Coordination Chemistry Reviews 501 (2024) 215561

Contents lists available at ScienceDirect

Coordination Chemistry Reviews

journal homepage: www.elsevier.com/locate/ccr

Review

Fluorescent and colorimetric sensors for anions: Highlights from 2020 to 2022

Giacomo Picci [a], Riccardo Montis [b], Alexander M. Gilchrist [c], Philip A. Gale [d,*], Claudia Caltagirone [a,*]

[a] Dipartimento di Scienze Chimiche e Geologiche, Università degli Studi di Cagliari, S.S. 554 Bivio per Sestu, 09042 Monserrato, CA, Italy
[b] Department of Pure and Applied Science, University of Urbino, Via della Stazione 4, I-61029 Urbino, Italy
[c] The University of Sydney, School of Chemistry, Sydney, NSW 2006, Australia
[d] University of Technology Sydney, Faculty of Science, School of Mathematical and Physical Science, Ultimo, NSW 2007, Australia

ARTICLE INFO

Keywords:
Supramolecular chemistry
Anion sensing
Fluorescence
Optical chemosensors

ABSTRACT

The development of colorimetric and fluorescent sensors continues apace. In this review, we highlight developments made in this area from 2020 to 2022. The review is structured by the different non-covalent interactions used to bind anions in addition to covering photoswitchable systems, excimers and molecular logic gates, and arrays for anion sensing.

1. Introduction

Anions play a multitude of roles in biological and industrial processes. Significant effort has been devoted to the development of colorimetric and fluorescent sensors for anionic guests. This review covers advances in this area between the years 2020 and 2022. The review is structured by the different non-covalent interactions used to bind anions in addition to covering photoswitchable systems, excimers and molecular logic gates, and arrays for anion sensing. Interesting developments over this period include the use of vesicles as filters for improving the performance of sensors and further developments of sensors that can be used within cells.

2. Hydrogen bond based chemosensors

Chemosensors containing urea and thiourea groups have been widely reported in the literature. These functional groups can efficiently interact with the anions *via* the formation of directional hydrogen bonds, and in the presence of suitable fluorophores or chromophores, the optical properties of chemosensors can be finely tuned. Recently Vega, Lara, and co-workers have reported the bis-urea, **1**, bearing two naphthalene substituents as a fluorescent ON-OFF sensor for oxoanions and acetate (AcO^-) in particular (Fig. 1) [1]. The presence of the polyether bridge also allowed for the binding of metal ions. Upon the addition of increasing amounts of AcO^- (as its tetrabutylammonium (TBA) salt) in CH_3CN:dimethylsulfoxide (DMSO) (9:1, *v/v*) to a solution of **1** (5.0×10^{-6} M), caused quenching of the emission band of the system (centred at 367 nm) due to the electron transfer (eT) from the carbonyl group of the urea moiety to the naphthalene substituents in the excited state. The preferential formation of a 1:2 (**1**:2(AcO^-)) adduct was demonstrated by DFT calculations.

Interestingly, recent literature concerning anion sensing with urea receptors has moved towards the development of novel materials. As an example, Chen and co-workers reported on the aggregation-induced emission (AIE) of urea-containing poly(phenylene ethynylene) **2** (Fig. 2) [2]. The aggregation properties of **2** were investigated in the absence and in the presence of anionic guests (CN^-, N_3^-, AcO^-, F^-, Cl^-, I^-, and Br^-) in dimethylformamide (DMF)/H_2O (1:1, *v/v*). Polymer **2** exhibited an emission band at 442 nm: upon the addition of the anion guests, a quenching of the emission was observed in all cases; CN^- also caused a remarkable red shift moving the emission band at 464 mm (Fig. 2A). To study the effect of the presence of the anionic guests on the aggregation properties of the polymer, dynamic light scattering (DLS) analysis was performed. As clear from Fig. 2B, the addition of the anion caused a disaggregation of the polymer with a decrease of the average hydrodynamic diameter (D_h) in the presence of various anions. Given the selective fluorescence response of polymer **2** towards CN^-, the authors investigated the effect of the concentration of CN^- on the

* Corresponding authors.
E-mail addresses: philip.gale@uts.edu.au (P.A. Gale), ccaltagirone@unica.it (C. Caltagirone).

https://doi.org/10.1016/j.ccr.2023.215561
Received 5 October 2023; Accepted 6 November 2023
Available online 12 December 2023

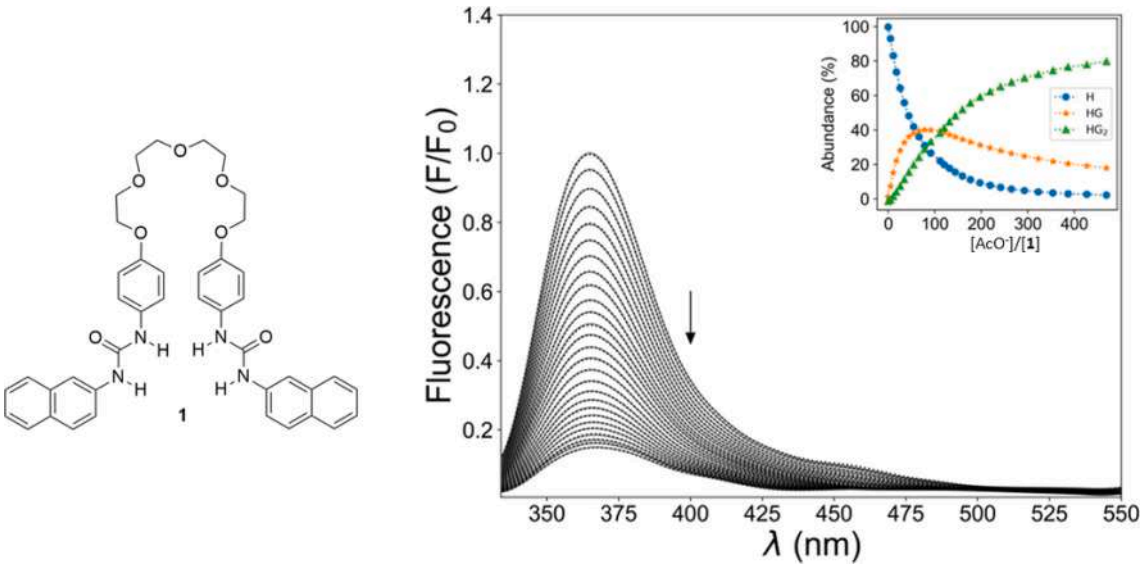

Fig. 1. Changes in the emission spectrum of **1** (5.0×10^{-6} M) upon the addition of increasing amounts of TBAAcO (0–2.35×10^{-3} M) in CH_3CN:DMSO (9:1, *v/v*), λ_{exc} = 298 nm. Inset: speciation of H (1), HG (1:1, **1**:AcO^- adduct) and HG_2 (1:2, **1**:2(AcO^-) adduct). Reproduced with permission from Ref. [1]. Copyright ACS, 2022.

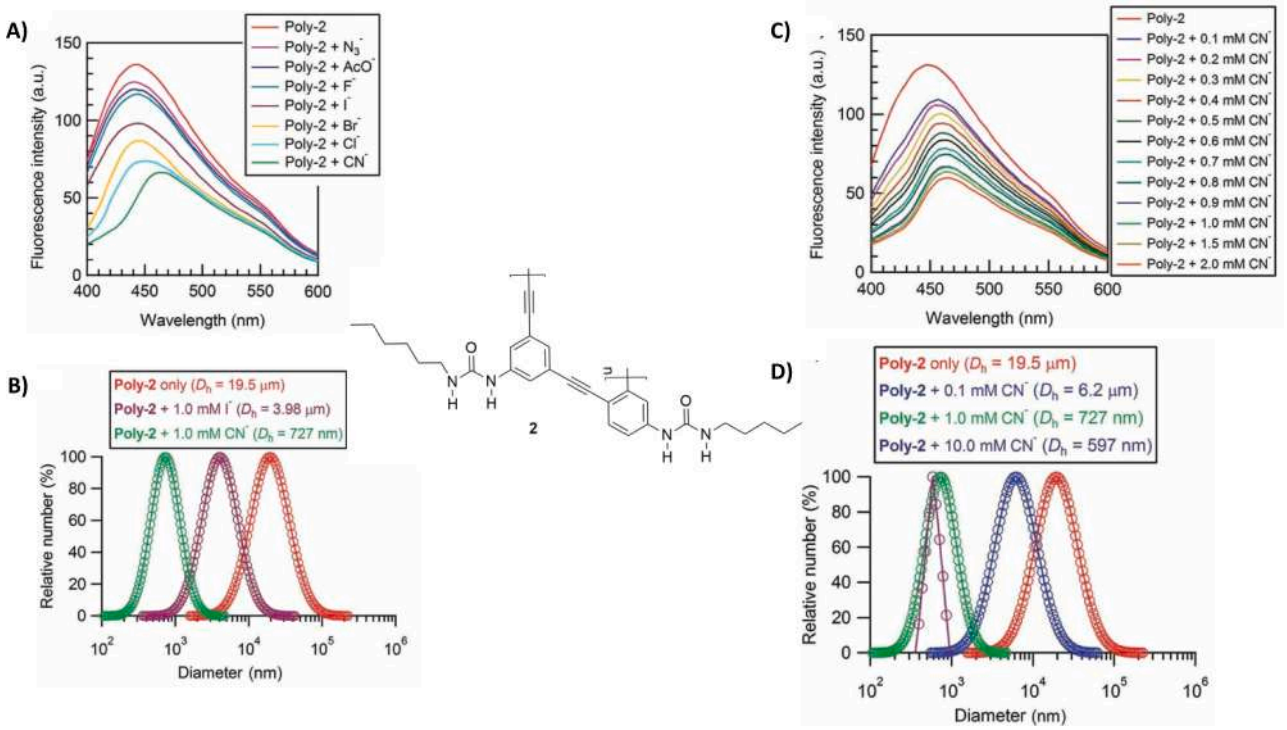

Fig. 2. A) Changes in the fluorescence emission of polymer **2** in DMF/H_2O (1:1, *v/v*) upon the addition of different anions. B) Changes in the average dynamic diameter of **2** in the presence of I^- (purple) and CN^- (green). C) Quenching of the fluorescence emission of polymer **2** in DMF/H_2O (1:1, *v/v*) upon the addition of increasing amounts of CN^-. D) Changes in the average dynamic diameter of **2** in the presence of increasing amounts of CN^-. Copyright Taylor and Francis 2021. Reproduced with permission from Ref. [2].

aggregate's dimensions. A net decrease in the dimension of the particles was observed with the concomitant fluorescence quenching illustrating the AIE properties of the system.

By dispersing polyvinyl *N*-(4-(4-nitrophenylazo)phenyl)-*N'*-methylthiourea into polymethylmethacrylate (PMMA) fibres, Kato and co-workers were able to obtain a polymer for the sensing of hydrophilic anions in protic solvents [3]. Methanolic solutions of hydrophilic anions such as Cl^-, AcO^-, and $H_2PO_4^-$ could penetrate the nanofibers of the material, causing a change in the intensity of the diffuse-reflection absorption spectrum of the polymer and a red-shift of the absorption band due to the formation hydrogen bonding interactions between the anionic guests and the thiourea moieties. It was also demonstrated that the polymers response to the tested anions was dependent on the thickness of the fibres (the thinner the fibres, the smallest was the response).

A novel approach for fluoride sensing has been introduced by Torres, Brovetto, Veiga, and co-workers, who reported a urea-based imprinting

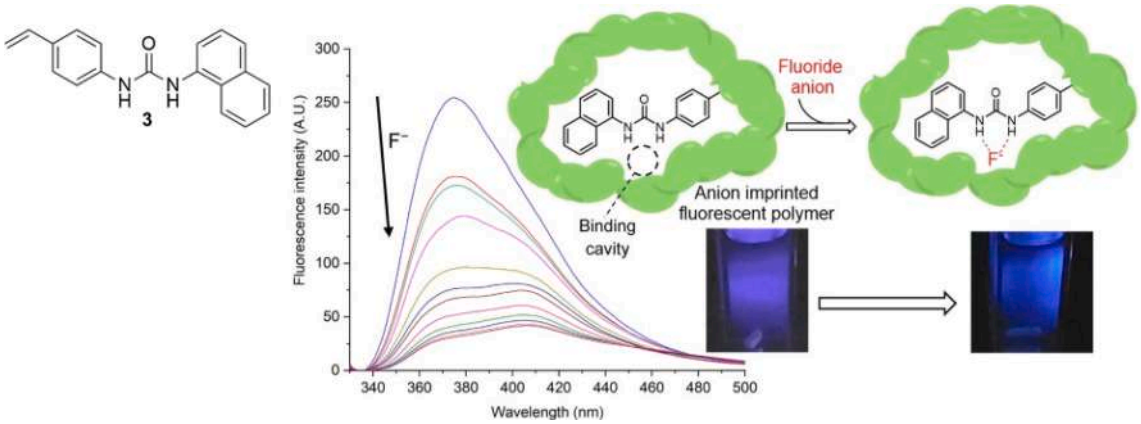

Fig. 3. Fluorescence quenching caused by fluoride in DMSO in the imprinted polymer based on receptor **3** (λ_{exc} = 319 nm). Reproduced with permission from Ref. [4]. Copyright Elsevier 2022.

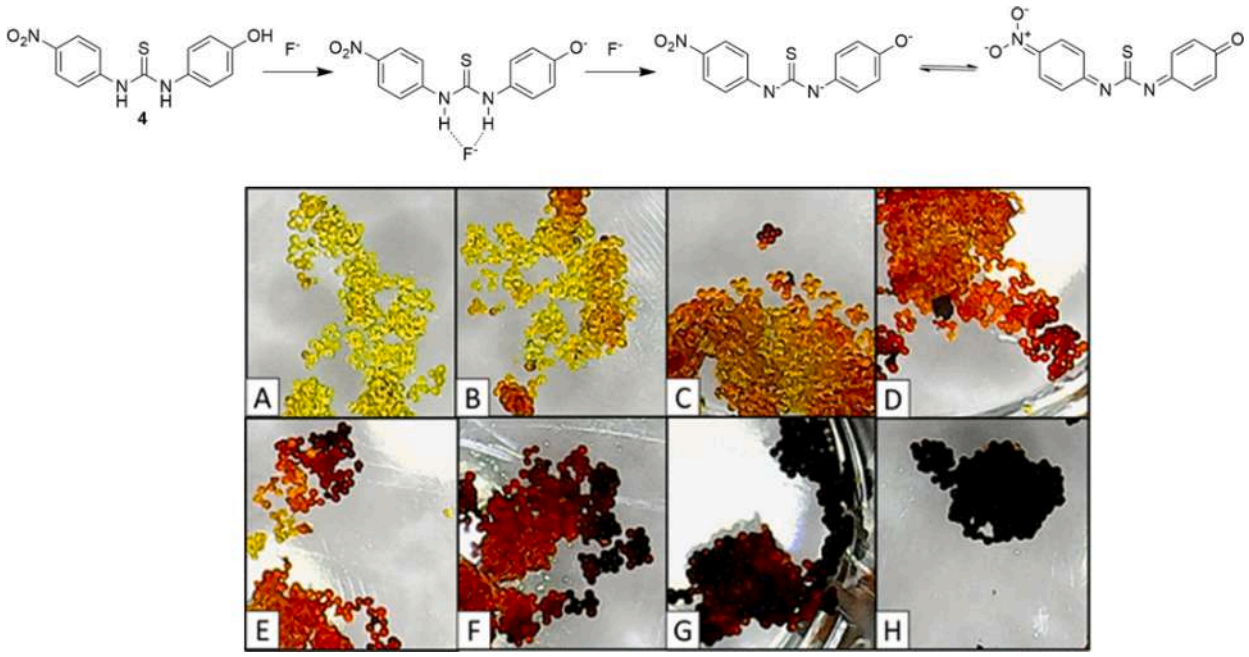

Fig. 4. 1) Proposed scheme for the binding/deprotonation process of fluoride by thiourea **4** and 2) the colorimetric response of **4** towards increasing concentrations of F^- (added as TBAF) supported by Tentagel resin in H_2O: A) resin functionalised with **4**, B) TBAF (0.2 mM), C) TBAF (0.4 mM), D) TBAF (0.6 mM), E) TBAF (0.8 mM), F) TBAF (1 mM), G) TBAF (2.5 mM), H) TBAF (5 mM). Reproduced with permission from Ref. [5]. Copyright ACS 2021.

polymer capable of sensing the presence of fluoride anions [4]. In order to enhance the sensing properties of the fluorescent urea **3** (Fig. 3), the authors prepared a polymeric optical sensor by reacting compound **3** with ethylene glycol dimethacrylate (EDMA) as cross-linking agent and 2,2′-azobis(2-methylpropionitrile) (AIBN) in the presence of F^- as the TBA salt. Removal of the anion led to the novel polymeric materials with a specific binding pocket for the anion. Upon the addition of F^- to a solution of the polymer in DMSO, a quenching of the emission band at 374 nm was observed (Fig. 3). Compared to the free receptor, the sensitivity towards fluoride improved in the polymer (LOD = 18.3 μM in **3** and 11.3 μM in the polymer). Moreover, the interference of the other anions, especially $H_2PO_4^-$, is negligible, with 70 % of F^- entrapped by the polymeric matrix vs 4.8 % of $H_2PO_4^-$.

Thiourea **4** bearing a phenol group was studied in a DMSO solution with different anions [5]. It was demonstrated that in DMSO solution AcO^-, $H_2PO_4^-$, and F^- anions deprotonated the phenol OH and subsequently the thiourea NHs causing the solution to change colour. Thiourea **4** was linked to Tentagel resin as a solid support, and the functionalised resin could detect the presence of fluoride even in 100 % aqueous solution (Fig. 4).

Interestingly, although the solid support allowed for sensing in 100 % water, the sensitivity of the system decreased when compared to the DMSO solution, presumably due to enhanced competition for the formation of hydrogen bonds between the thiourea NH groups, fluoride anions and the oxygen atoms of the polyethylene groups of the PEG at the surface of the resin.

Busschaert and co-workers have demonstrated an innovative method to enhance the selectivity of sensors called the transporter-liposome-fluorophore (TLF) approach [6]. As shown in Fig. 5A, this method is based on the encapsulation of a non-selective fluorophore inside liposomes and the use of non-selective small molecule transporters to enhance the fluorophore response. Only the analytes that are transported inside the vesicles and can give an optical response can be sensed. Lucigenin was chosen as fluorophore and 1,3-diphenylurea as anionophore. Lucigenin (1 mM) was encapsulated inside egg phosphatidylcholine (EggPC) unilamellar vesicles (100 nm) containing $NaNO_3$ and

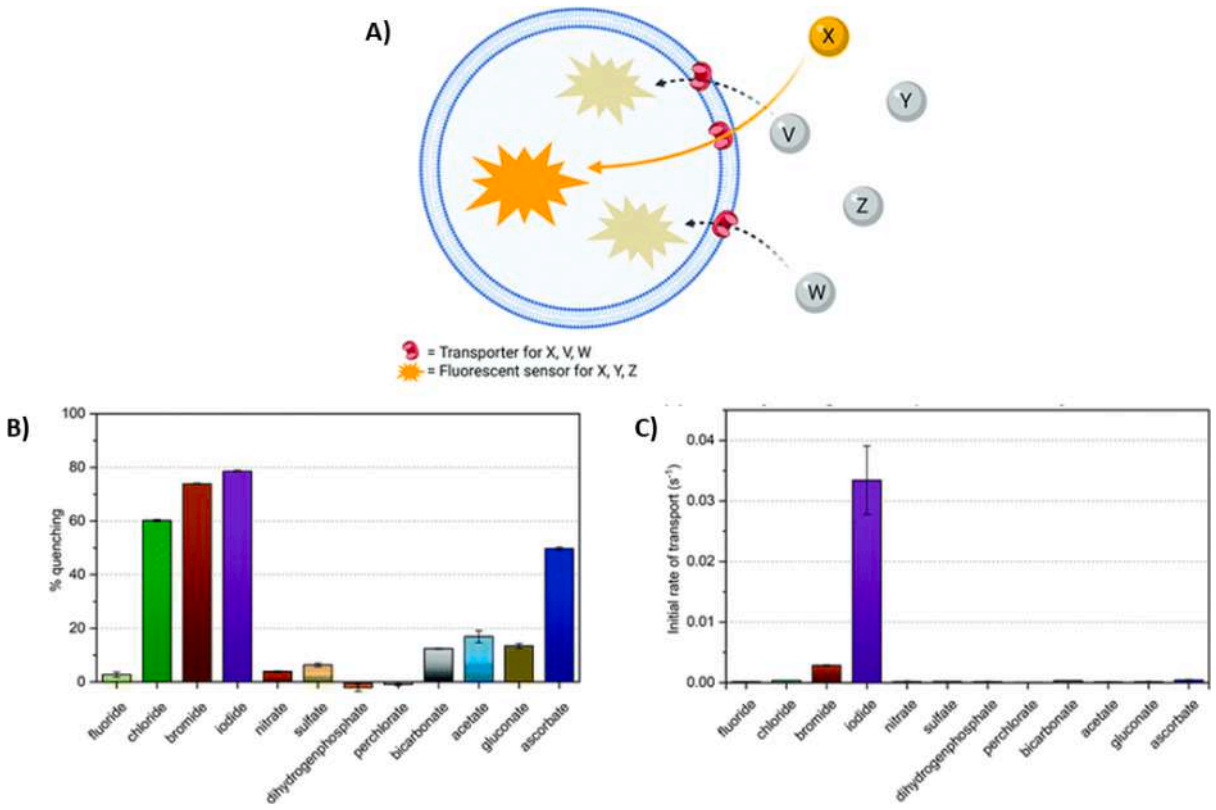

Fig. 5. A) Scheme describing the TLF approach; B) percentage of quenching of free lucigenin upon addition of various anions as their sodium salts at 16.4 mM; C) TLF approach response evaluated considering the initial rate of transport by different anions as their sodium salts at 25 mM. Adapted with permission from Ref. [6]. Copyright RSC 2020.

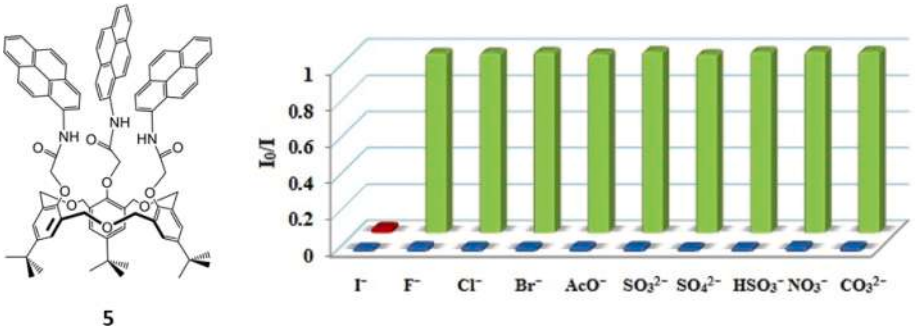

Fig. 6. Competition experiments conducted on **5** in THF/H_2O (7:3, *v/v*) at pH = 7.0 buffered with Tris-HCl. The green bar represents the fluorescence intensity (I_0/I) response at 458 nm of **5** in the presence of 100 equivs. of each tested anion. The blue bar represents the I_0/I response at 458 nm of **5** in the presence of 100 equivs. of I^- and 100 equivs. of each tested anion. The red bar represents the response of **5** in the presence of I^- and all the other anions. Reproduced with permission from Ref. [13]. Copyright Elsevier 2020.

buffered to pH 7.4 with 4-(2-hydroxyethyl)-1-piperazineethanesulfonic acid (HEPES), while the vesicles were suspended in a solution of $NaNO_3$ (22 mM), NaI (25 mM), and HEPES at pH 7.4. A DMF solution of the anionophore was added, and the transport was monitored for 5 min following the quenching of the lucigenin. The experiment was performed in the presence of various anions (F^-, Cl^-, Br^-, NO_3^-, SO_4^-, $H_2PO_4^-$, ClO_4^-, HCO_3^-, AcO^-, gluconate, and ascorbate) and as shown in Fig. 5B and C a great enhancement of the selectivity towards I^- was observed in the TLF approach when compared to the free lucigenin.

Amide-based chemosensors have continued to attract the attention of researchers [7–12]. The C_{3v} symmetry hexahomotrioxacalix[3]arene **5** functionalised with three pyrene moieties as the active fluorescent units has been reported by Zhang, Yamato, and co-workers (Fig. 6) [13]. Upon excitation of **5** at 346 nm, a selective quenching of the fluorescence band at 484 nm was observed in the presence of I^- with respect to other anions (F^-, Cl^-, Br^-, AcO^-, SO_3^{2-}, SO_4^{2-}, HSO_3^-, NO_3^-, and CO_3^{2-} added as sodium salts) in tetrahydrofuran (THF)/H_2O (7:3, *v/v*) at pH = 7.0 buffered with Tris-HCl. Competition studies demonstrated that the other anions tested did not cause interference with I^- (Fig. 6). The chemosensor works in I^- concentrations ranging from 0 to 200 μM with a LOD of 164 nM. Using ^1H NMR titrations, the authors demonstrated that a change in the conformation of the macrocycle occurs in the presence of I^- which interacts with the three amide moieties via the formation of hydrogen bonding interactions. The authors explain the observed fluorescence quenching of **5** is due to the formation of the H-bonds in tandem with the heavy atom effect that causes an increase in the population of the non-emissive triplet state.

The selective detection of CN^- in 100 % H_2O by the acetamide

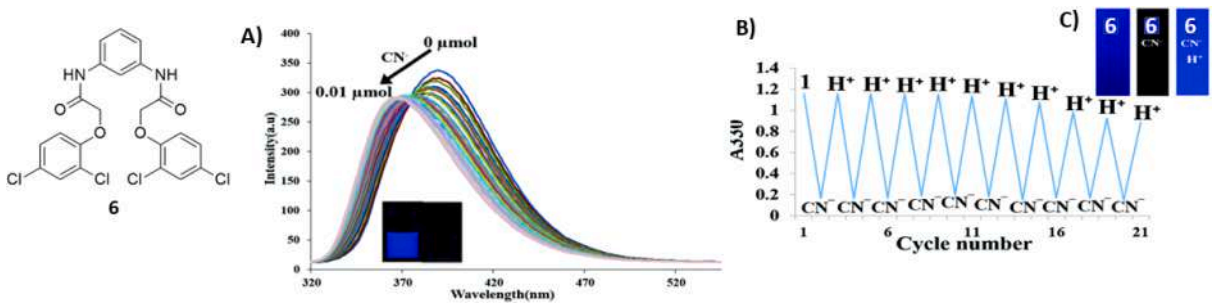

Fig. 7. The chemical structure of **6**, and A) the fluorescence titration of **6** in the presence of CN^- and a picture showing the changes in the emission under UV light.

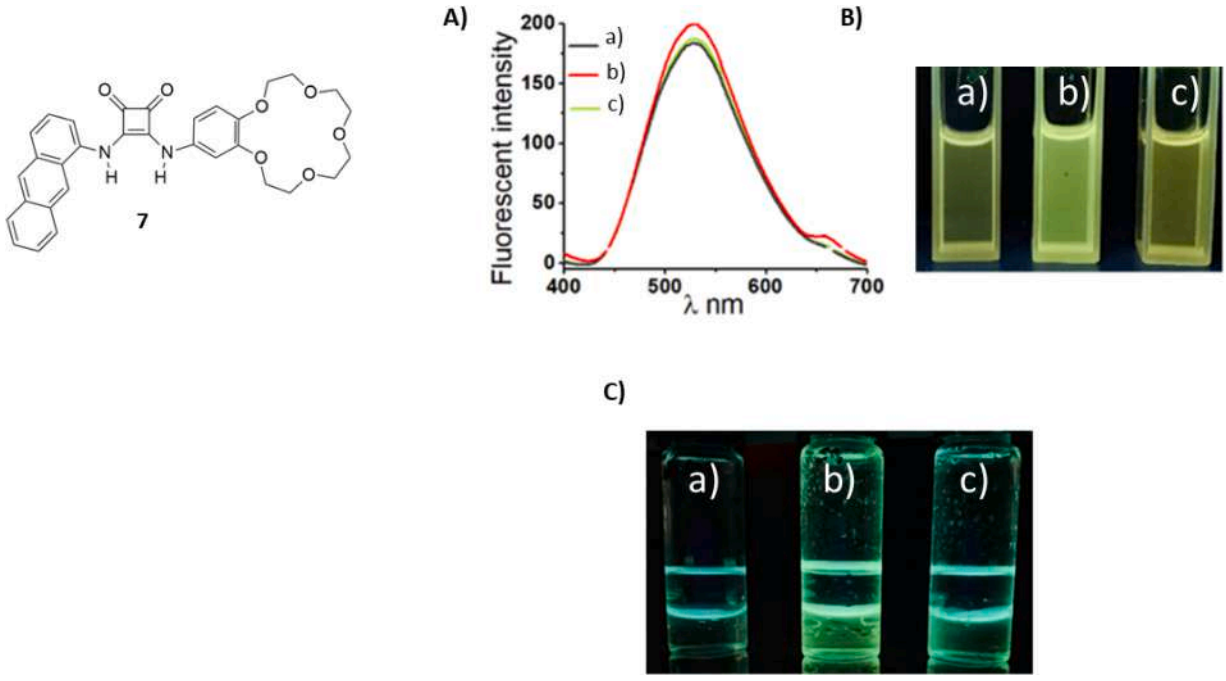

Fig. 8. A) Fluorescence spectra (λ_{exc} = 327 nm) of **7** a), **7** + 5 equivs. of $(TBA)_2SO_4$ b), **7** + 5 equivs. of TBACl c) in CH_3CN/H_2O (9:1, *v/v*). B) Pictures of **7** a), **7** + 5 equivs. of $(TBA)_2SO_4$ b), **7** + 5 equivs of TBACl c) in CH_3CN/H_2O (9:1, *v/v*) under UV light (254 nm). C) Pictures of a) a solution of **7** in $CHCl_3$ in contact with an aqueous solution, b) after extraction of an aqueous solution of K_2SO_4, and c) after extraction of an aqueous solution of KCl. Reproduced from Ref. [21]. Copyright MDPI 2021.

derivative **6** was reported by Darabi and co-workers (Fig. 7) [14]. When dissolved in an organic solvent, such as DMF, **6** showed a weak emission at 359 nm (Φ = 0.015); however, upon the addition of increasing amounts of water, an intense fluorescence emission at 389 nm appeared (Φ = 0.1). This is due to AIE as **6** can self-assemble, forming intramolecular H-bonds and π-π stacking in the presence of water. In a 100 % aqueous solution at pH = 7.4 upon the formation of a 1:1 adduct ($K_a = 4 \times 10^8$) with CN^- (as the sodium salt), the emission of **6** is blue shifted to 359 nm, suggesting that the presence of CN^- disassembles the system (Fig. 7A). All the other tested anions (Br^-, Cl^-, F^-, I^-, SCN^-, S^{2-}, SO_4^{2-}, SO_3^{2-}, $S_2O_3^{2-}$, $S_2O_4^{2-}$, $S_2O_5^{2-}$, ClO_3^-, ClO_4^-, IO_3^-, IO_4^-, CH_3COO^-, BrO_3^-, HSO_4^-, MoO_4^{2-}, $H_2PO_4^-$, NO_3^-, and NO_2^-) resulted in no observed changes. A LOD of 8.2 nM was calculated for CN^-. The changes in the fluorescence emission caused by CN^- are reversible upon the addition of HCl, the original emission is restored both in solution and in solid-state on strip test (Fig. 7B–C). This interesting system is also able to detect CN^- extracted from apricots, peaches, and bitter almond seeds.

Compared to analogous ureas and amides, it has been demonstrated that the use of squaramide-based receptors offers several advantages in terms of anion binding efficiency [15–20].

The fluorescent heteroditopic receptor **7**, reported by Romański and co-workers, is able to extract sulfate salts and detect them via fluorescence emission (Fig. 8) [21]. The squaramide portion of the molecule interacts with the SO_4^{2-} anions, the benzo-18-crown-6 interacts with the metal cation, while the anthracene moiety acts as the fluorescent unit. As shown in Fig. 8A and B, in a solution of CH_3CN/H_2O (99:1, *v/v*), the fluorescence emission of **7** increased upon the addition of 5 equivs. of $(TBA)_2SO_4$, probably because of an exchange between the water molecules and the anion within the binding sites of the chemosensor. Upon the addition of TBACl, the fluorescence did not appreciably change. Similar changes were observed in $CHCl_3$, and this gave the possibility to develop a two-phase fluorescent sensor as the system can selectively extract K_2SO_4 from water and change its fluorescent emission (Fig. 8C).

Elmes and co-workers have very recently described the self-aggregation behaviour of naphthalimido-squaramides **8**–**10**, which did not show any specific sensitivity towards anions, although anion binding selectivity was observed towards AcO^- in DMSO-d_6 during ^1H NMR titrations at 298 K [22]. The authors showed that the non-symmetric naphthalimido-squaramides **11** and **12** also self-aggregate and change colour in solution upon deprotonation in the presence of basic anions such as F^-, AcO^-, SO_4^{2-}, and $H_2PO_4^-$ [23].

Caltagirone, Picci, and co-workers have shown that the Cu(II)

complex of bis-pyrenyl-squaramide **13** is capable of switch-on fluorescence sensing towards basic anions (OH^-, CN^-, and F^- as their TBA salts) in CH_3CN via deprotonation of the squaramide NHs [24].

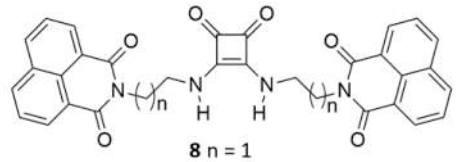

8 n = 1
9 n = 4
10 n = 7

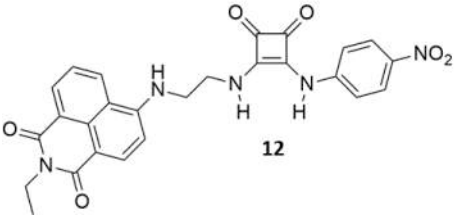

12

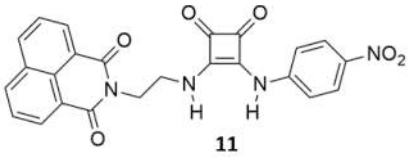

11

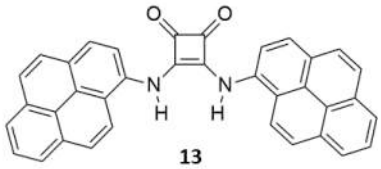

13

Various research groups have also reported imidazole-based chemosensors in the last few years [25–31]. Misra and co-workers have described the sensing properties based on the intramolecular charge transfer mechanism towards CN^- and F^- of the imidazole derivative **14** (Fig. 8) [32]. Chemosensor **14** showed a solvatochromic behaviour with a bathochromic shift of the emission with the increase of the polarity of the solvent and a tendency to aggregate in 1,4-dioxane with a disaggregation effect due to the presence of water. In the presence of basic anions such as CN^- and F^- in a 1,4-dioxane solution, dramatic changes in the absorption and emission properties of **14** were observed. The absorption band of the free chemosensor at 416 nm was red-shifted to 538 nm upon the addition of F^- and further blue-shifted to 122 nm in the case of CN^- (Fig. 9A) with the colorimetric changes being observable by the naked eye.

The emission band at 548 nm of the free **14** (arising from excitation at 416 nm) was quenched and blue-shifted (at 488 nm) upon the addition of 7 equivs. of CN^-, while a simple quenching was observed when titrating **14** with an increasing concentration of fluoride. Proton-NMR titrations in DMSO-d_6 were used to elucidate the interaction between the chemosensor and the tested anions, which is an acid-base interaction with F^- with deprotonation of the imidazole N–H and a H-bond interaction along with a nucleophilic Michael addition at the lactone moiety of the coumarin fragment of **14** with CN^-.

3. Halogen-bond based chemosensors

Due to their directionality and strength, halogen bonds (XBs) [33] represent another important intermolecular interaction for the design of supramolecular systems [34]. According to the recommendation of IUPAC [35], a halogen bond "*occurs when there is evidence of a net attractive interaction between an electrophilic region associated with a halogen atom in a molecular entity and a nucleophilic region in another, or the same, molecular entity*". In other words, a halogen bond is a highly directional and attractive interaction occurring between an electron-deficient halogen atom and a nucleophile or a Lewis base. Amongst the variety of electron-rich systems, anions represent good candidates to interact with electron-deficient halogen atoms. Accordingly, over the past few years, halogen bonding has become a promising tool for the design of anion receptors and probes [36]. Recent work focused on the design of probes based on iodo-triazole derivatives [37–40].

In a recent article [39], Beer and co-workers described three new probes containing pyridine (**15**), pyridinium (**16**) or a secondary amine (**17**) spacers, functionalized with coumarin fluorophores decorated with hydrophilic triethylene glycol (TEG) substituents and incorporated into a XB bis-iodotriazole donor-site (Fig. 10). Analogous hydrogen bonding-based receptors (**18**–**20**) were also synthesized and their properties compared to compounds **15**–**17** (Fig. 10). The sensing ability of the receptors towards HS^- and halides were investigated by fluorescence spectroscopy in buffered aqueous solutions (HEPES buffer at pH 7.4). Among the three XB-based receptors, **15** exhibited the highest selectivity for HS^-, behaving as a supramolecular probe for HS^- over the halides. When excited at 342 nm, **15** showed a significant quench of its fluorescence emission (60 %) only in the presence of HS^- (Fig. 10A), while no variation of the emission intensity was observed in the presence of halides (Cl^-, Br^-, and I^-, Fig. 10B). In the case of **16**, the addition of an increasing amount of HS^- resulted in quenching of the fluorescence emission of approximately 45 %. In the presence of halogens, the receptor exhibited a response only upon the addition of Br^- and I^-. Receptor **17**, under the experimental conditions used for the titration experiments, existed mainly in its protonated form **17**H^+. Upon addition of the target anion species, **17**H^+ responded only in the presence of HS^- and I^-. Interestingly, compared to their XB-based analogues, the HB-based probes **18**–**20** showed no detection ability towards the target anions. These results were also confirmed by density functional theory (DFT) and molecular dynamics simulations.

A recent article by Docker and Hang et al. [38] reported a family of probes (**21**–**27**) for anion detection based on tetraphenylethene (TPE) derivatives bearing iodo-triazole halogen bond donors.

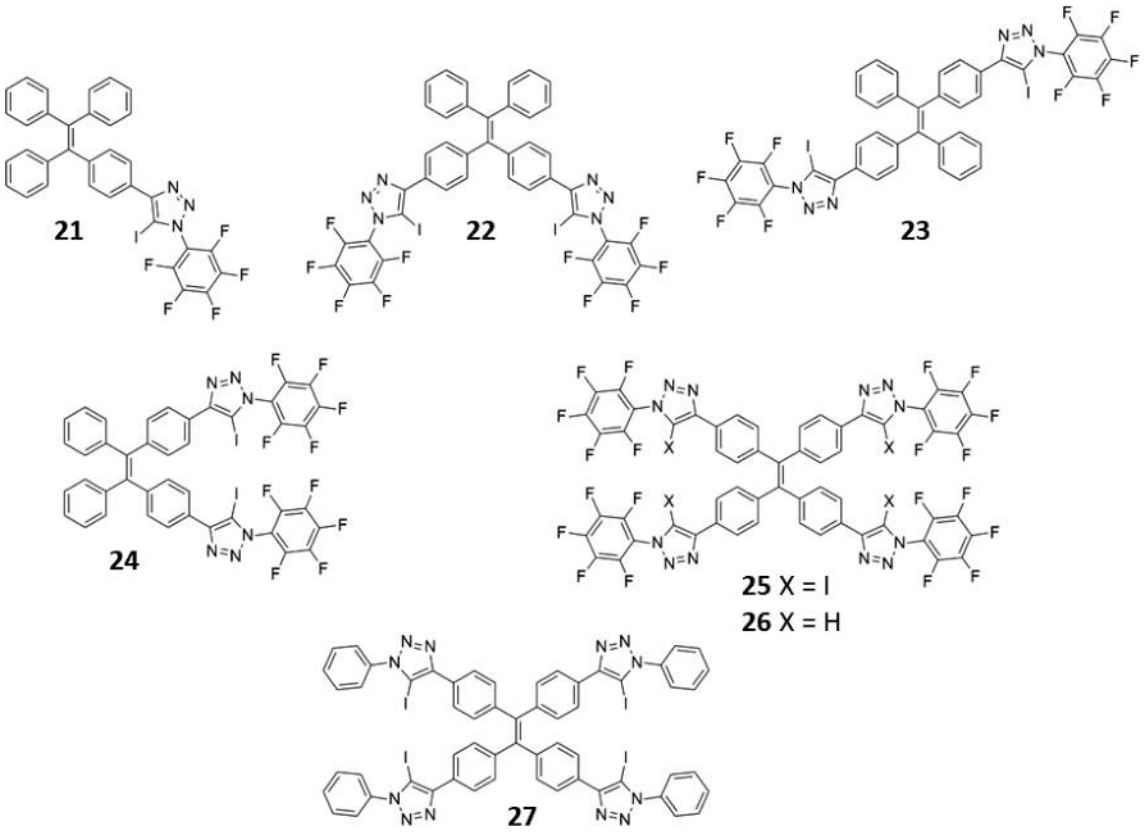

The binding ability of **21**–**27** towards halides was investigated using ^{1}H NMR titration techniques in THF-d_8 at 298 K. The different structures of **21**–**27** result in different binding modes and stoichiometries. With compounds **22** and **23**, the two iodotriazole donors are too far apart to allow for chelation in a bidentate fashion. However, in the case of **24**, the two iodotriazole donors cooperate in the binding process. In particular, the differences in the anion binding properties observed for the two *E* and *Z* derivatives **23** and **24** prompted investigations on the possibility that the two isomers can be interconverted by light, acting as photo-switchable anion receptors. The presence of additional XB donors in compounds **22**–**27** enables higher binding stoichiometries. However, depending on the geometrical features of the binding site, the complexation with higher stoichiometry can be considerably weaker with respect to the formation of the 1:1 complex. This is the case with **24**, in which, due to the proximity of the two iodotriazole donors, the formation of the 1:2 complex shows negative cooperativity, presumably due to anion-anion repulsion. Similar behavior is observed for the tetradentate receptors **25** and **26**, while HB-based bi-dentate receptor **27** shows weak binding properties. The ability of **21**–**27** to detect anionic species was also investigated. The results of the fluorescence titration experiments of **21**–**27** in the presence of increasing amounts of halides show a strong response only in the case of the perfluoro-tetradentate **25**, which exhibits a three-fold increase of the emission band at 520 nm accompanied by a blue-shift (≈ 20 nm) after the addition of 10 equiv. of Cl^- (Fig. 11A). This response is ascribed to an AIE mechanism. Single-crystal X-ray diffraction and DLS measurements confirm the tendency of **25** to aggregate in the presence of Cl^- (Fig. 11B and C). DLS measurements revealed that in the absence of Cl^- anions, **25** does not tend to form aggregates, while the addition of one equivalent of Cl^- induces the formation of aggregates with a size of approximately 100 nm (Fig. 11B).

4. Boron-based chemosensors

Several boron-based chemosensors for anions have been developed recently. With the exception of systems bearing BODIPY dyes, where the boron centre is not directly involved in the interaction with the anion, there are some examples that utilise boron-based functional groups to bind anions, transducing the binding event into a colorimetric or fluorescent response. The sensing mechanism involves the addition of the nucleophilic anion (usually F^- or CN^-) to the boron Lewis acid, with the consequent change of its geometry (from trigonal planar to tetrahedral) and electronic structure, causing changes in the photophysical properties, including absorption and emission. Among boron-based sensors, boronic acid derivatives, due to their synthetic versatility and low toxicity [41], have been extensively applied for anion sensing. Recognition of anions occurs either by exploiting the Lewis acidity of the boron centre through a direct B–A^- coordination or, in a few cases, via hydrogen bonding with the $B(OH)_2$.

Minami, Liu et al. [42] have recently described a fluorescent chemosensor array based on two pyrenylboronic acid derivatives (**28** and **29**) for the simultaneous discrimination of AcO^-, oxalate ($C_2O_4^{2-}$), malonate ($C_4H_2O_4^{2-}$), citrate ($C_6H_5O_7^{3-}$), F^-, dihydrogen phosphate, $H_2PO_4^-$, and pyrophosphate ($HP_2O_7^{3-}$). The ability of **28** and **29** to recognize the analytes was investigated by fluorescence titrations and electrospray ionization mass spectrometry (ESI-MS). Depending on the analytes, **28** and **29** responded by an OFF-ON and ON-OFF fluorescence response due to photoinduced electron transfer (PET) between the fluorophore and the boron atom, originating from anion recognition. The binding constants, $K = 4.2 \times 10^8$ and 1.0×10^8 M^{-1} were obtained for **28** and **29**, respectively. The two pyrenylboronic acid derivatives were tested as an array for the qualitative and semi-quantitative discrimination of multiple anions using a linear discriminant analysis (LDA). The array allowed the successful discrimination of seven types of anions with

100 % accuracy and the quantitative detection of oxalate, malonate, and citrate in 1:1:1 mixtures.

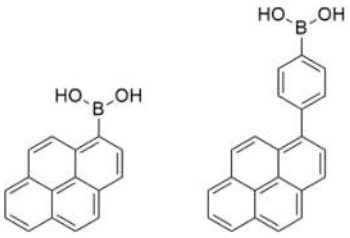

28 29

A recent article by Liu et al. [43] reported a BODIPY derivative bearing a pinacol boronate group (**30**) for the selective detection of F^- anions in aqueous solutions (Fig. 12A). The interaction of **30** with F^- anions caused a slight blue shift of the absorption band at 630 nm (Fig. 12B, top) and a turn-on fluorescence response at 677 nm (Fig. 12B, bottom), which proved to be stable in the pH range 3–9.

Furthermore, **30** exhibited high selectivity toward fluoride ions in the presence of other reactive cations and anions. The mechanism of recognition proposed (Fig. 12A) involves the coordination of the F^- anion by the sp^2 boron, causing a change from the trigonal planar to the tetrahedral geometry, as confirmed by ^{11}B NMR. Compound **30** was also tested for the detection of F^- in real water samples and in-vivo fluorescence bioimaging of F^- anions (Fig. 12C), opening the possibility of applying this system in environmental and biological samples.

The use of boronic acid derivatives to sense anions via hydrogen bonding has been recently investigated, both experimentally and computationally. Yatsimirsky and co-workers reported on the sensing properties of an anthracene appended *o*-aminomethylphenylboronic acid (**31**) towards 20 organic and inorganic anions [44]. In this case, depending on the anion species investigated, the boronic acid can interact via hydrogen bonding or directly coordinate with the anion. In the presence of fluoride anions, the Lewis acidic behavior of the $B(OH)_2$ is favoured, as evidenced by ^{11}B NMR data, that are consistent with the formation of a tetrahedral Lewis-type adduct. On the other hand, in the presence of carboxylate, phosphate and sulfate anions, the boronic acid group interacts with them by hydrogen bonding (Fig. 13). In most cases, the recognition process involves a turn-OFF fluorescence response attributed to the enhanced PET. The aminomethyl group in **31** is involved in an intramolecular hydrogen bond with the $B(OH)_2$. This interaction blocks the quench of the fluorescence generally observed in the case of derivatives featuring the aminomethyl group attached to anthracene and ascribed to the PET mechanism. The interaction between the boronic acid and the anion competes with the intramolecular interaction with the methyl amine group, restoring the PET-induced quench of the fluorescence.

Interestingly, in the presence of monoanions of dicarboxylic acids, the quenching of the fluorescence decreases dramatically, resulting in an opposite turn-on effect. This was explained as the result of a decrease in PET due to the formation of a COOH···N hydrogen bond between the non-dissociated COOH group of the dicarboxylic acid and the aminomethyl moiety. This effect was particularly marked in the presence of the malonic acid monoanion, opening the possibility of selective detection of this species among other anions.

Boronic acid derivatives have also been employed for the design of boron-containing polymers as emerging chemosensors. Brantley and colleagues [45] developed a boron-based polymer obtained by esterification of polyvinyl alcohol with aryl boronic acids. Through UV–Vis and spectrofluorimetric titrations showed an optical response in the presence of borophilic anions such as OH^-, F^-, and CN^-. Further DFT calculations at the B3LYP2/def2-SVP3 level of theory suggest that the anion binding process combines the Lewis acidity of B(III) through a direct B–A^- coordination and the hydrogen bond character of the other OH groups in the polymeric chain.

Triarylboranes represent another class of tri-coordinated boron derivatives that have found an application for the detection of small anionic species, such as F^- and CN^-. Qi *et al.* have recently reported an interesting example of an organoboron derivative with a multiple resonance (MR) effect (**32**) for the selective detection of fluoride anions (Fig. 14A) [46]. This type of fluorophore possesses useful properties, such as narrow-band emission, high fluorescence quantum yields and good chemical and thermal stability, making them the ideal candidates for several applications, including organic light-emitting diode (OLED) applications. The photophysical properties of **32** were investigated by UV–Vis absorption and fluorescence spectroscopy in THF at room temperature (298 K). Chemosensor **32** exhibited weak absorption bands between 282 nm and 368 nm and an intense band at 467 nm. A sharp and narrow emission band at 485 nm and a blue-green fluorescence was also observed. The photoluminescence quantum yield (PLQY) was 90 %. The system also exhibited excellent thermal and photochemical stability. The anion binding properties of **32** were investigated by UV–Vis and fluorescence spectroscopy in THF solutions (Fig. 14B and C). In the presence of incremental amounts of TBAF, an increase in the intensity of the emission at 282 nm and 368 nm was observed, with a concomitant decrease in the intensity of the absorption bands at 322 nm and 466 nm. Upon the progressive addition of TBAF, the emission band at 483 nm decreased dramatically. The calculated LOD was 7.2×10^{-11} mol L^{-1}. The quenching of the fluorescence was ascribed to the formation of the B–F^- adduct, obtained through the occupation of the empty p_π orbital of the boron center by the anionic species, destructing the MR structure of **32**. The authors used DFT calculations to confirm the disruption of the MR structure promoted by the formation of the B–F^- adduct (**32**·F^-).

The crystal structure of both **32** and the B–F^- adduct were obtained by single-crystal X-ray diffraction (Fig. 14D and E). While the structure of **32** shows a trigonal planar geometry of the boron center, the B–F^- adduct clearly showed a tetra-coordinated boron center, though this is unusually bound to an oxygen atom located between the boron and the aromatic ring. This observation was explained as the result of an oxidation process that occurred during the crystallization experiment. The formation of a tetra-coordinated B–F^- adduct was further confirmed by ^{11}B NMR titration experiments in THF. The results show the appearance of new signals at −152 and 11.5 ppm, confirming the formation of a 1:1B–F^- adduct after the addition of 1 equiv. of TBAF. The calculated binding constant for the B–F^- adduct was $K_a = 1.16 \times 10^5$ M^{-1}. The 1:1 stoichiometry was also confirmed by a job plot. The formation of the B–F^- adduct was also investigated in the presence of interfering anions, such as Cl^-, Br^-, I^-, NO_3^-, ClO_4^-, BF_4^-, PF_6^-, AcO^-, and $H_2PO_4^-$. The results suggest that **32** only exhibits remarkable fluorescence changes in the presence of F^-, while the addition of the other anions resulted in no significant changes.

Recent work has also focused on the development of triarylborane-based donor–acceptor (D–A) conjugates with improved optical properties [47–50]. Raveendran et al. investigated the influence of additional donors and acceptor groups on the optical properties and anion sensing of triarylborane–triarylamine-based donor–acceptor conjugates [51]. For this purpose, the electron-donating 4-ethynyl-*N*,*N*-dimethylaniline group and the electron-withdrawing 4-ethynylbenzonitrile group were introduced as an additional donor (**33**) and acceptor (**34**) on the triphenylamine unit and their properties compared to the neutral derivative (**35**, Fig. 15). The photophysical properties of **33**–**35** were investigated in different solvents. In CH_2Cl_2, the three derivatives showed two absorption bands in the region ~260 nm and ~390 nm, with differences that can be ascribed to the different nature of the substituents (Fig. 15A). With respect to the reference parent compound **35**, **33** and **34** showed, respectively, a red-shift and a blue-shift of the bands attributed to intramolecular charge transfer (ICT). When excited in the region 350–425 nm, analogous shifts were observed in the emission spectra. Furthermore, **35** and **34** produced a single emission band (at ~470 nm for **35** and ~440 nm for **34**), while **33** exhibited two emission bands, the local excited emission band (430 nm) and the ICT

band (515 nm). Increasing the solvent polarity caused a bathochromic shift in the emission spectra of the three compounds, with an effect more pronounced for **33**. The overall results suggest that the ICT band is predominant in **33** due to the presence of the donor moieties (NMe_2) and less important in **34** due to the presence of different acceptors that cause the redistribution of the charge transfer. This is also reflected in the higher quantum yields observed for compounds **35** and **34** when compared to that of **33**.

The anion binding properties of **33**–**35** were also investigated by UV–Vis and fluorescence titration experiments in CH_2Cl_2. The three compounds showed high selectivity toward F^- anions, even when other competing anions, such as Cl^-, Br^-, I^-, NO_3^-, ClO_4^-, and $H_2PO_4^-$ are present. Upon increasing amounts of TBAF, the ICT absorption band of **33** centred at 389 nm showed a bathochromic shift, accompanied by a decrease in intensity. A simultaneous increase in the intensity of the band at 350 nm was also observed. In the case of **35** and **34**, adding increasing amounts of TBAF caused a decrease of the two bands centred at ~375 nm and ~262 nm. Fluorescence titrations of **33** with increasing amounts of TBAF caused a gradual shift of the emission band at 515 nm to the region at 450 nm (Fig. 15B) with a simultaneous increase in intensity. In contrast to **33**, which showed a fluorescence enhancement, the emission bands of **35** and **34** showed a gradual quench upon the addition of increasing amounts of TBAF.

A rare case of time-resolved fluorescence sensing of fluoride using the two triarylborane derivatives **36** and **37** (Fig. 16, A) was reported by Lee and co-workers [52]. Chemosensors **36** and **37** both consist of a triarylborane skeleton substituted with a triazine acceptor, linked in the *ortho* position of the phenylene ring with a carbazole (Cz) or a diphenylamine (DPA) donor unit, respectively (Fig. 16A). The interaction of **36** and **37** with fluoride anions causes a decrease of the strong bands in the range 270–350 nm, attributed to the donor-centered $\pi - \pi^*$ transition mixed with the boron-centered π(Mes) $-$ p_π(B) charge-transfer transition (Fig. 16B). Chemosensors **36** and **37** show a further broad and weak absorption band at 413 nm and 451 nm, respectively, assigned to the ICT transition between D–A. In the case of **37**, the interaction with F^- caused a blue-shift of this band as the consequence of disruption of the conjugation between the boron and triazine acceptor. Fluorescence titration of **36** with increasing amounts of fluoride anions showed ratiometric changes in the fluorescence upon F^- binding, while **37** exhibited a turn-on fluorescence response. Both derivatives displayed thermally activated delayed fluorescence (TADF), behaving as a time-resolved turn-on fluorescence sensor. Both ^{11}B NMR and ^{19}F NMR measurements indicated that the fluoride is coordinated to the boron centre, causing a change in the coordination geometry. The response of chemosensor **37** in the presence of an excess of other anions, such as Cl^-, Br^-, I^-, ClO_4^-, NO_3^-, and HSO_4^-, was also studied. The system showed no response toward the set of anions analysed, leading to a strong turn-on fluorescence only in the presence of F^-. The selective detection of F^- by **37** was also tested in the presence of a competitive fluorophore (Coumarin 6) using time-resolved emission spectroscopy (TRES) with a delay of 100 ns. The results showed a complete disappearance of the signal from Coumarin 6, retaining only the long-lived fluorescence signals originating from the **37**·F^- adduct.

Single-crystal X-ray diffraction performed on the fluoride adduct of **36** (**36**·F^-) confirmed the formation of a tetra-coordinated boron (Fig. 16C). The crystal structure of **36** also showed that the design with D–A moieties substituted in the *ortho*- position on the phenylene ring introduces steric hindrance, promoting a D–A twisted conformation. As suggested by calculations, the D–A twisted conformation reduces the spatial overlap between the HOMO and LUMO, promoting a fast reverse intersystem crossing (RISC) process and, consequently, a TADF mechanism.

5. Metal-based chemosensors

Metal complexes possess a series of physical and chemical properties suitable for the design of selective anion chemosensors. The metal center, with its positive charge, coordination number and geometry, represents a potential selective Lewis acid binding site for anionic species. Most importantly, the metal ion can confer specific optical, photochemical, magnetic or redox properties to the system [53]. Several classes of metal-based chemosensors have recently been reported. In most of these cases, the recognition process involves a variation of the optical or fluorescent properties of the metal complex due to the interaction of the anion with the metal center or other parts of the chemosensor [24,54,55]. In a few other cases, the anion promotes the displacement of either the metal ion or other species, causing an optical response [56–58].

Huang and Pierre have recently developed a family of two Fe(III) receptors (**38** and **39**) for the selective recognition of phosphate anions (Fig. 17) [59]. In the two complexes, Fe(III) is respectively coordinated by tetra- (**38**) and pentadentate (**39**) 1,2-hydroxypyridinone ligands, with the remaining open coordination site occupied by a fluorescein molecule. This has the dual function of preventing the formation of the μ-oxo dimers and, at the same time, recognizing the target anion via indicator displacement assay (IDA). The ability of **38** and **39** to coordinate the phosphate anions and the concomitant displacement of the fluorescein moiety were investigated by ATR-IR, ^{31}P NMR, UV–Vis, and fluorescence spectroscopies. In particular, the fluorescence spectroscopy results show a 20-fold turn-on in fluorescence upon coordination of 1 equiv. of the PO_4^{3-} anion to the Fe(III) centre of both **38** and **39** (Fig. 17A and B). The results suggest that in both cases, a 1:1 binding mode with equilibrium constants $8.8 \times 10^5\ M^{-1}$ for Fe(III)·**38** and $1.1 \times 10^6\ M^{-1}$ for Fe(III)·**39**. The two probes showed high selectivity over the most common competing anionic species, such as CO_3^-, NO_3^-, SO_4^{2-}, halides (F^-, Cl^-, Br^-, and I^-), and AsO_4^{3-}.

A platinum-based dual-selective probe (**40**) for the recognition of cations and anions was recently developed by Yam and co-workers (Fig. 18) [60]. Probe **40** consists of a dipicolylamine (DPA)-containing alkynylplatinum(II) terpyridine complex, exhibiting a high affinity for Zn(II) (Fig. 18a). The addition of increasing amounts of $Zn(OTf)_2$ **40** shows a blue-shift of its low energy absorption band at 370–560 nm. The emission spectra show a band at approximately 600 nm attributed to the triplet metal-to-ligand charge-transfer (^{3}MLCT) excited state. Complexation of Zn(II) by the DPA moiety of **40** forms the probe, **40**·Zn^{2+}, which was able to recognize $Na_4P_2O_7$. In the presence of increasing amounts of $Na_4P_2O_7$, **40**·Zn^{2+} shows an increase of the low-energy absorption band at 650 nm and a decrease of the band at 415 nm, with a concomitant formation of a well-defined isosbestic point at 347 nm (Fig. 18A left). After the addition of approximately 1 equiv. of $Na_4P_2O_7$, the colour of the solution turns from yellow to orange (Fig. 18B). The emission spectra recorded at increasing concentrations of $Na_4P_2O_7$ show the appearance of a band at 770 nm, accompanied by a decrease of the ^{3}MLCT at 600 nm, suggesting the formation of aggregates (Fig. 18A right).

Molecular modelling and spectroscopic and spectrometric characterization suggest that the $HP_2O_7^{3-}$ anion bridges two **40**·Zn^{2+} units, which oligomerize via Pt···Pt and $\pi - \pi$ stacking interactions, resulting in the formation of nanofibers.

Khatua and colleagues developed a cyclometalated Ir(III) complex of a methylene-bridged benzimidazole-substituted 1,2,3-triazole, **41** for the detection of $H_2P_2O_7^{2-}$ (Fig. 19) [61]. Compared to the examples above, in this case, the binding site involves the use of weaker and directional intermolecular interactions such as hydrogen bonding, making the anion binding process reversible. Probe **41** showed a high selectivity for $H_2P_2O_7^{2-}$ even in the presence of other competing anions, such as $H_2PO_4^-$, ATP, ADP, and AMP. In CH_3CN **41** showed a weak emission at 483 nm and 510 nm (λ_{exc} = 370 nm; ϕ = 0.016) that increased upon titration with $H_2P_2O_7^{2-}$ (Fig. 19A). The results fit with a 1:1 binding model ($K_a = 8.6 \times 10^7\ M^{-1}$). Using ^{1}H NMR titrations, it was demonstrated that the anion interacts with the benzimidazole-substituted 1,2,3-triazole ligand via a set of C–H···O, N–H···O, and

O–H···O (Fig. 19B). Interestingly, **41** also shows low cytotoxicity against HeLa cells and is suitable for intracellular pyrophosphate imaging, opening the possibility of biological applications.

Ruthenium-based complexes represent another class of metal-based systems recently investigated for the development of selective anion-sensing probes [62–66]. Mukhopadhyay and co-workers [16] reported a fluorescent Ru(II)-complex (**42**) for anion sensing and bio-imaging (Fig. 20) [67]. Probe **42** consists of Ru(II)–arene scaffold combined with a glycine derivative. The sensing ability of **42** towards different anions (Cl^-, Br^-, I^-, CO_3^{2-}, SO_4^{2-}, N_3^-, NO_2^-, SCN^-, BPh_4^-, and $S_2O_8^{2-}$) has been investigated by UV–Vis and fluorescence spectroscopy in DMSO. When titrated with various anions. Compound **42** shows a red-shift of the absorption band at 330 nm only in the presence of CO_3^{2-} and SO_4^{2-} anions (Fig. 20A). Anions CO_3^{2-} and SO_4^{2-} also cause a significant quench of the fluorescence (Fig. 20B). Both anions interact with **42** in a 1:1 ratio via H-bond formation with the N–H and the adjacent aromatic C–H, with binding constants of $K_a = 3.97 \times 10^4\ M^{-1}$ and $2.59 \times 10^4\ M^{-1}$ for the formation of the adducts with CO_3^{2-} and SO_4^{2-}, respectively.

Due to their photophysical properties, such as sharp emission spectra and long luminescence life-time (up to ms), Lanthanide-based receptors represent another class of metal complexes that have received much attention in anion sensing [68]. Similar to what was observed for other metal-based receptors, anion binding and recognition processes by lanthanide-based probes can be achieved using different approaches. Lanthanide complexes, due to their affinity for oxyanions, represent the ideal candidates for the design of phosphate probes [69]. Accordingly, a number of recent examples focused on the development of probes for the detection of phosphates and nucleoside phosphate anions [70–73].

Anzenbacher and co-workers developed three carboxamidequinoline-Eu(III) complexes (**43**–**45**) for the recognition of phosphates in water (Fig. 21A) [74]. Upon complexation of Eu(III), the ICT state is suppressed, resulting in a quenched fluorescence emission of the carboxamidequinoline scaffold. The coordination of Eu(III) by phosphate species determines the displacement of the ligand and, consequently, the regeneration of its fluorescence emission (Fig. 21B). The three probes exhibit a higher affinity for ATP, followed by species with a decreasing number of phosphate moieties ($HP_2O_7^{3-}$, ADP, $H_2PO_4^-$, and AMP), as would be expected considering the role of electrostatic interactions in the binding process. In this sense, the selectivity of most reported nucleoside phosphate probes follows the order ATP > ADP > AMP [75]. Therefore, achieving a selectivity for dihydrogenphosphate or AMP anions in the presence of the other competing species is not straightforward.

Recently, Butler and co-workers [75] have developed two macrocyclic receptors based on a cyclen scaffold, functionalized with a steric demanding 8-(benzyloxy)quinoline pendant arm able to coordinate Eu (III) (complexes **46** and **47**). The 8-(benzyloxy)quinoline pendant arms take part in coordinating the Eu(III) centre in the axial site, occupying the top of the receptor, also acting as an antenna and therefore providing an efficient sensitization of the Eu(III) emission. Furthermore, in order to achieve multi-site recognition, the 8-(benzyloxy)quinoline moiety of **47** is functionalized with a boronic acid function. This provides reversible interactions between the boronate ester and the ribose sugar of AMP, supporting the coordination of the phosphate moiety to the Eu(III) center. Upon the addition of AMP, ADP, and ATP (10 mM HEPES at pH 7.0), both receptors showed an enhancement of the Eu(III) emission intensity more pronounced for AMP. The higher selectivity towards AMP was particularly evident for **47**, which showed a 4-fold enhancement in overall Eu(III) emission intensity (Fig. 22B–D). In both **46** and **47**, the steric hindrance generated by the quinoline moiety, combined with the high rigidity of the anion binding site, prevents efficient coordination by ATP and ADP, resulting in the selectivity order AMP > ADP > ATP, which is reversed with respect to that generally observed. The two receptors also show good selectivity for the phosphate anion and no response in the presence of HCO_3^- and lactate anions. Based on its promising binding properties, **47** was applied to detect inorganic phosphate in human serum samples and to monitor the enzymatic production of AMP in real-time.

In a second article by Butler and co-workers, the influence of the position of the phenylboronic acid group on the binding properties was investigated, comparing the behaviour of **47** with its *o*- and *p*-isomers (**48** and **49**) [76]. The results show that, like **47**, the *p*-isomer has higher selectivity to AMP over ATP, though it has a lower level of discrimination between AMP and ADP. Interestingly the *o*-isomer, due to the direct coordination of the phenylboronic acid to the Eu(III) centre, shows no response upon the addition of anions.

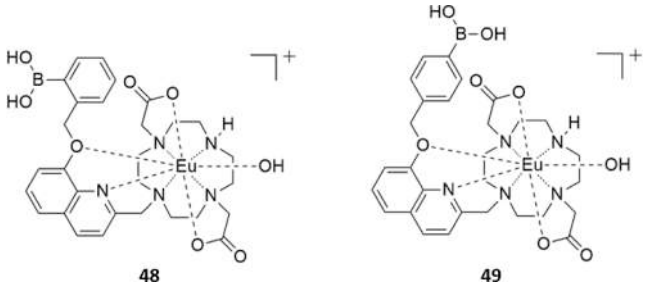

48 **49**

Although lanthanide-based receptors show a great affinity for oxyanions, the detection of other anionic species has also been investigated [77–80]. Faulkner and co-workers developed a family of binuclear lanthanide complexes able to bind chloride in aqueous solutions (**50**–**55**) [81]. The probes consist of two macrocyclic ligands bridged by flexible ethane (C-2) and propane (C-3) linkers and complexed by lanthanide metals (Eu(III), Tb(III), and Yb(III)), resulting in coordinatively unsaturated neutral binuclear complexes. These are preorganized to form a pocket between the lanthanide centers able to host halide anions coordinated to the metals. The binding process has been investigated by ^{35}Cl NMR at different temperatures (298 K, 304 K, 311 K, and 317 K) and via luminescence spectroscopy. The systems show a response upon the addition of F^- and Cl^- under physiological conditions and no observable changes towards competing halides, such as Br^- and I^-. Also, Cl^- binding involves chelation in the equatorial position between the metal centres. The association with Cl^- anions was also evaluated by high-resolution ESI-Mass spectrometry, supporting the formation of ternary complexes $[Ln_2(ligand)_2C\text{-}2(m\text{-}Cl)]^-$ and $[Ln_2(ligand)_2C\text{-}3(m\text{-}Cl)]^-$.

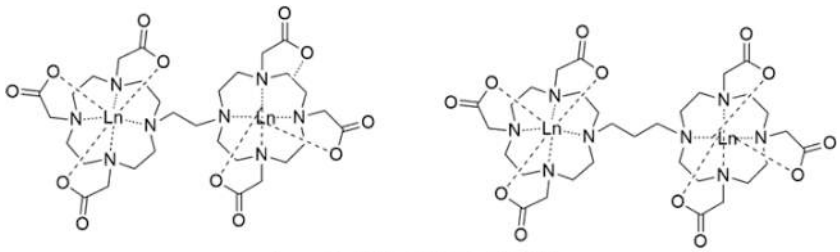

Ln = Eu(III), Tb(III), Yb(III)

50-56

Metal-organic frameworks (MOFs) represent an extensively investigated class of crystalline materials with different potential applications, such as gas storage, separation, and catalysis, to cite a few. The possibility to choose among a variety of metals and linkers and, therefore, design and tailor the porosity with specific H-bond donors and acceptors makes this class of materials extremely versatile. Several examples of MOFs which have been used for the detection of different anion species have been recently reported [72,73,77,79,80,82–86].

Mahata and co-workers developed a chelidamic acid - Y(III)/Mn(II) heterobimetallic MOF (**57**) for the selective detection of phosphate (Fig. 23) [87]. The system was fully characterized by single-crystal X-ray diffraction, FT-IR, UV–Vis spectroscopy, thermal gravimetric analysis (TGA), Brunauer–Emmett–Teller (BET) analysis, PXRD, and steady-state and time-resolved photoluminescence studies. Characterization by BET analysis and TGA provided information about the porosity, dehydration, and thermal stability of **57**. Structural determination by single-crystal X-ray diffraction shows the presence of hydroxyl-functionalized pockets (Fig. 23A), representing potential binding sites. Irradiation of an aqueous dispersion of **57** at 280 nm shows an emission peak at 388 nm, attributed to the intraligand transitions ($\pi^* \rightarrow \pi$ and $(\pi^* \rightarrow n)$. The sensing ability of **57** was investigated in the presence of different anions (I^-, Cl^-, F^-, Br^-, NO_3^-, NO_2^-, SO_4^{2-}, $C_2O_4^{2-}$, ClO_4^-, CH_3COO^-, and PO_4^{3-}). The system provided a significant response only in the presence of PO_4^{3-}, showing a 4-fold increase of the luminescent intensity (concentration up to 62.5 μM), with a calculated LOD of 0.2 μM (Fig. 23, B). Furthermore, **57** proved to be highly selective for PO_4^{3-} (Fig. 23, C). The stability of **57** in aqueous media and also in the presence of PO_4^{3-} was investigated by PXRD, proving that the crystal structure remains unchanged after the detection process. The phosphate interacts with the hydroxyl-functionalized pockets, determining an enhancement of the luminescent emission.

6. Charged chemosensors

Through protein engineering, Dodani and co-workers have developed a turn-on fluorescent chloride sensor (**58**, Fig. 24) from rhodopsin GR, a light-driven proton pump derived from *Gloeobacter violaceus* [88]. To form a Cl^- binding site, the D121 position was mutated by substituting valine for aspartate, thereby changing the counterion of the phenolate chromophore. When Cl^- was added (as NaCl, 400 mM) to a system of **58** (~3 μM) and buffered to pH 5 with acetate and gluconate (50 and 600 mM, respectively, as NaX salts), the pK_a of the sensor shifted from 3.1 ± 0.1 towards the protonated state, 4.8 ± 0.1. Under the same conditions, a pH-dependent, red-shifted fluorescent response was observed for Br^-, I^-, and NO_3^-, while no fluorescent response was observed when $H_2PO_4^-$ was added to the system as the NaX salts (400 mM). The dissociation constants of **58** with NaCl, NaBr, and NaI were K_d = 204 ± 41, 194 ± 14, and 170 ± 34 mM, respectively, and interestingly, the NaCl LOD of **58** was calculated at 12.5 mM. The authors used a series of single and bulk cell *in vitro* fluorescence studies on *E. coli* expressing both the cyan fluorescent protein (CFP) and the **58** mutations, which revealed that **58** senses the changing extracellular Cl^- concentration and ruled out interference caused by perturbed membrane potential or the transmembrane ion transport facilitated by **58**. Interestingly, when **58** was encapsulated in detergent micelles under aqueous conditions, the sensor was also capable of detecting changes in the extracellular Cl^-.

Qi and co-workers have synthesised two charged chemosensors, **59** and **60**, containing a carboxyl and sulfinyl group, respectively, which are soluble in both an aqueous and cytomembrane environments [89]. Using UV–Vis studies, both **58** and **59** (10 mM) were capable of sensing HSO_3^- in water with detection limits of (4.59 and 8.19 nM, respectively) causing a colour change from blue to colourless. When added to a phosphate buffer solution (PBS) buffered to pH 7.1 containing HSO_3^-, SCN^-, N_3^-, ClO_4^-, HSO_4^-, $H_2PO_4^-$, AcO^-, I^-, Br^-, Cl^-, and F^- (10 μM, as NaX salts), each probe (10 μM) only HSO_3^- elicited a significant response. The maximum fluorescence absorbance of **58** and **59** was 645 and 662 nm, respectively, while the fluorescence emission was 375 and 415 nm, respectively. The large Stokes shift of ~250 nm was observed, effectively weakening probe auto-fluorescence and self-absorption, resulting in a heightened sensitivity to the HSO_3^- anion. The authors determined the fluorescence quantum yields of **58** and **59** to be 0.251 and 0.167, respectively. The sensing mechanism operates via the addition of HSO_3^- to the electron-deficient carbon–carbon double bond, which inhibits ICT and, subsequently, a distinct colour change from blue to colourless. The toxicity of the probes (0–10 μM) in B16-F10 cells showed **58** was less cytotoxic than **59**. Notably, the higher biocompatibility of **58** could lead to potential applications of this HSO_3^- sensor in delicate biological or environmental systems.

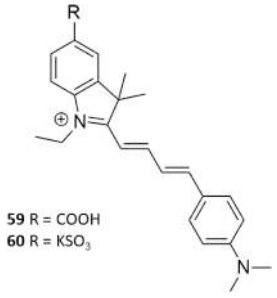

Dong and co-workers report the synthesis of a CN^- sensitive coumarin-connected carboxylic indolium near-infrared (NIR) turn-off sensor (**61**) that is both cytomembrane permeable and water-soluble [90]. The sensor was prepared in a 73 % yield following a three-step synthesis. The anion selectivity of **61** (10 μM) was evaluated via both UV–Vis spectrophotometry and Fluorescence studies in an aqueous solution buffered with Tris-HCl (0.01 M), adjusted to pH 7.2. The solution contained 50 equivs. of the following anions, SCN^-, N_3^-, CN^- (added as NaX salts) and ClO_4^-, HSO_4^-, $H_2PO_4^-$, AcO^-, I^-, Br^-, Cl^-, F^- (added as TBA salts). Only in the presence of CN^- (with a LOD of 4.44×10^{-7} mol L^{-1}) did fluorescence quenching occur. The result was an observable colour change from blue (584 nm) to colourless (425 nm) due to ITC disruption caused by CN^- addition to the π-conjugated indolium vinylene unit. Using the MTT assay, a B10–F10 cell viability of < 85 % was achieved with **61** concentrations of 0.01–50 μM, indicating potential use in biological or environmental CN^- sensing.

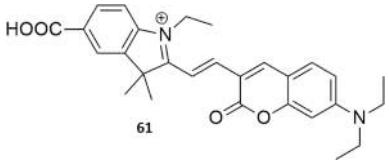

Ghosh and co-workers have reported the synthesis of **62** (Fig. 25), an Ir(III) complex functionalised with 2-phenylpyridine and 3,3′-([2,2′-bipyridine]-5,5′-diylbis(methylene))bis(1-ethyl-1H-imidazol-3-ium), in a 77 % yield [91]. Single crystal X-ray diffraction revealed **62** formed a $2PF_6^-$ complex and maintained a distorted octahedral geometry in the solid-state (Fig. 25). PL anion competition assays, performed in CH_3CN at 298 K, showed that **62** (10 μM) acts as a selective lifetime-based luminescent $H_2PO_4^-$ and $HP_2O_7^{3-}$ (2 and 1 equiv., respectively) chemosensor in the presence of ClO_4^-, I^-, Br^-, NO_3^-, HCO_3^-, Cl^-, AcO^-, HSO_4^-, NO_2^-, BzO^-, and F^- (10 equivs., as TBA salts). Further analysis of the PL titration data produced $H_2PO_4^-$ ($K_1 = 6.1 \times 10^4$ and $K_2 = 1.1 \times 10^4$ M^{-1}) and $HP_2O_7^{3-}$, ($K_a = 7.94 \times 10^4$ M^{-1}) binding constants. Interaction between **62** and $H_2PO_4^-$ or $HP_2O_7^{3-}$ causes a blue-shift in emission from 615 to 577 or 579 nm, respectively. A 13.7- ($H_2PO_4^-$) and 8.5-fold ($HP_2O_7^{3-}$) PL intensity increase was also observed alongside an increase in lifetimes (τ) (0.03543–0.2736 or 0.1323 μs, respectively). Proton-NMR titrations were used to study the anion recognition mechanism of **62** (7 mM) in DMSO-d_6 at 298 K and revealed hydrogen-bonding interactions between $H_2PO_4^-$ or $HP_2O_7^{3-}$ and the imidazolium C–H moiety.

Importantly, the LOD of **62** for $H_2PO_4^-$ and $HP_2O_7^{3-}$ was at sub-micromolar levels and calculated to be 0.040 and 0.035 μM, respectively.

7. Anion sensing using excimers

Ma and co-workers have synthesized a series of pyrene-labelled sequence-controlled polymers (SCPs) using living anionic polymerization (LAP) [92]. Three monomers, 4-(3-butenyl)styrene (**63**), 4-(5′-pentenyl)-diphenylethylene (**64**), and 3-mercaptopropanoate-oxymethyl pyrene (**65**), were synthesized in 72, 55, and 79 % yields, respectively. The steady-state fluorescence spectrum of pyrene-labelled SCPs with average chain lengths of 0, 10, 20, 40, and 60 exhibited a near-linear relationship between monomer emission intensity (378 nm) and excimer emission intensity (481 nm). Molecular Dynamics (MD) simulations using the DPSBD method were shown to accurately describe the luminescent properties of SCPs in statistical sequences observed in experiments.

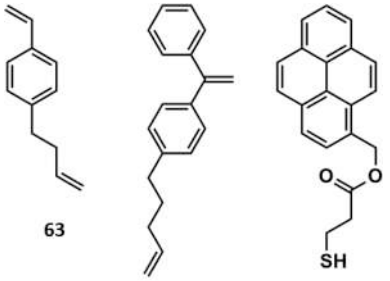

Menezes and co-workers synthesized two fluorescent naphthalene- (**66** and **67**) and pyrene-substituted (**68**) (thio)ureido-hexahomotrioxacalix[3]arene-based chemosensors in 53, 71, and 83 % yields, respectively [93]. The receptors formed 1:1 host:guest complexes via hydrogen bonds with NO_3^-, HSO_4^-, ClO_4^-, AcO^-, BzO^-, I^-, Br^-, Cl^-, and F^- anions (as TBA salts) and were analyzed using ^1H NMR, UV–Vis, and fluorescence titrations (0–10 equivs.). Proton-NMR titrations of **66**–**68** (2.5×10^{-3} M) in $CDCl_3$ at 298 K showed K_a constants increased with anion basicity with AcO^-, BzO^-, and F^- showing the strongest binding to **68** ($K_a = 3.42$, 3.45, and 3.31 M^{-1}). Fluorescence titrations of **68** exhibited monomer (398 nm) and excimer (498 nm) fluorescence with lifetimes of 1.98 and 25.9 ns, respectively. Using UV–Vis absorption studies in CH_2Cl_2 and CH_3CN, binding constants were derived for **66**–**68** ($1–2 \times 10^{-5}$ M) where, in general, the increased anion basicity of AcO^-, BzO^-, and F^- resulted in the highest K_a values of the series. Both **66** and **68** were more efficient than the naphthyl-thiourea **67**, with thermodynamic data showing that the binding of **68** to AcO^- and F^- was driven by entropy. Computational studies using the GFN2-xTB method with ALPB, where geometry-minimized structures were further optimized using the dielectric constant of CH_3CN, showed CH_3CN molecules were directly involved in anion binding via dispersion forces or hydrogen-bonding interactions. It was also seen that the entropy and enthalpy of the system decreased proportionally with the increase in CH_3CN molecules.

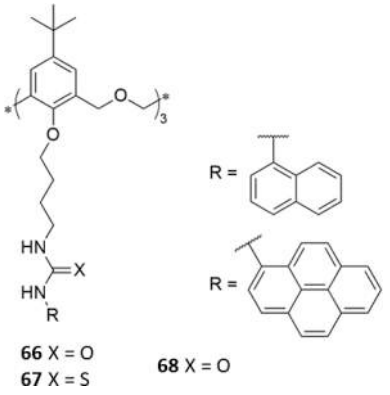

Chen and co-workers synthesized a porous hydrogen-bonded organic framework (HOF), **69**, from the hydrogen-bond driven self-assembly of 3,3′,5,5′-tetrakis-(4-carboxyphenyl)-1,1′-biphenyl (Fig. 26A) [94]. Powder X-ray diffraction (PXRD) showed the three-dimensional (3D) framework was a single pure phase with a BET surface area and solvent filling space calculated to be 2066 m^2g^{-1} and 56 %, respectively (Fig. 26B). The fluorescent emission of **69** was seen to be concentration dependant with the emission of the solid (392 nm) red-shifting to 359 nm when suspended in ethanol. Further dilution decreased excimer formation and a blue-shifted emission (369–359 nm). Sensing experiments exhibited significant fluorescence quenching when Fe^{3+}, Cr^{3+} (added as nitrate salts), and $Cr_2O_7^{2-}$ (added as the sodium salt) ions were added to a **69** ethanol suspension and revealed Fe^{3+}, Cr^{3+}, and $Cr_2O_7^{2-}$ with LODs of 0.689, 2.516, and 1.638 μM, respectively. The fluorescence resonance energy transfer and competitive absorption mechanisms account for the fluorescence quenching of Fe^{3+} and $Cr_2O_7^{2-}$, while the electron transfer quenching mechanism is also attributed to Fe^{3+} and Cr^{3+}. During fluorescence titrations, **69** (5 mg/100 mL) exhibited high selectivity for dopamine (10 mM) via fluorescence quenching in phosphate buffer solution with a pH range of 2–6 and revealed a LOD of 36.57 mM. Importantly, tests using fetal bovine serum biological samples containing dopamine at different concentrations showed that **69** is capable of quantitative dopamine recoveries of 101.1 % to 104.9 %.

Hayashida, Imamura, and Miyazaki have reported the synthesis and characterization of an anionic cyclophane (**70**) containing a reduction-responsive disulfide linkage and a fluorescent pyrene substituent [95]. In an aqueous polar environment containing a carbonate buffer (pH 10), self-inclusion of the pyrene moiety into the host cavity of **70** (10 μM) was observed with monomer emissions at 377, 398, and 420 nm. In the same system, over 30 min, the reduction and subsequent cleavage of the disulfide linkages in **70** upon contact with glutathione (GSH, 0.5 mM) generates the tetra-anionic thiolate cyclophane. The cleaved amphiphilic pyrene then self-aggregates, producing a fluorescent excimer response at 480 nm. The polarity-dependant behaviour of **70** (0.5 mM) was analyzed via ^1H NMR at 298 K by altering the D_2O/CD_3OD *v/v* ratios from 1:9–8:2 and showed that at higher water contents, self-inclusion of the pyrene unit increased. The increased self-inclusion was accompanied by the pyrene, aromatic cyclophane, and methylene cyclophane protons shifting up-field. The authors also analyzed the concentration-dependent behaviour of **70** (0–20 μM) in the aqueous carbonate buffer (pH 10 at 298 K) and showed that below concentrations of 1×10^{-5} M, **70** exists as monomers, excimer emission at 480 nm was observed at higher concentrations.

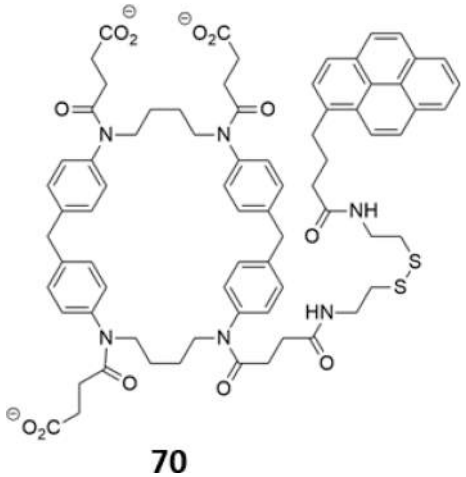

70

Ghosh and co-workers have developed a fluorescent tetramide chemosensor (**71**) for $HP_2O_7^{3-}$ using a dipyrromethene scaffold via a four-step synthesis in a 70 % yield [96]. Fluorescence studies of **71** (2.5×10^{-5} M) dissolved in CH_3CN/DMSO (1 %) showed a strong excimer emission peak at 450 nm when $HP_2O_7^{3-}$ (40 equiv., as the TBA salt) was

incrementally titrated to the system. However, no excimer-based fluorescence was observed upon addition of NO_3^-, HSO_4^-, $H_2PO_4^-$, AcO^-, I^-, Br^-, Cl^-, and F^- ($1{\cdot}10^{-3}$ M, as TBA salts). From the fluorescence titrations, an $HP_2O_7^{3-}$ binding constant of $3.2 \times 10^3\ M^{-1}$ was found and had a detection limit of $2.08 \times 10^{-5}\ M^{-1}$. The anion sensing ability of **71** was investigated using UV–Vis titrations in CH_3CN/H_2O (3:1, *v/v*) with DMSO (1 %). High selectivity for $HP_2O_7^{3-}$ was observed, accompanied by a red-shifted emission (365–420 nm), with a binding constant and detection limit of $4.20 \times 10^3\ M^{-1}$ and 1.68×10^{-5} M, respectively. DFT studies using a 6–31G(d) basis set and a dispersion corrected B3LYP-D3 hybrid function revealed the *syn*- and *anti*-form of **71** were equilibration CH_3CN, with the low-energy *syn*-form, being preferred during $HP_2O_7^{3-}$ binding. It was also found that anion-binding in the *syn*-form caused the naphthalene-substituents of **71** to be close, allowing π–π stacking to occur, resulting in the experimentally observed enhanced excimer fluorescence.

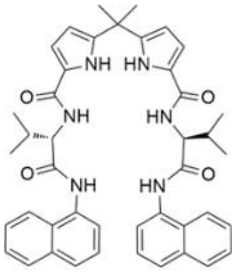

71

8. Anion-π interaction in sensing

George and co-workers have reported on the synthesis, characterization, and emissive charge-transfer (CT) states promoted by anion–π interactions of a dibromo-substituted dicationic pyrometallic diimide (**72**, Fig. 27) [97]. The interaction between the **72** core and two bound I^- anions in an aqueous solution allowed ground-state CT absorption to occur, resulting in the observed CT fluorescence at 560 nm from the singlet CT state (^{1}CT). Similar interactions were seen in the solid-state using single crystal X-ray diffraction, revealing both I^-–π (Fig. 26) and Br^-–π halogen-bonding interactions. Similarly, when supramolecular scaffolds of laponite (LP) were used to organize **72** into interlayer galleries, triplet-state phosphorescence was observed. Importantly, further steady-state and time-gated spectroscopic studies revealed the dual phosphorescence of the locally excited triplet-state (^{3}LE, at 470 nm) and the anion-π triplet CT state (^{3}CT, at 550 nm).

Ghosh, Mondal, and Rashid have developed a Ru(II)-based chemosensor, **73**, that contains a π-acidic pentafluorophenyl and a halogen-bonding iodotriazole moiety as the $2PF_6^-$ salt through a three-step synthesis in a 69 % yield (**73**•$[PF_6]_2$ (Fig. 28A) [40]. Single crystal X-ray diffraction revealed self-assembled polymeric chains of **73**•$[H_2PO_4]_2$ in the solid state due to coordination with $H_2PO_4^-$ anions via anion-π, halogen-bonding, and anti-electrostatic anion-anion interactions (Fig. 28A). Using DLS, transmission electron microscopy (TEM), and scanning electron microscopy (SEM) revealed polymeric structures in the presence of $H_2PO_4^-$. However, in the presence of ReO_4^-, supramolecular aggregation is observed, which is corroborated by dimeric solid-state structures of **73**•$[ReO_4]_2$ (Fig. 28C). Proton-NMR titrations in DMSO-d_6 at 298 K revealed no significant interactions between **73** or $H_2PO_4^-$ and $HP_2O_7^{3-}$ (as TBA salts, 0–1.5 equivs.), whereas chemical shifts of $\Delta\delta = 0.4$ and 0.6 ppm for $H_2PO_4^-$ and $HP_2O_7^{3-}$, respectively, during ^{31}P NMR, were indicative of phosphate–triazole halogen-bonding interactions, respectively. Similarly, up-field shifts were observed during ^{19}F NMR experiments when $H_2PO_4^-$ was added, indicative of anion-π interactions, while no shifts were observed when either ReO_4^- or $HP_2O_7^{3-}$ was added. Excitation of **73** at 402 and 441 nm in CH_3CN during UV–Vis studies resulted in an emission at 590 nm, corresponding to the metal-to-ligand charge-transfer (MLTC) ^{3}MLTC luminescence band. Out of Cl^-, Br^-, I^-, HSO_4^-, NO_3^-, F^-, AcO^-, BzO^-, HCO_3^-, OH^-, ReO_4^-, $HP_2O_7^{3-}$, and $H_2PO_4^-$ only the addition of $H_2PO_4^-$, $HP_2O_7^{3-}$, and ReO_4^- significantly increased emission intensity, with a 25-, 3.6-, and 1.2-fold increase, respectively. Using photoluminescence titrations in CH_3CN, the detection limits of **73** for $H_2PO_4^-$ and $HP_2O_7^{3-}$ were ~0.011 and ~0.091 μM, respectively.

9. Photoswitchable chemosensors

The possibility of using light to change the conformation of receptors and enhance their ability to sense anions is continuing to be of great interest in supramolecular chemistry [98–102]. Wezenberg and co-workers have synthesised a photoswitchable strapped calixpyrrole (**74**), which contains a stiff-stilbene photoswitchable moiety [103]. This system, as its *Z*-isomer, can bind Cl^- anions with a remarkable 8000-fold higher affinity than the *E*-isomer ($K_a = 1.6 \times 10^6\ M^{-1}$ and $K_a = 2.0 \times 10^2\ M^{-1}$ for the *Z*- and *E*-isomer, respectively). Photoisomerization from *Z* to *E* can be achieved by simply irradiating a solution of the sample in DMSO or CH_3CN at 365 nm. The isomerisation results in changes in the absorbance properties of **74,** which can be reversed by irradiating at 340 nm.

Wezenberg, in collaboration with Beves, has reported that the stiff-stilbene photoswitchable compound **75** binds anti-electrostatic $H_2PO_4^-$ oligomers via H-bonds [104]. The binding ability of **75** was studied via DOSY-NMR experiments. The diffusion rate of **75** is slower by 7 % in the *E*-isomer than in the *Z*-isomer. This is due to the fact that the *E*-isomer is more elongated. In the presence of $H_2PO_4^-$ oligomers, which form in DMSO solution at a concentration of 50 mM, the diffusion rate of the adducts of **75** and the oligomers decreases by 33 % and 26 % for the *E*-isomer and the *Z*-isomer, respectively. This means that in the presence of the anion, there is an enhancement of the change in diffusion upon photoisomerization, opening interesting perspectives toward the directional motion of the receptor driven by light or concentration gradient.

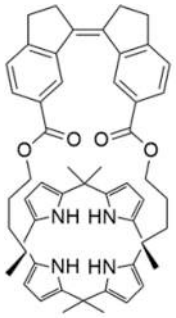

74 (*Z*-isomer)

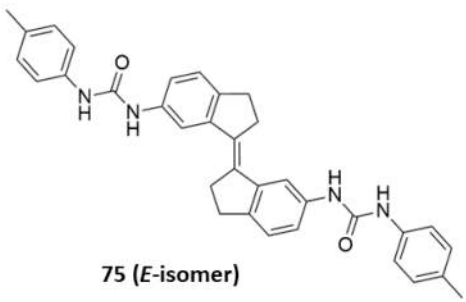

75 (*E*-isomer)

A new class of photoswitchable anion receptors containing a guanidinium moiety have been recently reported by Custelcean, Moyer and co-workers [105]. Receptor **76**, as its triflate salt, exists as either the *E,E*- or *Z,Z*-isomer, and the two can reversibly photoswitch when irradiated with a UV light (Hg vapour lamp). The *E,E*-isomer can bind SO_4^{2-} via H-bond formation and shows an affinity 5 orders of magnitude higher than that of the *Z,Z*-isomer (Log $K_{11} = 7.25$ and Log $K_{11} = 1.85$ for the *E,E*- and the *Z,Z*-isomer, respectively) as demonstrated by UV–Vis and ^{1}H NMR titrations in DMSO-d_6. Receptor **76** is also able to form adducts with 1:2 stoichiometry with SO_4^{2-} when an excess of anion is present in the solution. Interestingly, the authors developed a photo-induced anion-separation process, as shown in Fig. 29. In the presence of a high concentration of SO_4^{2-} in DMSO, the adduct formed with the *E,E*-isomer immediately precipitates. However, upon irradiation (or heating), the receptor converted back to the *Z,Z*-isomer, allowing the SO_4^{2-} to redissolve.

10. Chemodosimeters

When a receptor reacts with a specific analyte, and the reaction causes a change in the colorimetric or fluorescence properties of the system, the sensor is referred to it as a chemodosimeter. Various examples of chemodosimeters for fluoride sensing have been recently reported [106–108].

Chemodosimeters **77**–**80** contain a silyl fragment which is released upon the addition of fluoride, causing dramatic changes in the fluorescent emission of the system (see Fig. 30B and C in the case of **80**). In particular, the emission band at around 380 nm ($\lambda_{exc} = 300$ nm) of compound **80** increased in the presence of fluoride in a THF solution, but it was unaffected by other anions (Fig. 30A). The mechanism of the sensing was demonstrated by ^{1}H NMR titrations in $CDCl_3$ at 298 K.

A carborane-based chemodosimeter for fluoride was reported by Lee and co-workers in which the reaction triggered by fluoride is a deboronation that causes an enhancement of the fluorescence emission in a THF/H_2O (1:1, *v/v*) mixture [109]. Examples of chemodosimeters for CN^- sensing have also been described in the last two years, based on nucleophilic addition of cyanide to cyano vinyl moieties as in the case of compounds **81** [110] and **82** [73], nucleophilic addition to the indolynium group, as in the case of compound **83** [111], or deprotonation of the OH moiety as in the case of compound **84** [112].

Compound **85** can sense CN^- via nucleophilic aromatic substitution of three cyanide groups on the dinitrophenyl-substituted ring. In the UV–Vis spectrum of **9** in DMSO/H_2O (8:2, *v/v*), three bands appeared attributed to the mono, the bi-, and the tri-substituted derivative. The reaction is accompanied by a colour change of the solution from colourless to purple as well as a change in the emission properties of the system [113].

Gong, Chow, and co-workers described a novel approach in cyanide sensing and developed an interesting bimetallic system **86**, which is able to colorimetrically sense CN^- at pH 7 in phosphate buffer and then act as a catalyst to degrade it (Fig. 31) [114]. As described in Fig. 31, in compound **86**, the Fe(II)-diimine portion acts as a colorimetric indicator, and then, the Cu(II) complex is able to catalytically degrade the analyte to less toxic cyanate (OCN^-) in the presence of H_2O_2, offering the possibility to sense and detox a CN^- contaminated samples at the same time. The system is highly selective for CN^- over other interfering anions such as AcO^-, SO_4^{2-}, SCN^-, OCN^-, NO_3^-, and N_3^-. When supported on silicagel, the colour change was detectable by the naked eye and could degrade CN^- in real samples such as tap water, river water, and underground water with a LOD of 1.16×10^{-4} M.

An azulene-based chemodosimeter (**87**) for nitrite colorimetric recognition in CH_3CN/H_2O (1:1, *v/v*) at pH = 1 was reported by Wenk, James and Lewis (Fig. 32) [115]. The sensing mechanism is shown in Fig. 31 and consists of a diazotization of the amine moiety on the azobenzene followed by the formation of a diazoquinone (**88**, Fig. 32).

The proposed system is characterised by a high selectivity over other anions such as Cl^-, Br^-, I^-, HCO_3^-, HSO_3^-, PO_4^{3-}, NO_3^-, and, with respect to the standard Griess test for nitrite recognition requires only the preparation of one standard solution instead of three. Compound **87** was used to detect nitrite in cured meat, and the results obtained were comparable with those obtained using the current British Standard of testing. The LOD was 0.23 mgL^{-1}, which is below the maximum concentration allowed in drinking water (0.5 mgL^{-1}) in the European Community.

A turn-on chemodosimeter (**89**) for hydroxide recognition showing both a colorimetric and fluorimetric response was proposed by Mariappan and co-workers (Fig. 33, A) [116]. The anthraquinone macrocycle **89** in CH_3CN solution is able to react with 1 equiv. of TBAOH, causing the deprotonation of the macrocycle and a change in the colour of the solution, as shown in Fig. 33B. When an excess of TBAOH is present in the solution, a dramatic change in the emission

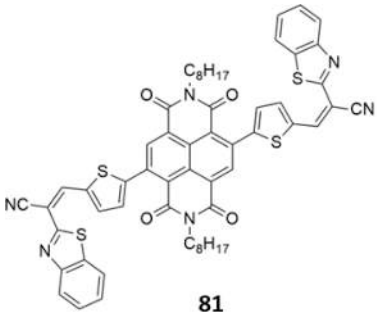

81

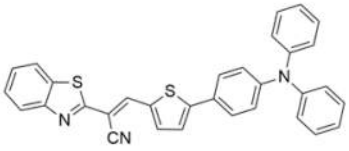

82

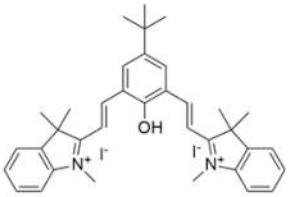

83

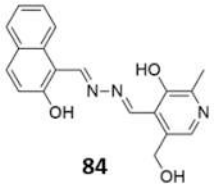

84

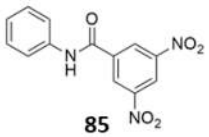

85

properties of the system occurs with the appearance of a green fluorescence emission at 515 nm (Fig. 33C) due to the keto-enol tautomerisation.

BODIPY derivative **90** was used for the fluorimetric and colorimetric superoxide detection in a solution of DMSO/PBS (2:8, *v/v*) at pH = 7.4 and in living cells (Fig. 34A) [117]. As reported in Fig. 5A, the addition of superoxide to **90** causes the cleavage of the phosphate bond and the formation of the highly fluorescent carboxylic acid **91**. BODIPY **90** was used to detect superoxide in living cells on RAW 264.7 macrophage cell line by means of fluorescence confocal microscopy, as shown in Fig. 33B. When cells were treated with two intracellular superoxide stimulators such as phorbol-12-myristate-13-acetate (PMA), (Fig. 34B, b1–b3) or bacterial endotoxin lipopolysaccharide (LPS), (Fig. 34B, c1–c3) and then BODIPY **90**, a bright green fluorescence was observed. On the other hand, if the cells were treated with LPS and then the intracellular ROS scavenger Trion, no fluorescence was observed (Fig. 34B, d1–d3).

A chemodosimeter (**92**) for hypochlorite (ClO^-) sensing was reported by Shiraishi and co-workers (Fig. 34A) [118]. Compound **92** is weakly emissive in a mixture of H_2O/CH_3CN (8:2, *v/v*) at neutral pH. As shown in Fig. 35B, upon the addition of 50 equivs. of ClO^- an intense green fluorescence developed. This was attributed to the oxidative cleavage of the imine bond in **92**, which caused the release of the naphthalimide derivative **93** and the subsequent switching on of the fluorescence (Fig. 35A). The reaction is highly selective, and all the other anions tested did not cause any changes in the emission properties of **92**. The chemodosimeter was also able to sense ClO^- in HeLa cells (Fig. 35C).

11. Anion sensing using arrays

Sensor arrays have recently gained attention as an emerging tool for the development of colorimetric and fluorescent probes, as suggested by the increasing number of examples recently reported in the literature [119–126]. Different from typical chemosensors that are designed to target a specific analyte, sensor arrays are composed of different groups of probes, allowing the simultaneous identification of different analytes. Each analyte interacts with a different probe, producing a typical fingerprint response that can be used to discriminate between multiple analytes [119,122].

Jolliffe and co-workers described an array system for the discrimination and classification of mono-, di-, and tri-phosphates [127]. The system is based on a cyclic peptide, functionalized with two Zn(II)–dipicolylamine (DPA) pendant arms (**93**, Fig. 35). When combined with pyrocatechol violet (PV), the 1:1 **93**·PV complex behaves as an indicator displacement assay (IDA) in the presence of phosphate species, as suggested by UV–Vis titration experiments. Complex **93**·PV exhibits changes in the UV–Vis spectra mainly in the presence of multivalent phosphates and no appreciable changes towards monophosphate and Pi, suggesting that the latter is not able to displace the indicator from the **93**·PV complex. These results prompted the development of an array-based system comprising six different sensing ensembles, obtained by combining **93** with PV, pyrogallol red (PGR), bromopyrogallol red (BPG), chromeazurol S (CAS), eriochrome cyanine R (ECR) and xylenol orange (XO) (Fig. 36A and B). The addition of the analyte to each sensor (equimolar amount of **93** and the respective indicator in HEPES) produced the absorption spectra shown in Fig. 36C.

The response was analyzed by multivariate data analysis. The principal component analysis (PCA), used to reduce the dimensionality of the data, showed clustering between the classes of monophosphates (nucleotide monophosphates and Pi), nucleotide diphosphates, nucleotide triphosphates, $HP_2O_7^{3-}$ (Fig. 37). These results were confirmed by linear discriminant analysis (LDA), which showed no overlap between the 95 % confidence ellipsoids for each class, highlighting the ability of the array to discriminate between different classes of phosphates.

Lin and co-workers developed a metallo-gel sensor array for the selective detection of different anions (I^-, N_3^-, CN^-) and amino acids (L-tryptophan and L-histidine) [128]. The authors synthesized a 3,4,5-tris (hexadecyl) benzoyl hydrazine-functionalized naphthalimide gelator (**94**), able to self-assemble into a stable supramolecular gel (Fig. 38A). Characterization of the self-assembly process by ^1H NMR, FT-IR, and XRD suggests that the gel formation involves mainly π–π stacking, together with hydrogen bonds and hydrophobic interactions. In the gel state ($T < T_{gel}$), **94** shows a strong blue-green fluorescence emission, while in the sol state ($T > T_{gel}$), the system shows no emission, suggesting that the self-assembly process results in an aggregation-induced emission (AIE). In the presence of anions, metallogels **94**·Fe^{3+}, **94**·Ca^{2+}, and **94**·Cu^{2+} were able to sense different anions (see Fig. 38B and C).

Furthermore, **94**·Fe^{3+}, **94**·Co^{2+}, and **94**·Ni^{2+} metallogels respond in the presence of the amino acids L-tryptophan (L-Trp) and L-histidine (L-His). A metallo-gel-based six-membered anion and L-amino acid sensor array was then developed. The system was successfully applied to sense I^-, N_3^-, and CN^- from aqueous solutions, also proving a response towards amino acids such as L-Trp and L-His. In particular, the limit of detection (LOD) for I^- was 3.38 nM.

Anzenbacher and colleagues recently described a sensor array for the quantitative detection of ATP [129]. The system is based on the three fluorescent carboxyamidoquinoline-based ligands described above (see metal-based chemosensors section) **43**–**45**. When complexed with Zn(II) in a 1:1 ratio, the fluorescent emission of **43**–**45** shows significant changes (Fig. 39).

The three complexes Zn(II) complexes are able to bind and sense different phosphate anions through a relay mechanism. As suggested by ^1H NMR spectroscopy, upon the addition of the phosphate analytes, the metal ion is, in most cases, displaced. This is also accompanied by a dramatic change in the optical properties of the system (Fig. 40A). In general, the three complexes towards different anion species (ATP, ADP, AMP, $HP_2O_7^{3-}$, PO_4^{3-}, Cl^-, Br^-, CH_3COO^-, SO_4^{2-}, and CN^-) show significant fluorescent changes only in the case of ATP, ADP, $HP_2O_7^{3-}$, and PO_4^{3-} species. However, when compared to Zn(II)·**43**, Zn(II)·**44**, and Zn(II)·**45** exhibit a slightly different selectivity in the presence of ATP and $HP_2O_7^{3-}$. On the basis of these results, a fluorescent sensor array was developed, and the response towards adenine nucleotides was tested. The results of the LDA show separate clustering only for ATP, ADP, $HP_2O_7^{3-}$, and PO_4^{3-}, highlighting the ability of the array to discriminate these species in the presence of AMP and the other anions (Fig. 40B). The ability of the array to quantify ATP with high sensitivity was also tested. The results show that the system allows highly accurate quantitation of ATP in unknown samples (range of concentration: 5–100 μM) with an error of less than 2.5 % (Fig. 40C).

12. Logic gates

Kurkuri and co-workers reported the study of three colorimetric chemosensors **95**–**97** [130].

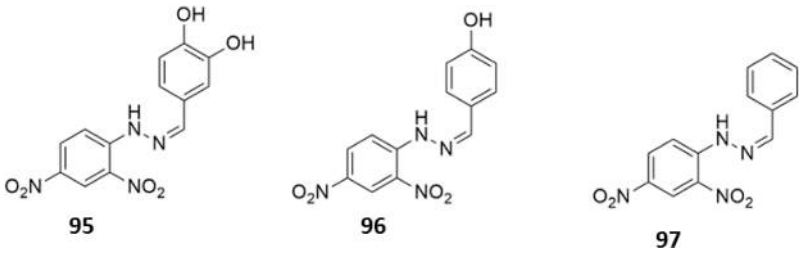

The optical response of **95**–**97** was tested through UV–Vis measurements in the presence of different anion species as their TBA salts. Interestingly, **95** was found to be able to bind the F^- over other anion species tested. Upon the addition of 2 equivs. of F^- and AcO^-, the characteristic absorption band centred at 417 nm decreased, accompanied by the comparison of a new band centred at 488 nm (Fig. 41A–B). The presence of F^- and AcO^- species also caused a colour change of the solution of **95** appreciable by naked eyes from yellow to red and pale red upon the addition of F^- and AcO^-, respectively (see inset Fig. 41A–B). On the other hand, while in the case of **96**, its behaviour was similar in the presence of both F^- and AcO^- species, receptor **97** was found to selectively bind AcO^- over F^-.

This behaviour was ascribed to the deprotonation event of the NH and OH groups into the chemosensors, accompanied by an intramolecular charge transfer process. Since reversibility is an important aspect of chemical sensors, it has been further studied in response to receptor **95**. As mentioned above, the presence of the F^- caused the comparison of a new absorption band centred at 488 nm with a colour change of the solution from yellow to red. As shown in Fig. 41, A, the addition of Cr^{3+} (as its nitrate salt) to this solution caused a colour reversion of the solution, turning from red to yellow. This reversible behaviour of **95** lasts up to 5 cycles (Fig. 42, B). The 'OFF-ON-OFF' behaviour was transferred into a logic molecular circuit, in which the ON state (Output = 1) was defined as the strong absorption at 488 nm due to the presence of F^- into the system, whereas the OFF state (Output = 0) represents no absorption at 488 nm, corresponding to the addition of the Cr^{3+} into the system. As shown in Fig. 42, C, the reversible and reconfigurable sequences of logic operations demonstrate the 'OFF-ON-OFF' functions with the optical output signals, which were utilised to mimic a molecular logic gate.

Arabahmadi reported a new hydrazone-based chemosensor **98** [131]. Its anion sensing capability towards different anion species was evaluated by spectrophotometric, spectrofluorimetric measurements and by ^1H NMR titrations in DMSO-d_6 at 298 K. The chemosensor was characterized by the presence of two absorption bands at 390 nm and 490 nm attributed to π–π* and n–π* transitions of the azomethine group, respectively. As shown in Fig. 43, upon the addition of an increasing amount of F^- (as the TBA salt), the decrease of the two characteristic absorption bands with the concomitant formation of a new absorption band centred at 513 nm was observed, accompanied by a dramatic colour change from red to purple (see inset of Fig. 43).

This behaviour was found to be ascribable to an initial interaction between **98** (Fig. 43) and F^-, followed by deprotonation upon the addition of an excess of F^-. Spectrofluorimetric measurements conducted in the same medium evidenced how the weak emission band of the chemosensor at 532 nm (λ_{ext} = 490 nm) underwent an enhancement upon the addition of an increasing amount of F^-, along with an enhancement of the quantum yield from 0.105 to 0.56. On the other hand, no significant changes were observed in the presence of the other anion species tested. Proton-NMR studies highlighted how, upon the addition of the F^-, the signals attributed to the NH and OH of the probe disappeared as a consequence of the deprotonation event, accompanied by an upfield shift of the aromatic signals (typical when deprotonation of the probe occurs). Interestingly, spectrophotometric and

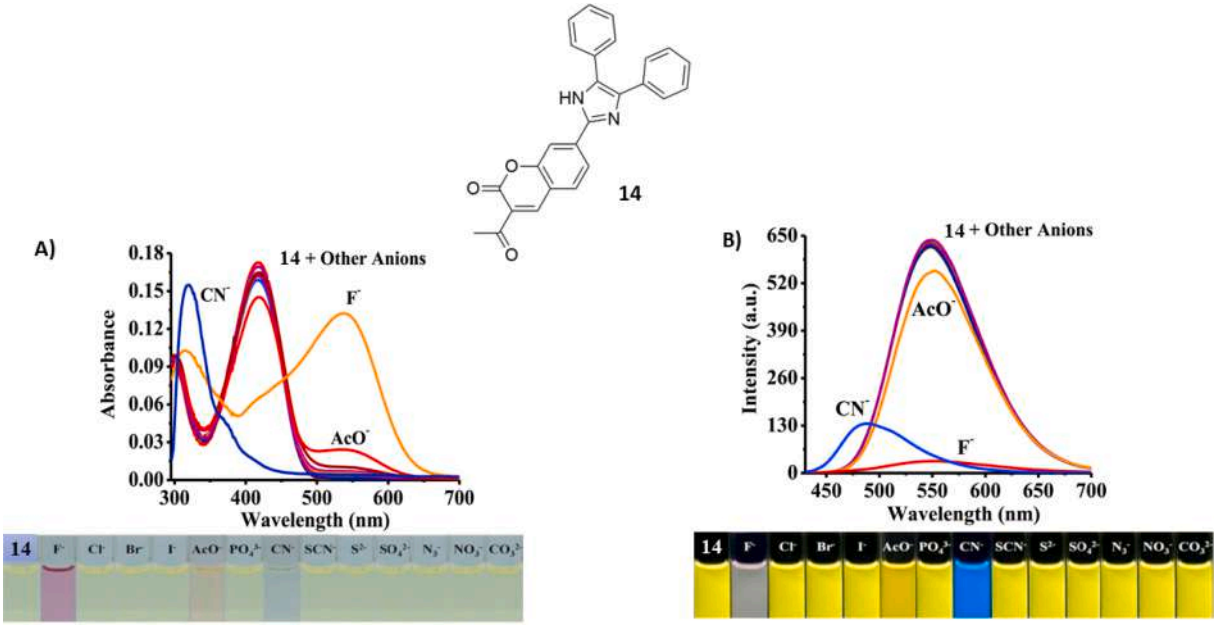

Fig. 9. A) Changes in the absorption spectrum of **14** in the presence of various anions in 1,4-dioxane; B) changes in the emission spectrum of **14** in the presence of various anions (as their TBA salts) added as a 1,4-dioxane solution. At the bottom of the figure, pictures of the changes in the colour of the solution of **14** in dioxane in the presence of 10 equivs. of various anions under daylight (left) and UV light (right). Reproduced with permission form Ref. [32]. Copyright Elsevier 2020.

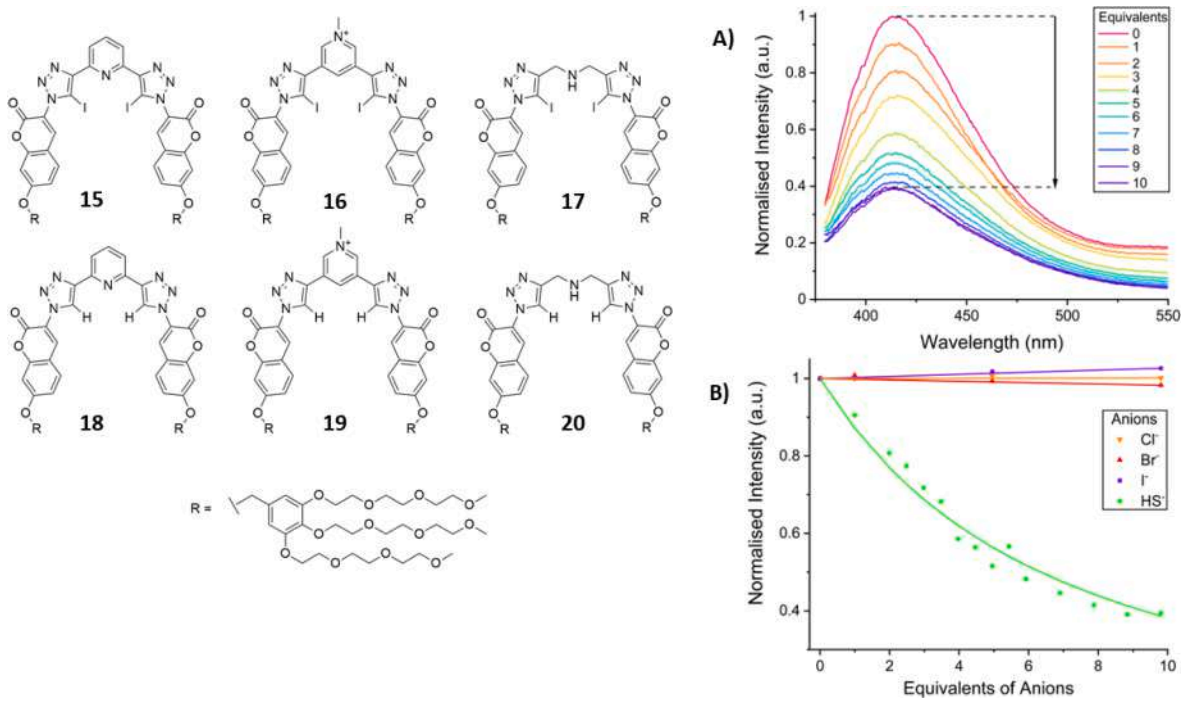

Fig. 10. A) Fluorescence titration of an aqueous solution of **15** (10 μM) with increasing amounts of NaSH, buffered with HEPES (10 mM) to pH 7.4). B) Binding isotherms and Bindfit analysis (λ_{max} 400–420 nm) of the data obtained from the fluorescence titration of **15** (10 μM) with increasing amounts of NaCl (yellow), NaBr (red), NaI (purple), and NaSH (green) (an aqueous HEPES (10 mM) buffer solution at pH 7.4). Adapted with permission from Ref. [39]. Copyright Wiley 2021.

spectrofluorimetric measurements conducted in the presence of different cation species evidenced how the presence of the Cu(II) caused the disappearance of the absorption band at 490 nm along with the concomitant formation of a new band at 400 nm, with an isosbestic point fixed at 439 nm (Fig. 44A). Moreover, the addition of the increasing amount of Cu(II) caused the quenching of the emission band at 532 nm. When compound **98** is excited at 490 nm, the emission band at 532 nm shows a bathochromic shift (Fig. 44b). Since the dual sensing of the probe towards F^- and Cu(II), the author decided to evaluate the response of the adduct with the F^- in the presence of the Cu(II) and the effect of the F^- to the complex **98**·Cu^{2+}.

The addition of an increasing amount of F^- to a solution of the

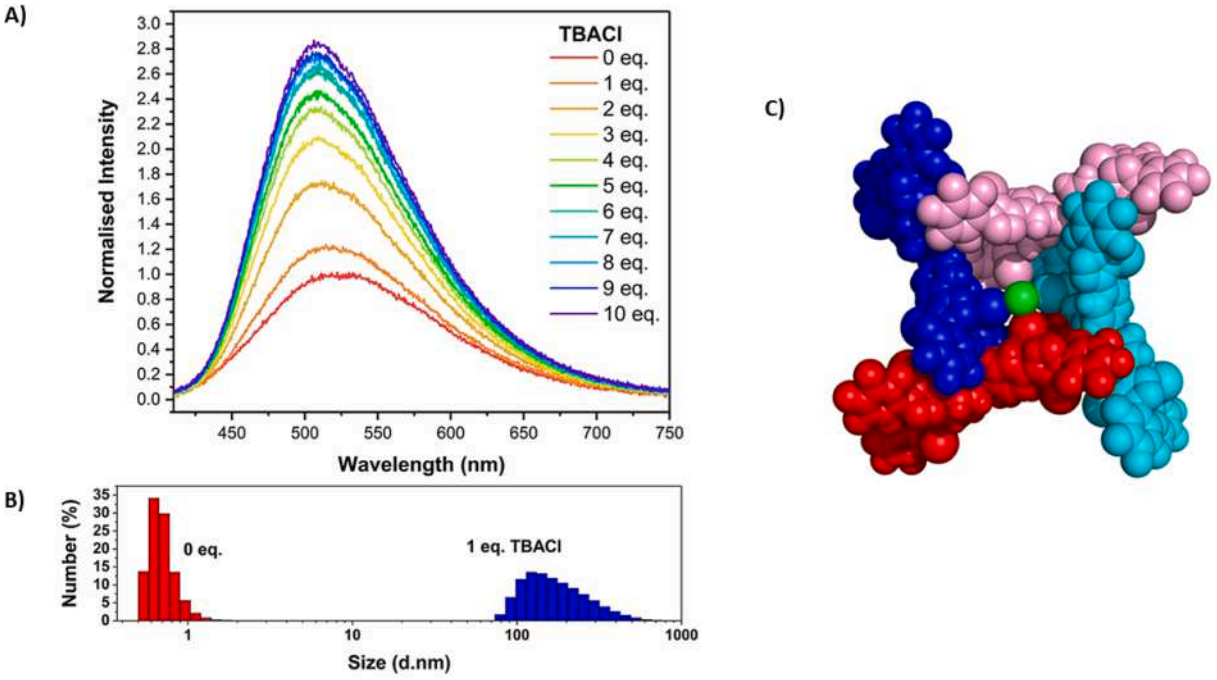

Fig. 11. A) Fluorescence emission of **25** in the presence of increasing amounts of TBACl (THF, 10^{-5} M, λ_{exc} = 350 nm); B) DLS measurements in the presence of 1 equiv. of TBACl (THF, 10^{-5} M); C) The single crystal X-ray structure of **25**·NaCl (space-filling style). Adapted with permission from Ref. [38]. Copyright Wiley 2021.

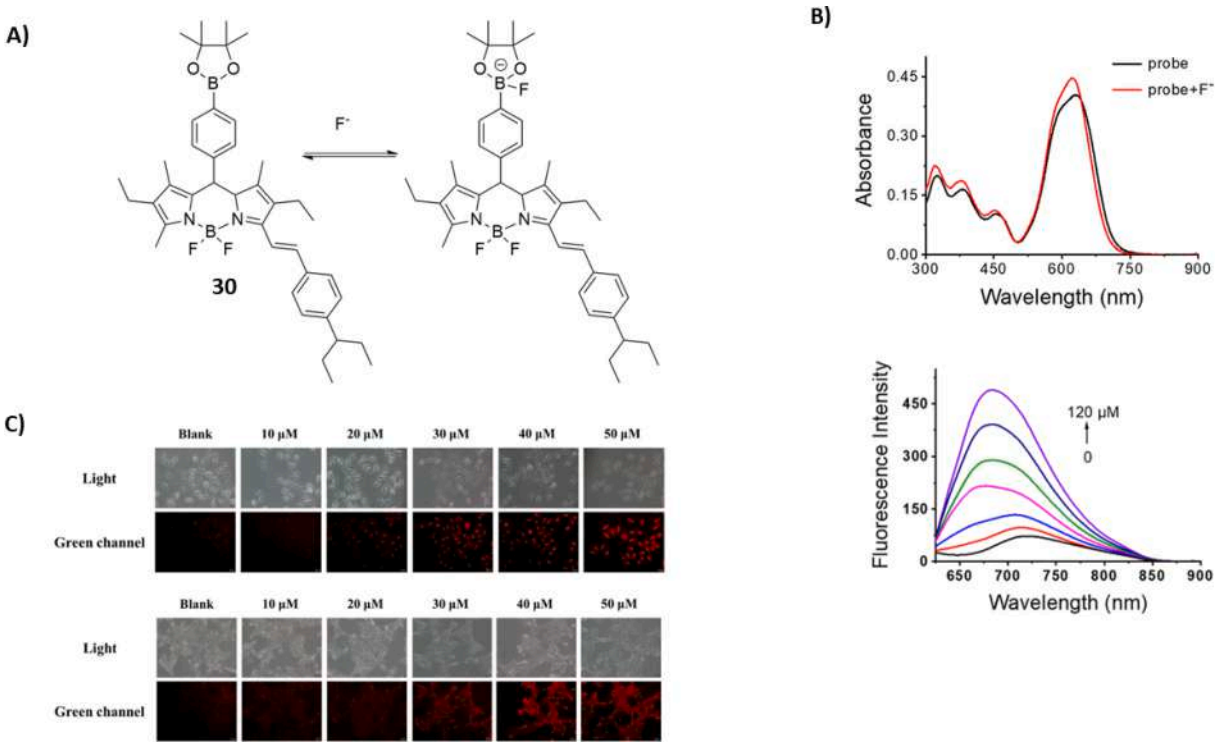

Fig. 12. A) The chemical structure of probe **30** and mechanism of detection of F^- (as its TBA salt). B) Top: absorption spectra before (black curve) and after (red curve) addition of F^- (100 μM); bottom: fluorescence spectra of **30** (10 μM) upon gradual addition (0–120 μM) of F^-. The growth medium was buffered to pH 7.4 using HEPES (10 mM) with CTAB (100 μM). C) Fluorescence images of **30**·F^- in HeLa cells (top) and 4 T1 cells (bottom). Scale bar: 20 μm, λ_{exc} (green channel): 460—550 nm. Adapted with permission from Ref. [43]. Copyright ACS 2022.

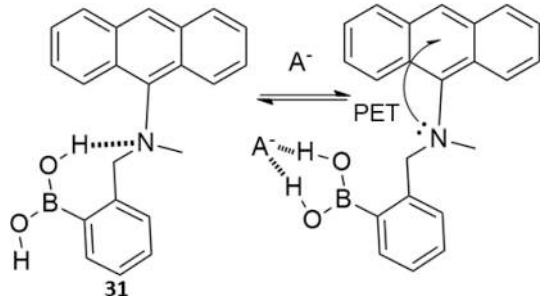

Fig. 13. The sensing mechanism proposed for chemosensor **31**.

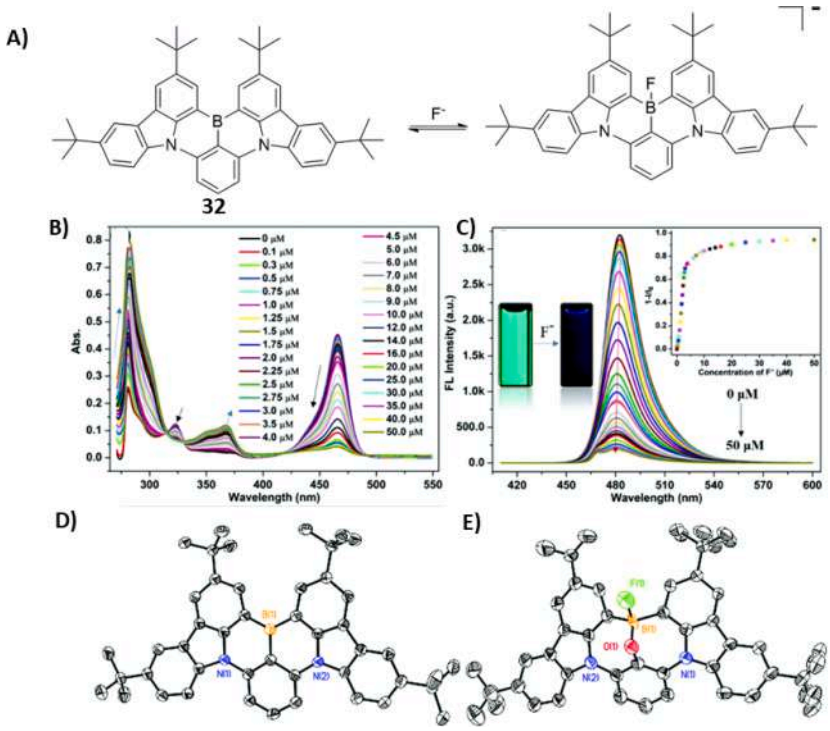

Fig. 14. A) Schematic representation of F^- sensing by **32**; B) UV–Vis spectra upon addition of increasing amounts of TBAF (50 μM) in THF. C) The fluorescence spectra after the addition of increasing amounts of TBAF in THF. D) The single crystal X-ray structures of **32** (CCDC: 2032277) and E) **32**·F^- (CCDC: 2032276†). All hydrogen atoms and TBA counter cations have been omitted for clarity. Adapted with permission from Ref. [46]. Copyright RSC 2021.

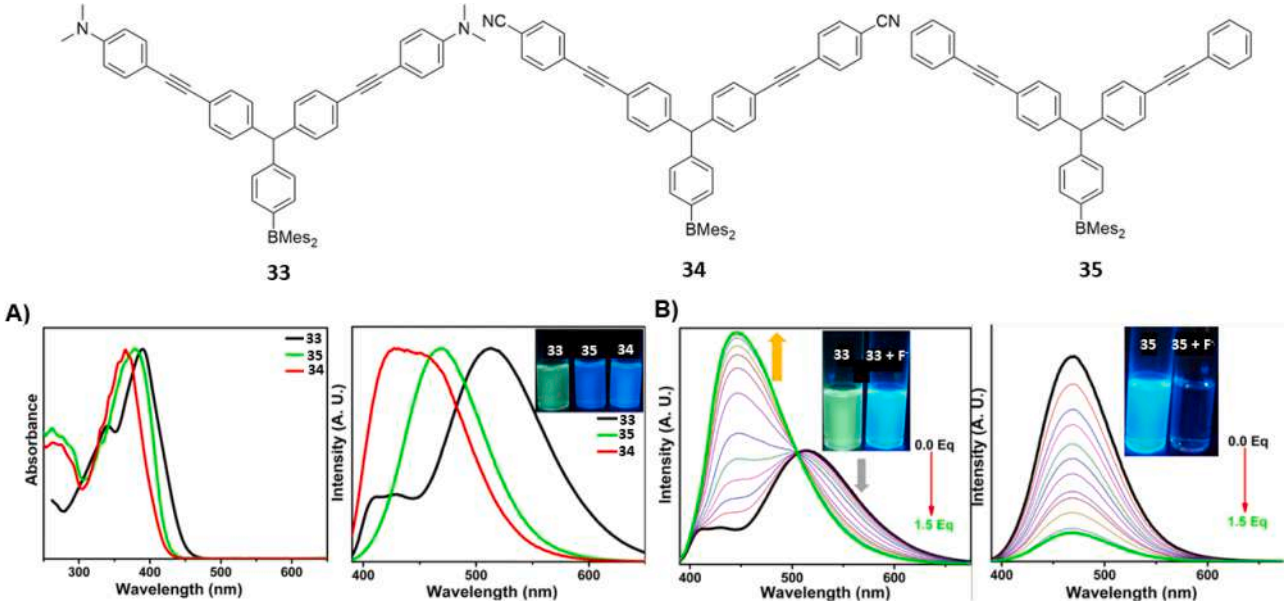

Fig. 15. A) Absorption (left) and emission (right) spectra of **33**–**35** (10 mM) in CH_2Cl_2 (λ_{exc} = 375 nm); B) the fluorescence spectra of **33** (left) and **35** (right) upon addition of increasing concentrations of F^- (0–1.5 equivs., λ_{exc} = 375 nm). Adapted with permission from Ref. [51]. Copyright RSC 2022.

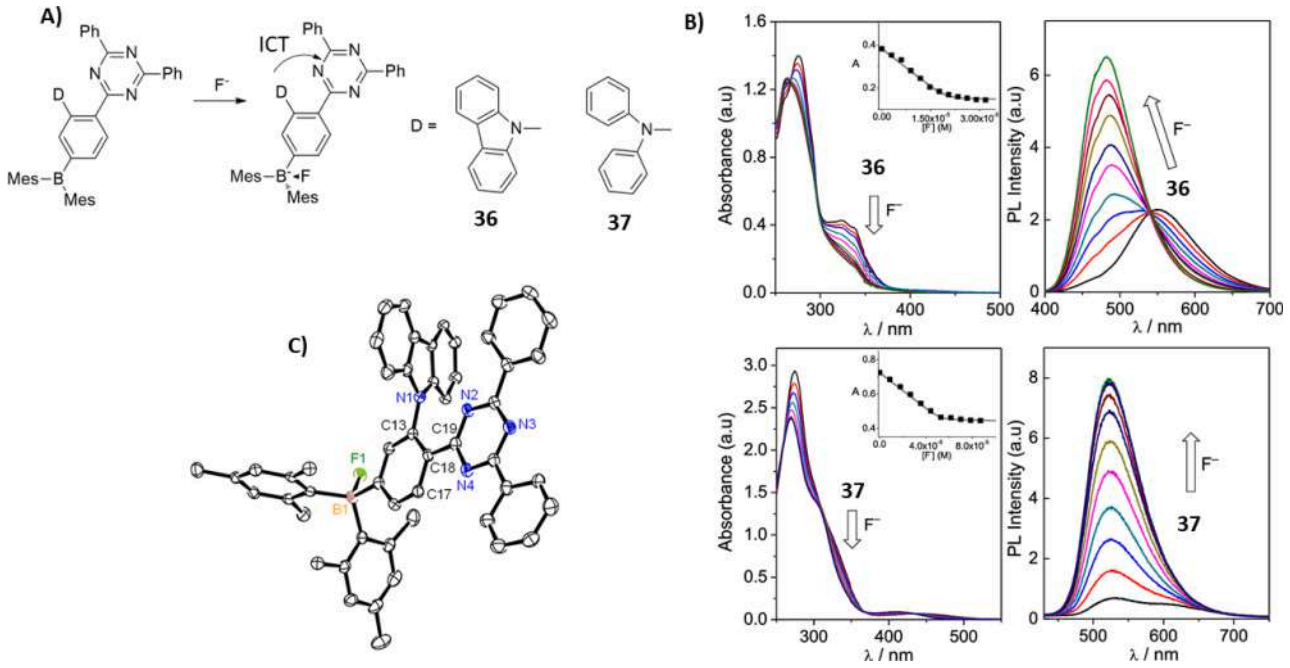

Fig. 16. A) Schematic representation of fluoride sensing by **36**–**37**; B) UV–Vis absorption spectra (left) and fluorescence spectra (right) of (top) **36** (2.0×10^{-5} M, $\lambda_{exc} = 297$ nm) and (bottom) **37** (5.3×10^{-5} M, $\lambda_{exc} = 367$ nm) in THF upon addition of increasing amounts of TBAF (0–2.0 equivs.). (inset) A plot of the absorbance versus [F^-] for **36** (338 nm) and **37** (336 nm); C) the single crystal X-ray structure of **36**·F^- (50 % thermal ellipsoids). The TBA counter cations and hydrogen atoms have been omitted for clarity. Adapted with permission from Ref. [52]. Copyright ACS 2020.

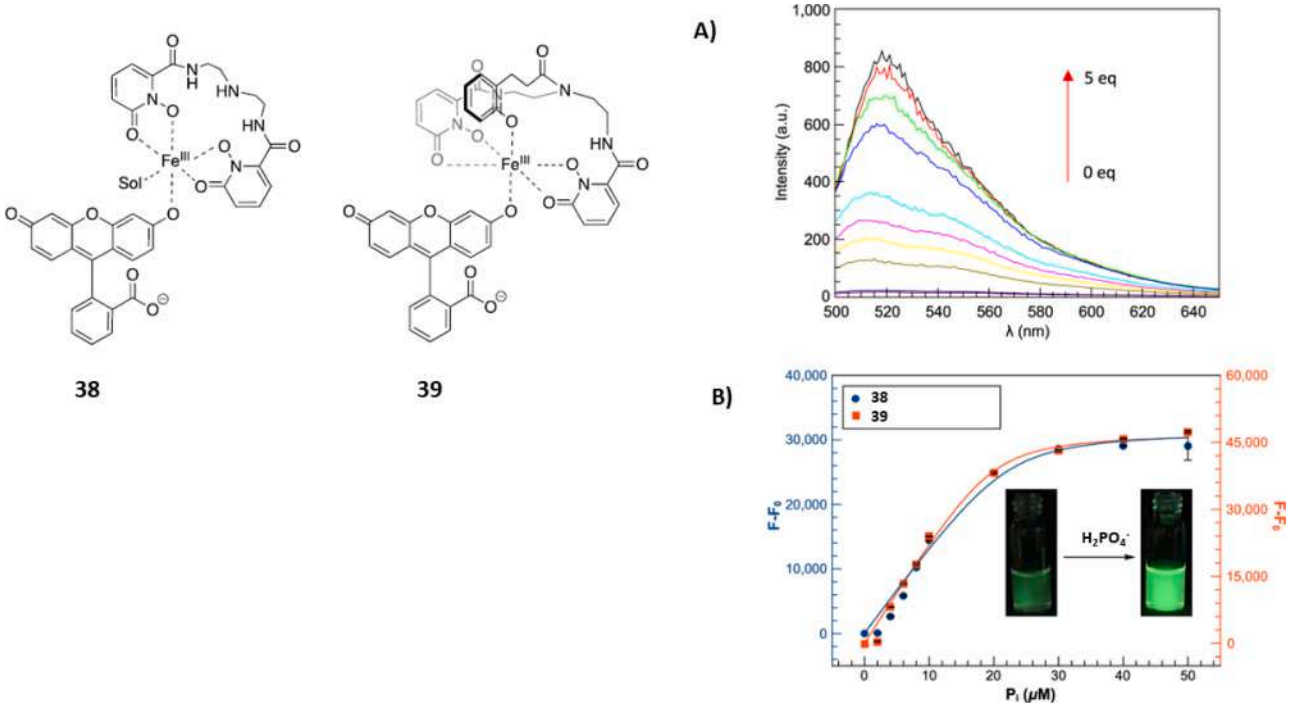

Fig. 17. A) Fluorescence titration of **38** upon increasing amounts of $H_2PO_4^-$ (Pi, 0–5 equivs.); and B) the subsequent increase in the emission intensity of **38** and **39** (10 μM) in wet ethanol at pH = 7. $\lambda_{exc} = 456$ nm, excitation and emission slit widths = 5 nm, voltage = 600 V, and $T = 25$ °C (298 K). F and F_0 represent the fluorescence intensity in the presence and in the absence of anions. Adapted with permission from Ref. [59]. Copyright ACS 2022.

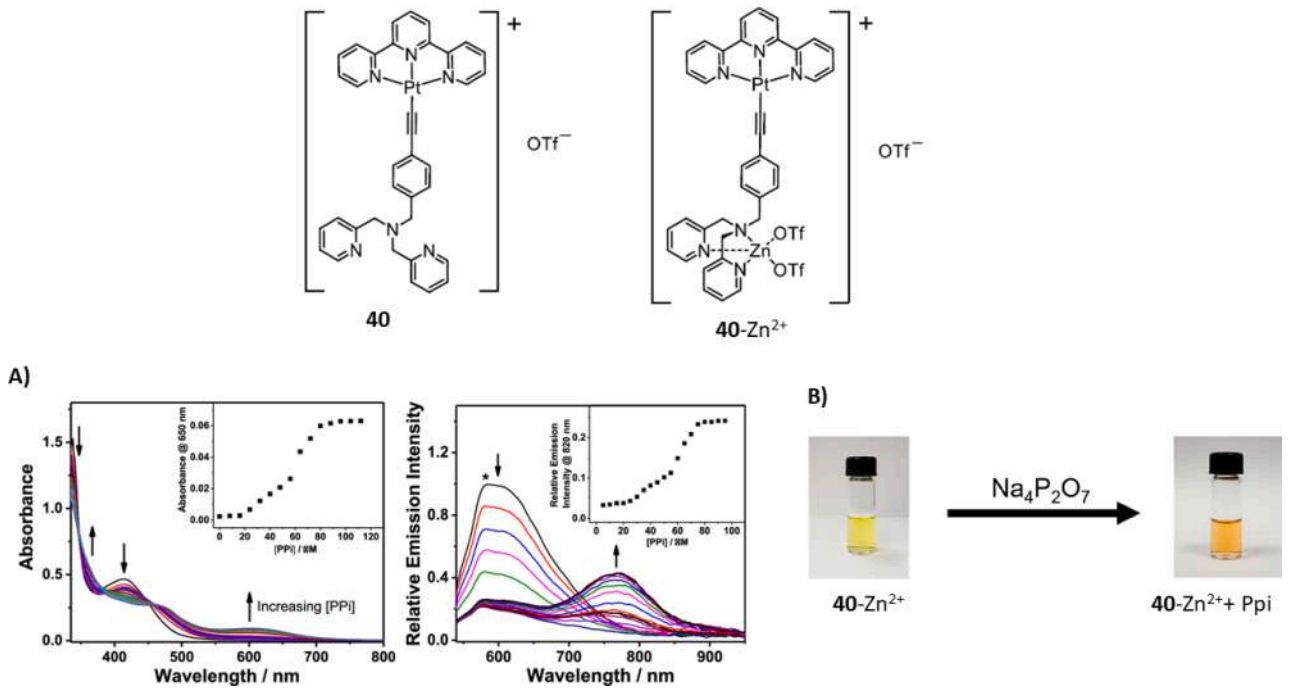

Fig. 18. A) Left: the absorption spectra of **40**·Zn^{2+} upon addition of increasing amounts of $Na_4P_2O_7$ (inset: plots of the absorbance at 650 nm as the function of the concentration of $Na_4P_2O_7$) and right: emission spectra of **40**·Zn^{2+} upon addition of increasing amounts (inset: plots of the emission intensity at 820 nm as the function of the concentration of $Na_4P_2O_7$) both measured at 298 K; B) colour change of the solution after adding 1.1 equivs. of $Na_4P_2O_7$. Adapted with permission form Ref. [60]. Copyright ACS 2021.

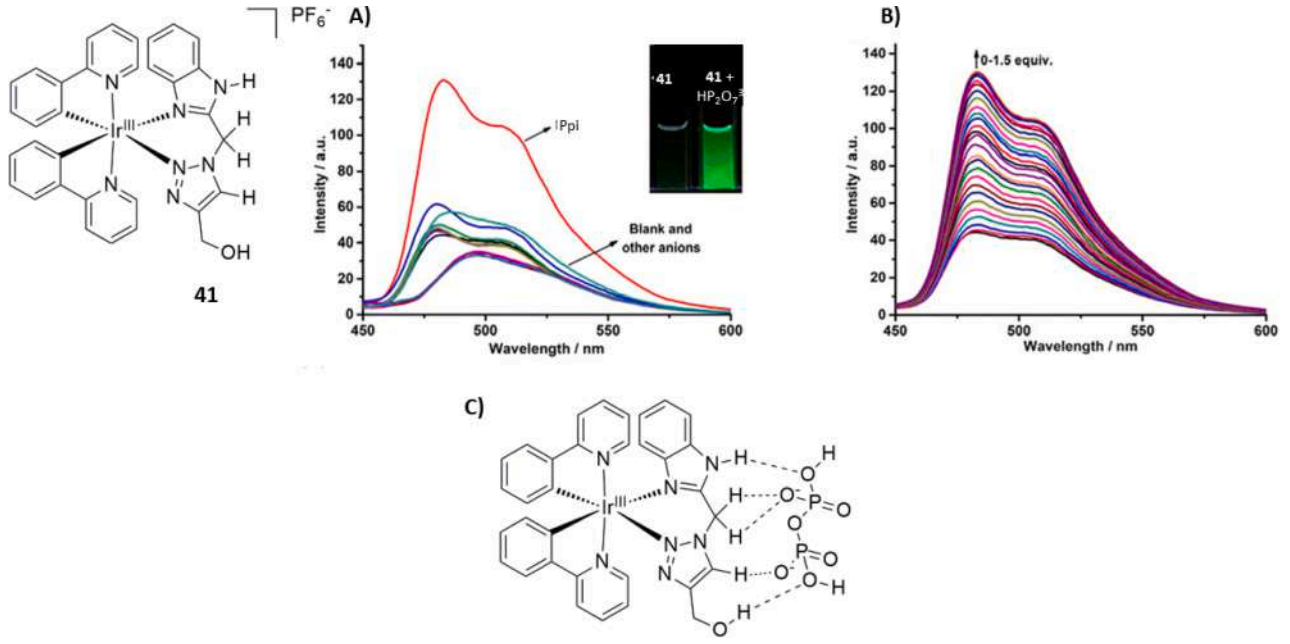

Fig. 19. A) Fluorescence spectra of **41** (10 μM) upon addition of 1.5 equivs. of different anionic species (F^-, Cl^-, Br^-, I^-, HO^-, AcO^-, NO_3^-, HSO_4^-, CN^-, $H_2PO_4^-$, AMP, ADP, and ATP); (Inset) and the fluorescence of **41** (10 μM) under a UV lamp upon addition of $H_2P_2O_7^{2-}$ (15 μM). B) The fluorescence titration of **41** (10 μM) upon addition of 0–1.5 equivs. of $H_2P_2O_7^{2-}$ in CH_3CN (λ_{exc} = 370 nm) at 298 K (25 °C); C) proposed binding mode of $H_2P_2O_7^{2-}$. Adapted with permission from Ref. [61]. Copyright RSC 2022.

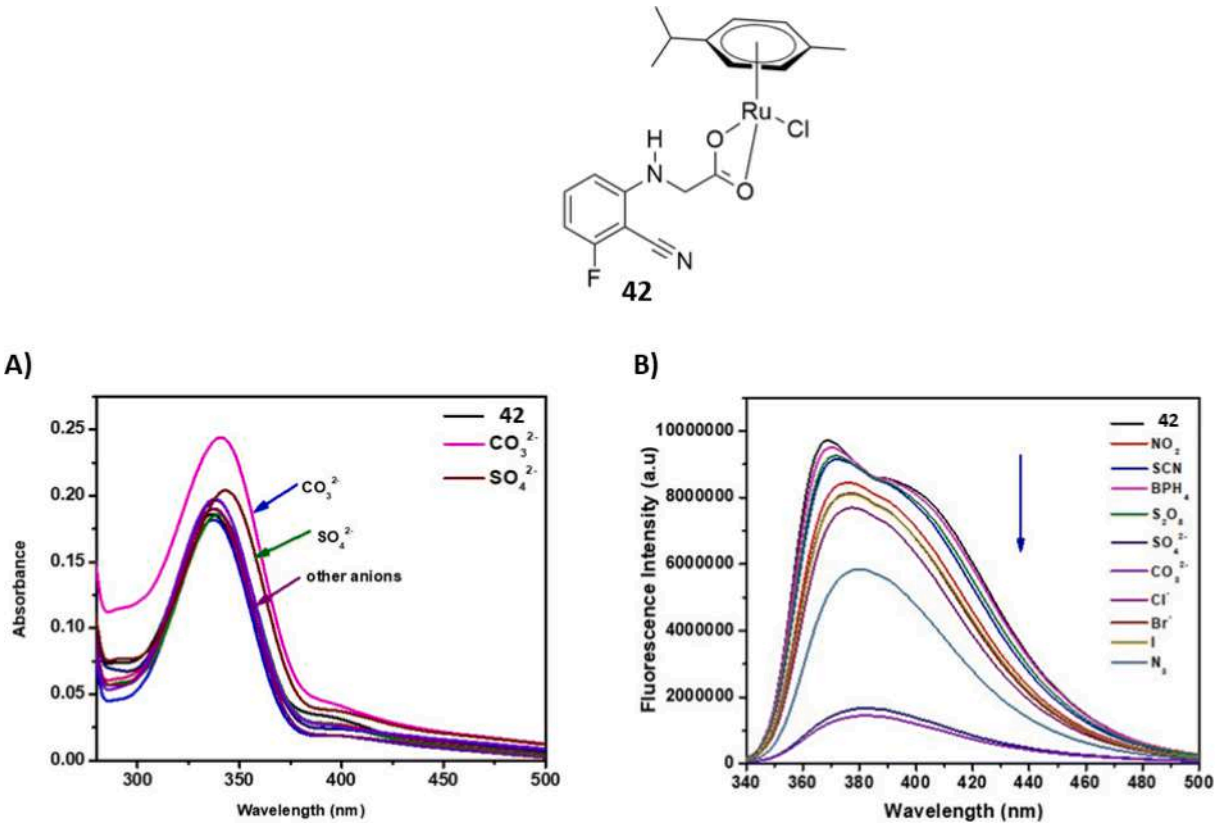

Fig. 20. A) The UV–Vis spectra of **42** (4×10^{-5} M) in DMSO upon the addition of 10 μL of different anionic species (10 mM); B) fluorescence spectra of **42** (4×10^{-5} M) upon the addition of 1.5 equivs. of different anionic species (4×10^{-4} M) in DMSO. Adapted with permission from Ref. [67]. Copyright RSC 2022.

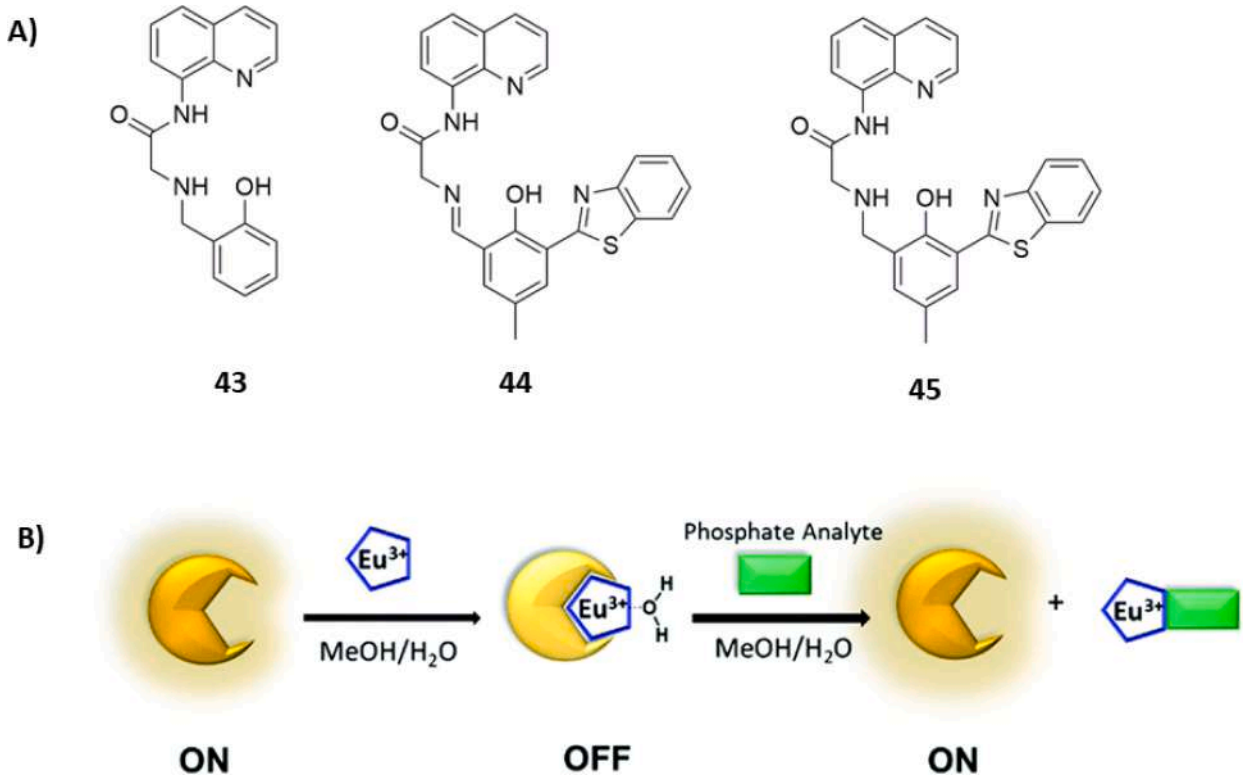

Fig. 21. Proposed mechanism of detection for the Eu(III) complexes of **43**–**45**. Adapted with permission from Ref. [74]. Copyright RSC 2022.

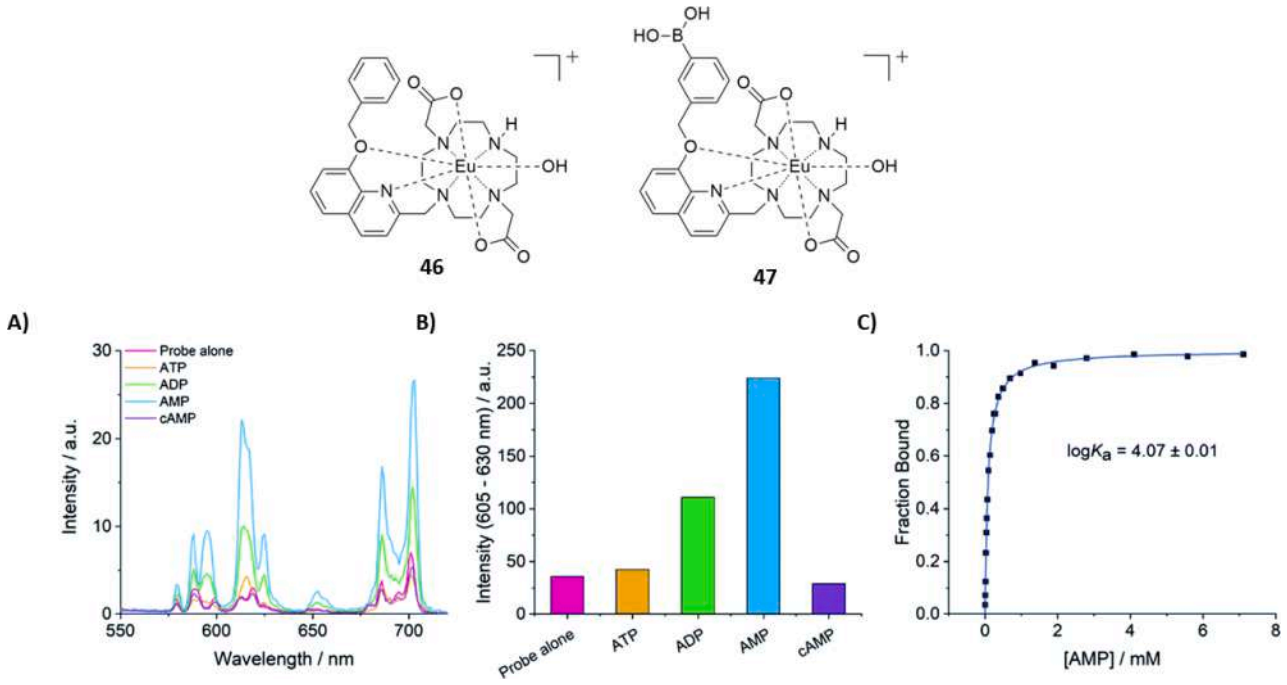

Fig. 22. A) The emission enhancement of **47** (5 mM) in the presence of AMP, ATP, ADP, and cAMP (1 mM); B) Emission spectra intensity of the ΔJ = 2 emission band of **47** (5 mM) in the presence of AMP ATP, ADP, and cAMP (1 mM); C) plot of fraction bound (obtained from the ΔJ = 2 / ΔJ = 1 intensity ratio) as the function of the AMP concentration, showing the fit to a 1:1 binding isotherm (HEPES at pH 7.0 (10 mM) and 295 K, λ_{exc} = 322 nm). Reproduced with permission from Ref. [75]. Copyright RSC 2022.

98·Cu^{2+} complex leads to a reduction of the absorption band at 400 nm, with the concomitant formation of the band at 493 nm, as highlighted by the purple line absorption spectrum reported in Fig. 45A, whereas the enhancement of the emission band at 570 nm with a blue shift at 532 nm was observed. On the other hand, the addition of an increasing amount of Cu(II) ion to the **98**·F^- adduct causes the drop of the absorption maximum at 513 nm (see line blue in Fig. 45A) and the enhancement of the emission peak intensity at 532 nm (see line blue in Fig. 45B). This intriguing behaviour was then transferred to a logic circuit interpreting different logic operations, such as XOR, INHIBIT, IMP, and AND logic gates operations. As shown in the truth table reported in Fig. 45C, by using the presence of F^- and Cu(II) as inputs and the change in the absorbance at 400 nm and 440 nm for INH_1 and XOR operations, respectively, and the change in the emission at 513 nm and 532 nm for INH_2, IMP, and AND operations, the author was able to construct the molecular logic circuit reported in Fig. 44C.

A cadmium probe based on quinoline derivative **99** for the identification of F^- by fluorescence was reported by Kumar and co-workers (Fig. 45) [132]. The probe formed a 1:1 adduct in the presence of an increasing amount of fluoride species (as tetrabutylammonium salt), followed by deprotonation upon the addition of an excess of the anion (2 equivs.), as suggested by the ^{1}H NMR studies conducted in DMSO-d_6. Moreover, the authors built a Boolean logic gate through the molecular response to the presence of the F^- in the system. They proposed an AND circuit by using the presence of the fluoride and the UV light as inputs (values of 1 and 0 in the truth table, respectively) and the strong fluorescent emission band centred at 500 nm along with the loss of the emission intensity as output, indicated as ON and OFF mode in the molecular logic circuit (Fig. 46).

Zhang and co-workers reported the sensing properties of a composite MOF probe **100** (Fig. 47) [133]. The probe was found to express a dramatic enhancement of the characteristic emission band centred at 435 nm upon the addition of an increasing amount of F^- (as its TBA salt), with no significant changes on the weaker emission band at 543 nm (Fig. 47A). Furthermore, this response was visible to the naked eye, with the colour of the solution of the composite probe turning from green to purple upon the addition of the fluoride (inset of Fig. 47A). Furthermore, the addition of the $Cr_2O_7^{2-}$ caused the quenching of both the emission bands at 435 nm and 543 nm (see Fig. 46B). Moreover, both the presence or addition of other interfering compounds or species did not affect the sensitivity of the composite probe towards these two species (Fig. 47C).

Importantly, to the best of the authors' knowledge, the MOF composite probe was found to be the best MOF-based chemosensor for the detection of the F^- and $Cr_2O_7^{2-}$ reported in the literature to date (LOD of 34.7 and 22.3 μM for F^- and $Cr_2O_7^{2-}$, respectively). The authors decided to test the optical response of the composite probe in labelling the two species tested in sweat latent fingerprint, in evaluating its monitoring capabilities in the environment, and as a biosensor in HepG2 cell line.

Nevertheless, the authors decided to use that optical response in the construction of a molecular logic gate based on AND–OR operations. As shown in the truth table in Fig. 48B, the presence of the fluoride and the dichromate species in the system were defined as input A and B in the AND operations, whereas the optical response of the MOF composite probe was defined as output C. At the same time, C was defined as one of the inputs of the OR operations, along with the presence of the fluoride species (A). In this second operation, the output of the circuit is defined as A + AB, in which the enhancement of the emission at 435 nm is set as state 1, while its quenching is state 0 (Fig. 48C).

Sivaraman, Rajesh, and co-workers proposed a dual sensing probe **101** for fluoride and bisulphate in aqueous media [134].

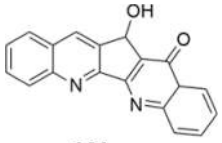

101

Solution-state studies conducted in a mixture of DMSO/H_2O (7:3, *v*/*v*) evidenced the decrease of the characteristic absorption band centred at 347 nm, with the concomitant formation of a new absorption band at 418 nm in the presence of an increasing amount of F^-, which was slowly

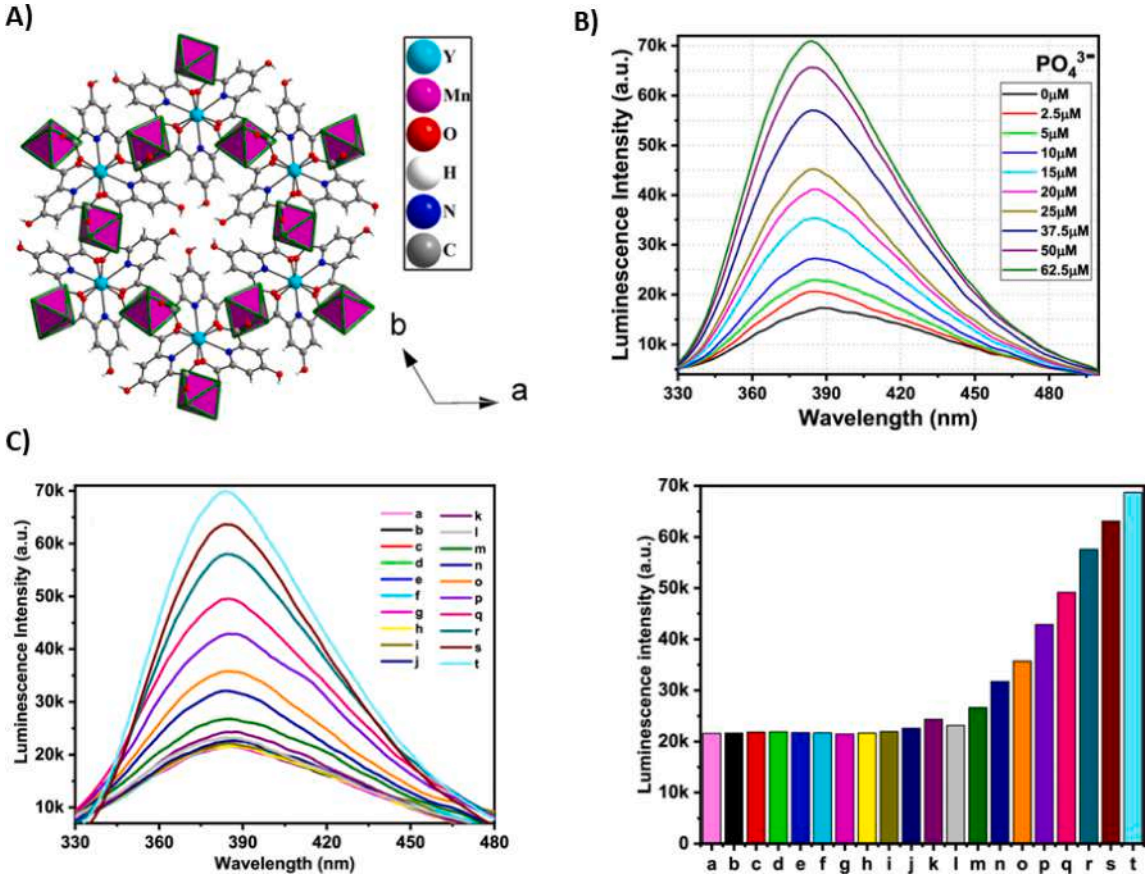

Fig. 23. A) The single crystal X-ray structure of **57** viewed along the c unit cell vector; B) fluorescence spectra of **57** in aqueous solution in the presence of increasing amounts of PO_4^{3-}; C) left: the emission spectra of an aqueous dispersions of **57** upon the gradual addition of a PO_4^{3-} solution in the presence of 12.5 μM of I^-, Cl^-, F^-, Br^-, NO_3^-, NO_2^-, SO_4^{2-}, $C_2O_4^{2-}$, ClO_4^-, and CH_3COO^- ($\lambda_{exc} = 280$ nm), and C) right: the corresponding emission intensity ($\lambda_{em} = 388$ nm). Experiments a–t correspond to the following conditions: (a) an aqueous dispersion of **57**, (b) a + 12.5 μM F^-, (c) b + 12.5 μM Cl^-, (d) c + 12.5 μM Br^-, (e) d + 12.5 μM I^-, (f) e + 12.5 μM $C_2O_4^{2-}$, (g) f + 12.5 μM SO_4^{2-}, (h) g + 12.5 μM NO_3^-, (i) h + 12.5 μM NO_2^-, (j) i + 12.5 μM CH_3COO^-, (k) j + 12.5 μM ClO_4^-, (l) k + 2.5 μM PO_4^{3-}, (m) l + 5 μM PO_4^{3-}, (n) m + 10 μM PO_4^{3-}, (o) n + 15 μM PO_4^{3-}, (p) o + 20 μM PO_4^{3-}, (q) p + 25 μM PO_4^{3-}, (r) q + 37.5 μM PO_4^{3-}, (s) r + 50 μM PO_4^{3-}, and (t) s + 62.5 μM PO_4^{3-}. Reproduced with permission from Ref. [87]. Copyright ACS 2022.

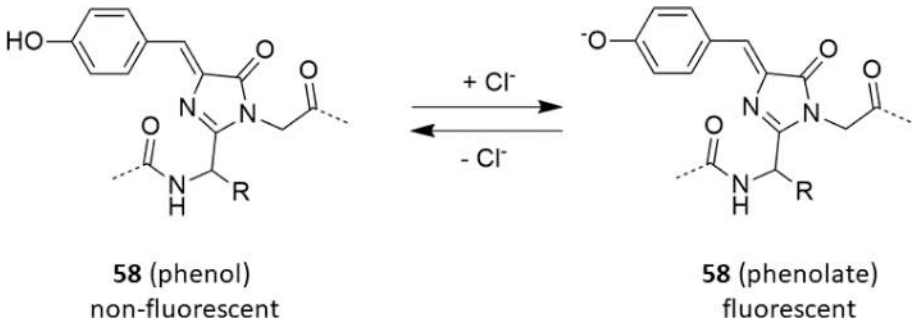

Fig. 24. The chemical structure of **58** (left) and the deprotonated phenolate form (right), which is a charged Cl^- turn-on fluorescent probe developed in ref.[88].

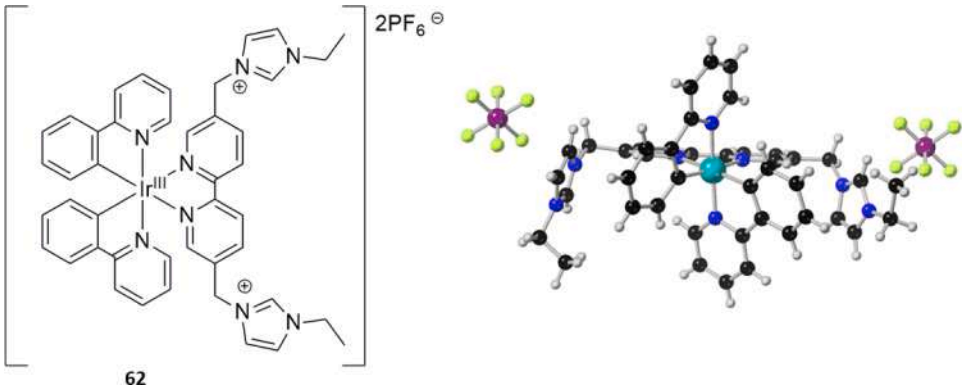

Fig. 25. The chemical structure of **62** and the corresponding solid-state structure were obtained using single-crystal X-ray diffraction. Solvent molecules and surrounding PF_6^- ions were removed for clarity; hydrogen, carbon, nitrogen, fluorine, phosphorus, and iridium atoms are shown as grey, black, blue, lime-green, purple, and cyan, respectively.

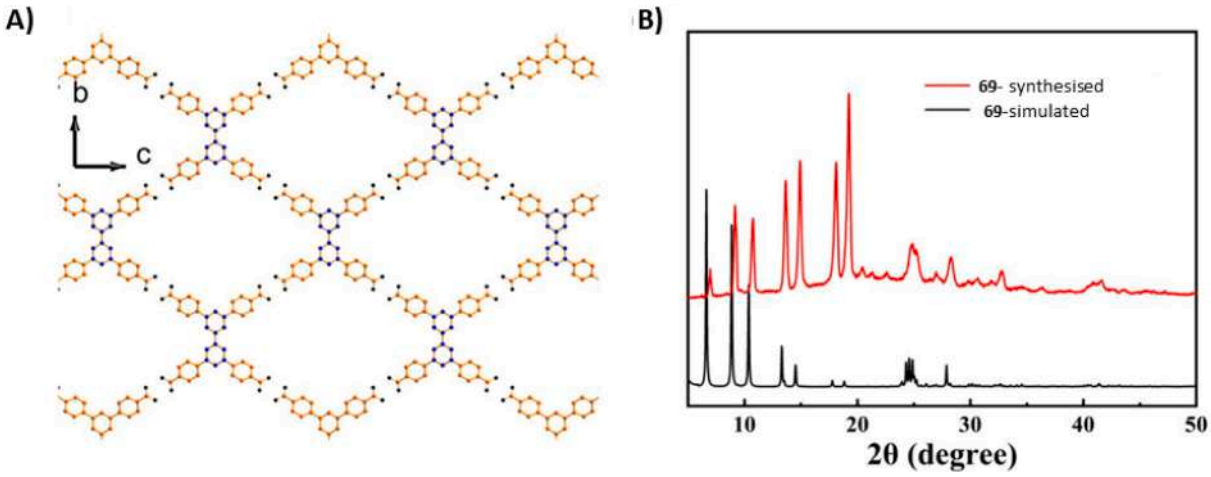

Fig. 26. A) The structure of HOF **69**; B) the PXRD patterns of **69** as synthesised in red and simulated data in black. Adapted with permission from Ref. [94]. Copyright MDPI 2022.

shifted as a consequence of the deprotonation of the –OH group of the probe and an intramolecular charge transfer (Fig. 49A). Moreover, when excited at 390 nm, **101** displays a weak emission band centred at 564 nm, which was dramatically enhanced upon the addition of the increasing amount of F^- (Fig. 49B), with a strong enhancement of the quantum yield of the probe from 0.03 in its free form to 0.38 in the presence of the anion.

Curiously, the addition of an increasing amount of HSO_4^- to the adduct **101**·F^- caused the quenching of the emission band at 564 nm, with the disappearance of the absorption band at 418 nm and the restore of the absorption band at 347 nm characteristic of the free probe (Fig. 50A–B for the UV–Vis and fluorescence spectra, respectively).

This OFF-ON-OFF behaviour was then transferred into a molecular logic gate circuit based on AND, NOT, NAND, and NOR operations. The

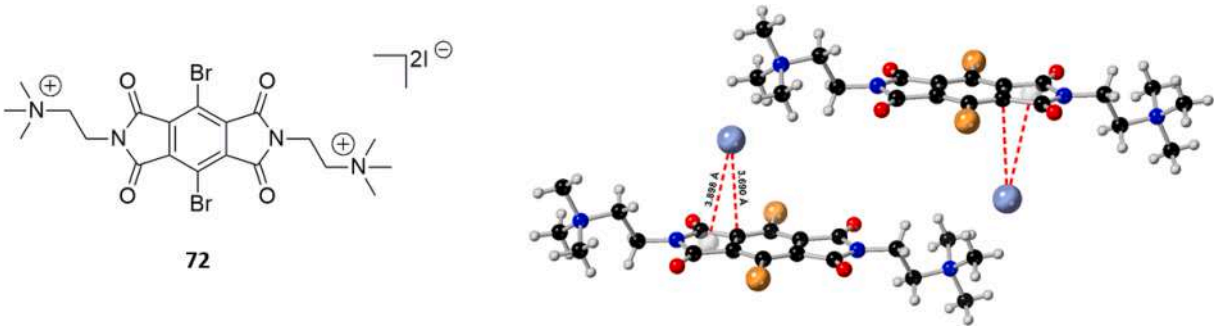

Fig. 27. The chemical structure of **72** and single crystal X-ray structure of **72** with anion–π interactions are shown as red broken bonds. Hydrogen atoms are shown in grey, carbon in black, nitrogen in blue, oxygen in red, iodine in pale-blue, bromine in orange, and placed centroid atoms are shown as transparent grey atoms. All solvent molecules have been removed for clarity.

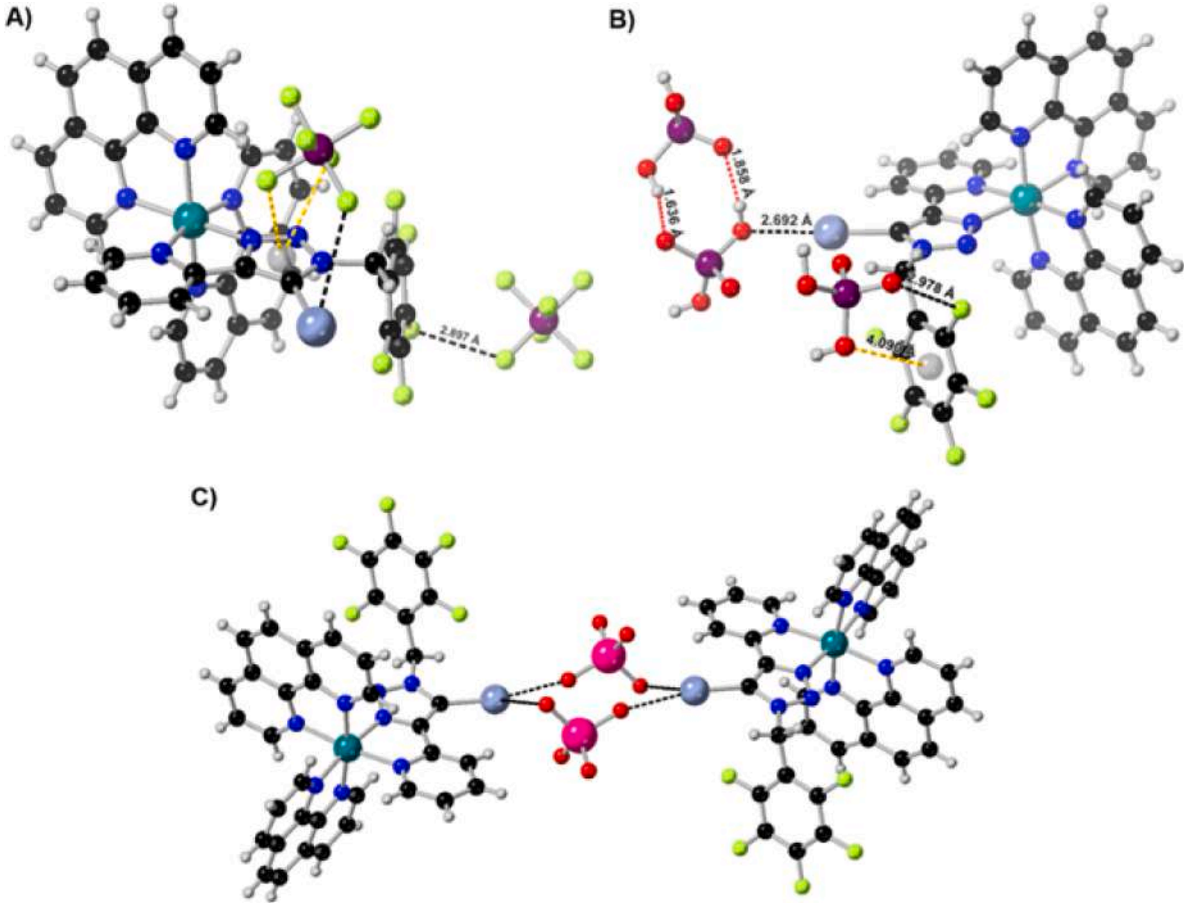

Fig. 28. The single crystal X-ray structure of A) **73**•$[PF_6]_2$, B) **73**•$[H_2PO_4]_2$, and C) **73**•$[ReO_4]_2$. Halogen-bonding interactions, anion–π interactions, and anti-electrostatic anion–anion interactions are shown as broken black, yellow, and red broken bonds, respectively. Hydrogen atoms are shown in grey, carbon in black, nitrogen in blue, oxygen in red, fluorine in lime-green, iodine in light-blue, phosphorus in purple, ruthenium in teal, rhenium in pink, and placed centroid atoms are shown as transparent grey atoms. All solvent molecules, counterions, and other anions have been removed for clarity.

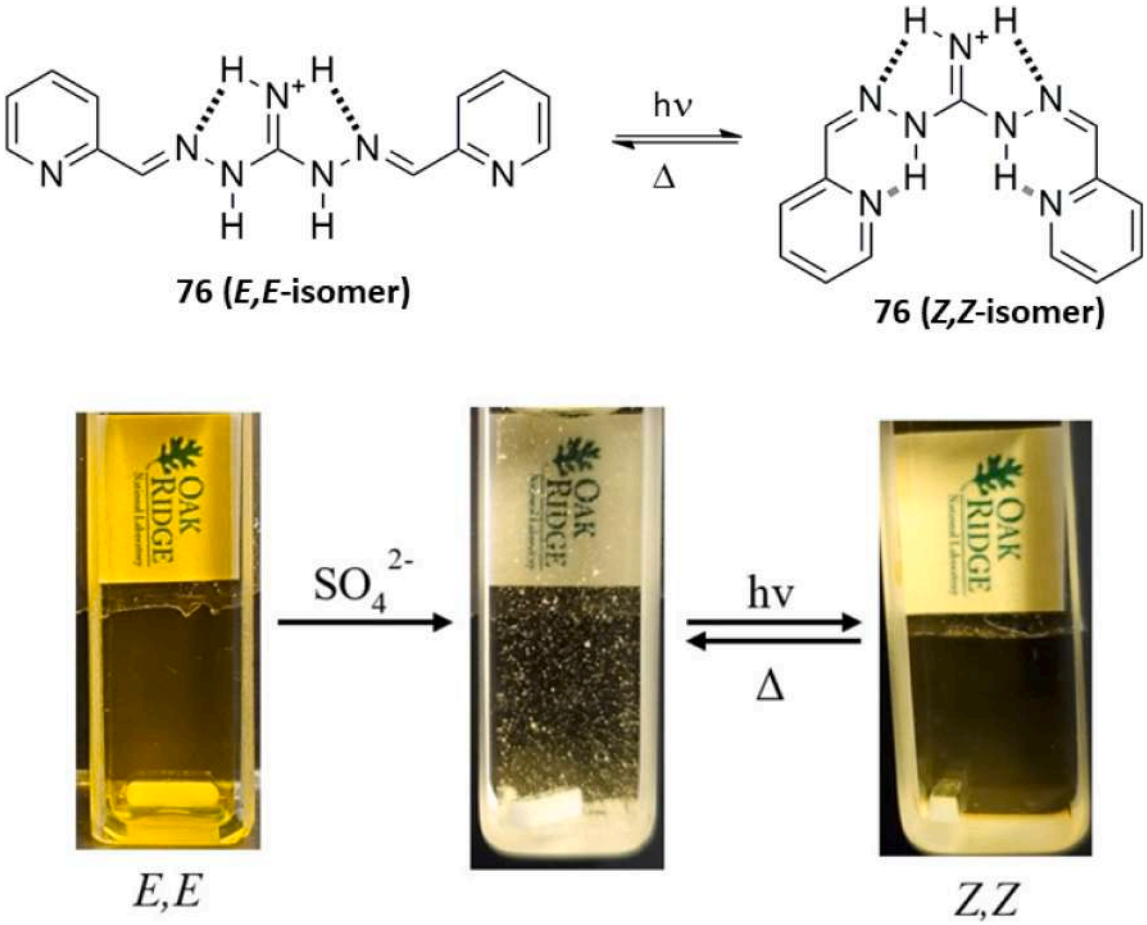

Fig. 29. Conversion of receptor **76** from *E,E*-isomer to *Z,Z*-isomer and photo-induced SO_4^{2-} precipitation-dissolution process. Reproduced with permission from Ref. [105]. Copyright Wiley 2022.

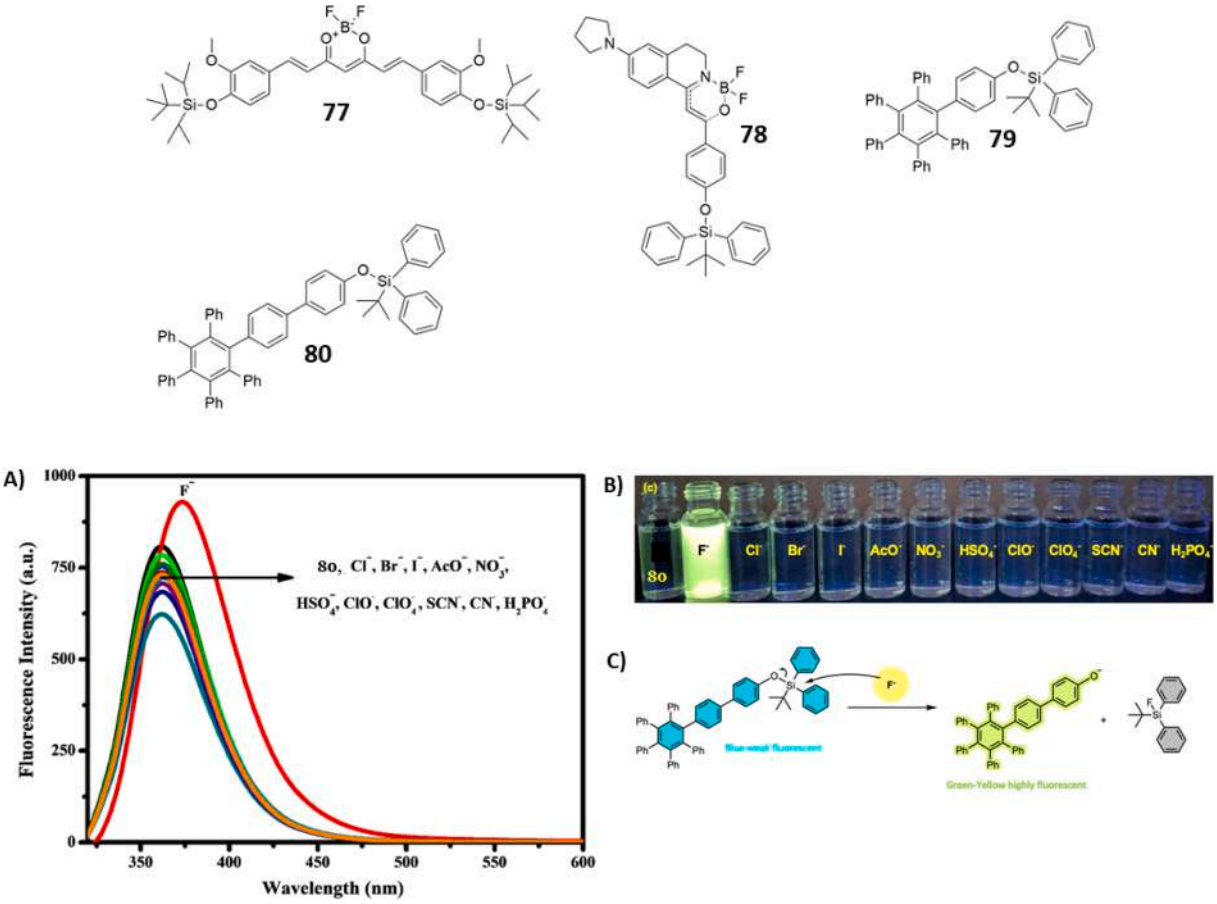

Fig. 30. A) Changes in the fluorescence spectra of **80** in the presence of various anions in THF; B) Changes in the fluorescence emission of **80** under UV light; C) proposed sensing mechanism. Adapted with permission from Ref. [106]. Copyright RSC 2022.

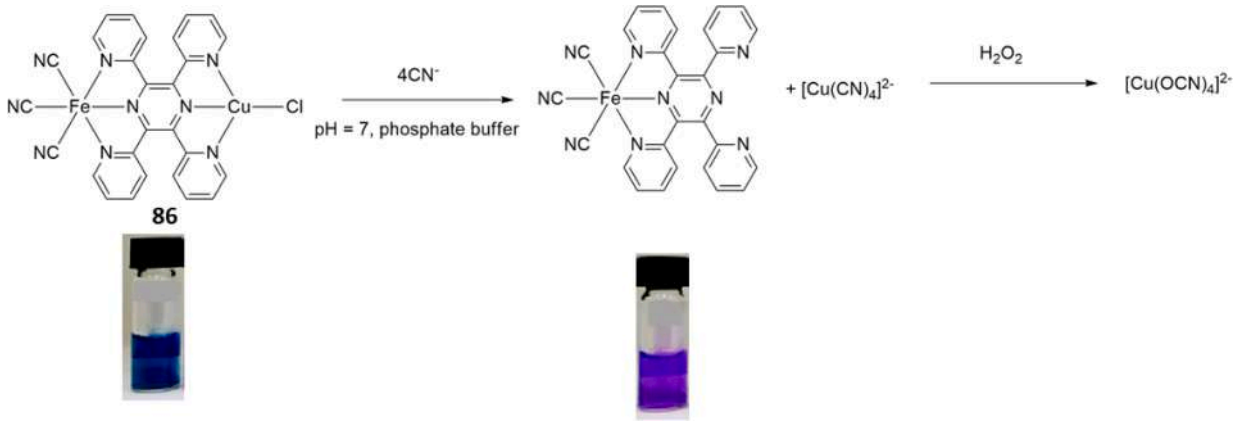

Fig. 31. The proposed mechanism for the sensing and the catalytic degradation of CN^- to OCN^- by complex **86**. Adapted from Ref. [114].

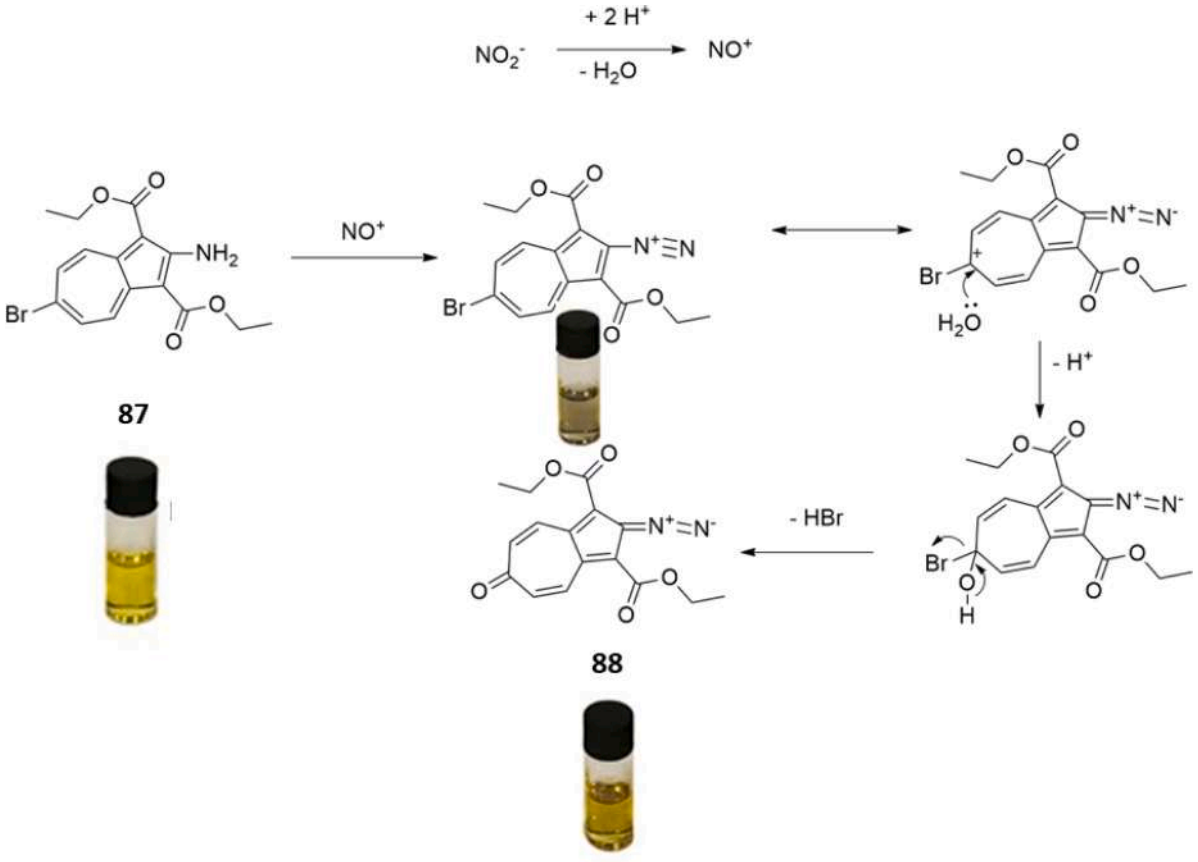

Fig. 32. Proposed mechanism for nitrite sensing by **87**. Adapted from ref.[115].

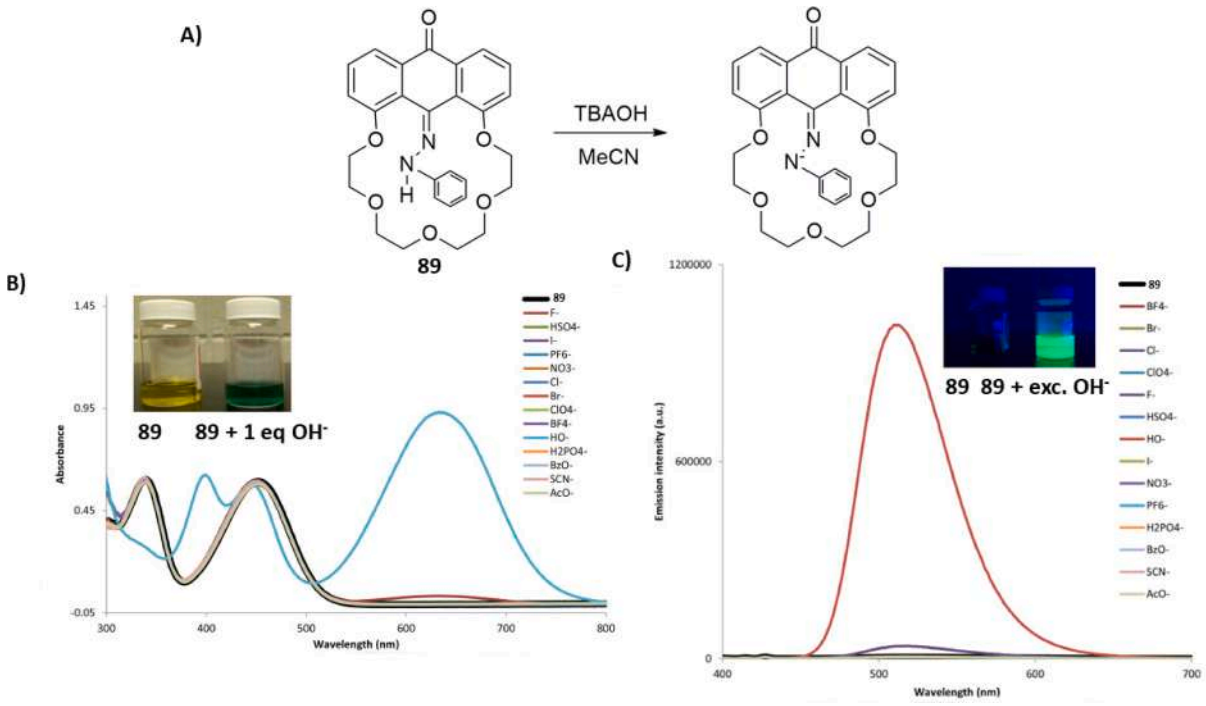

Fig. 33. A) Proposed mechanism for hydroxide sensing by **89**; B) changes in the absorption spectrum of **89** upon addition of one equivalent of different anions in CH_3CN solution; C) changes in the emission spectrum of **89** upon addition of an excess of different anions in CH_3CN solution. Adapted from Ref. [116].

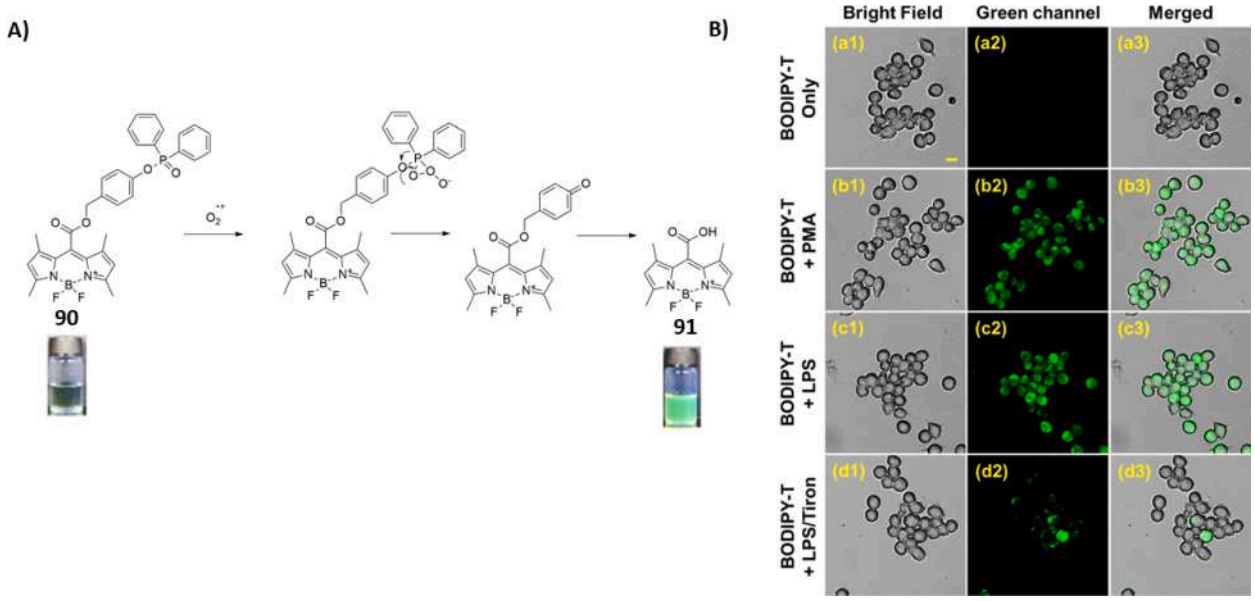

Fig. 34. A) Proposed mechanism for superoxide sensing by **90**; B) Confocal fluorescence images of RAW264.7 cells treated with different procedures: (a1–a3) RAW264.7 cells incubated with **90** for 20 min at 37 °C; (310.15 K) (b1–b3) RAW264.7 cells pretreated with PMA, then incubated with **90**; (c1–c3) RAW264.7 cells pretreated with LPS, then incubated with **90**; (d1–d3) RAW264.7 cells pre-treated with LPS, then treated with Trion, then incubated with **90**. Green channel: 515–580 nm (λ_{exc} = 488 nm). Scale bar = 10 μm. Reproduced with permission from Ref. [117]. Copyright Elsevier 2022.

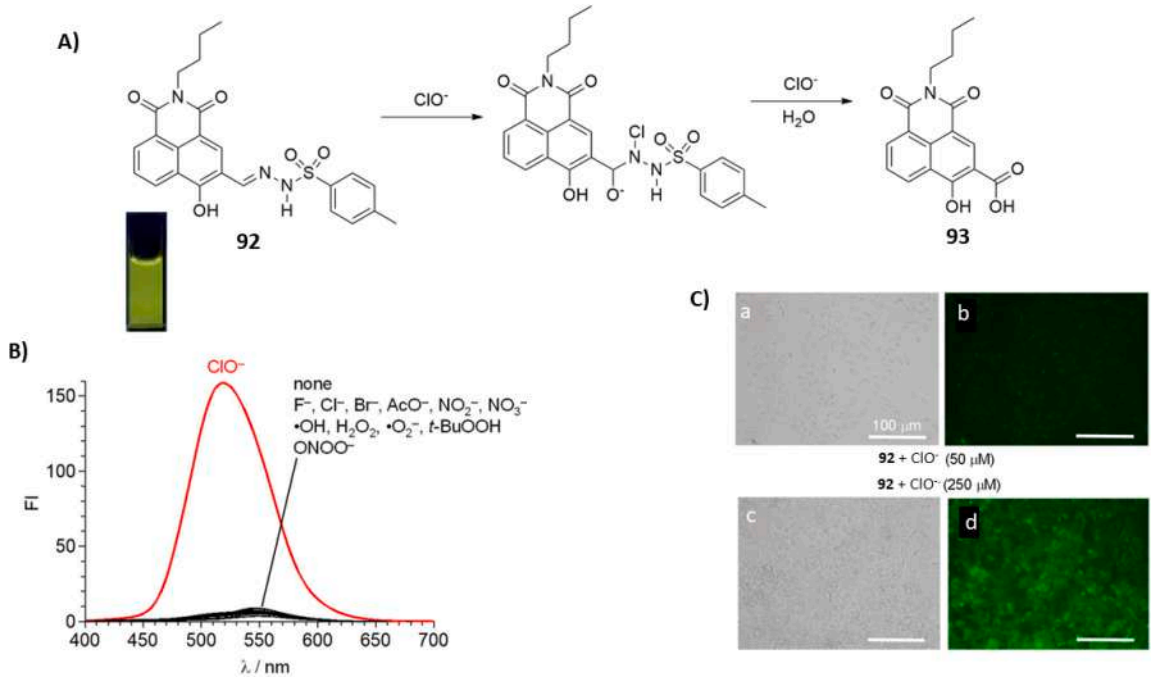

Fig. 35. A) Proposed mechanism for hypochlorite sensing by **92**; B) Changes in the emission spectra of **92** upon addition of different anions in H_2O/CH_3CN (8:2, *v/v*) at neutral pH; C) fluorescence images of HeLa cells treated with **92** in the presence of different concentrations of ClO^-. Adapted with permission from Ref. [118]. Copyright MDPI 2020.

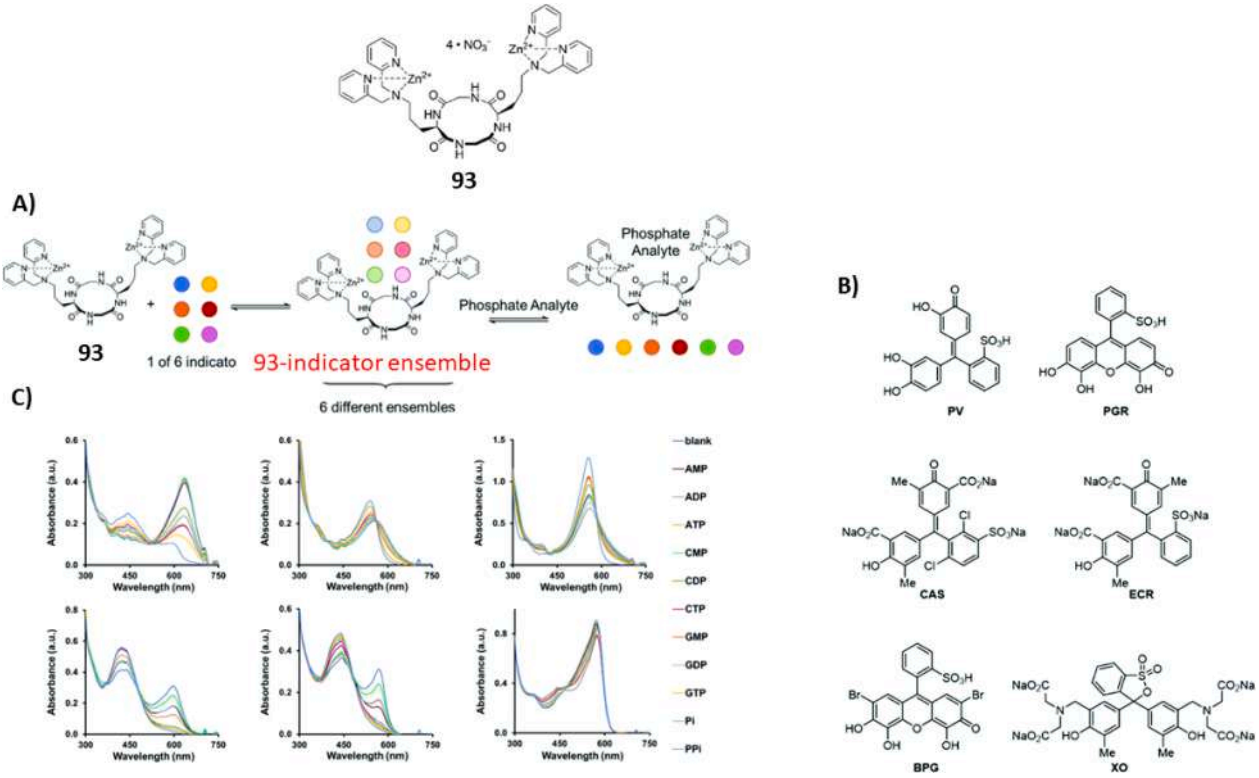

Fig. 36. A) Schematic representation of the sensor array based on different 1:1 **93**·indicator complexes and indicator displacement assay (IDA); B) the molecular structure of the indicators: pyrocatechol violet (PV), pyrogallol red (PGR), chromeazurol S (CAS), eriochrome cyanine R (ECR), bromopyrogallol red (BPG), and xylenol orange (XO); C) the absorbance spectra of different **93**·indicator ensembles. Reproduced with permission from Ref. [127]. Copyright RSC 2022.

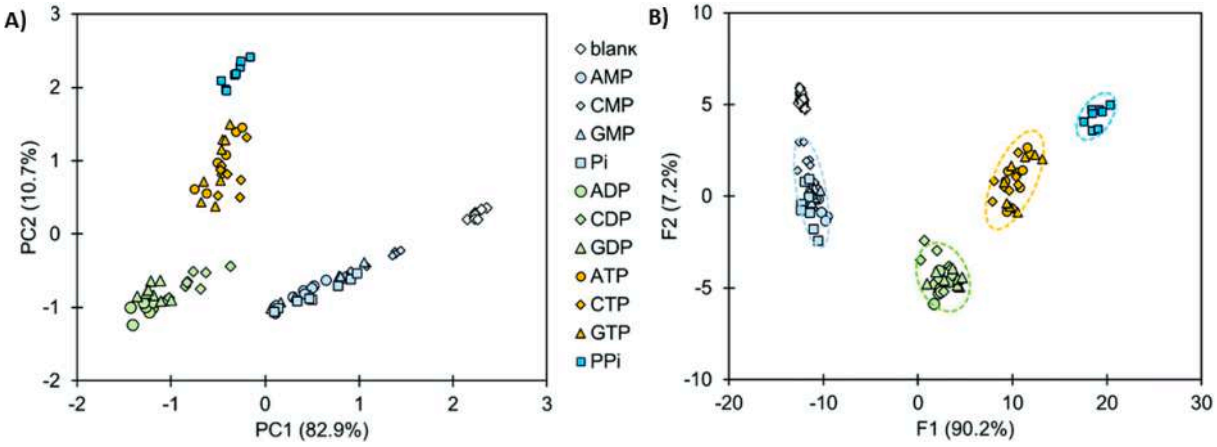

Fig. 37. The array response of **93**·indicator complexes evaluated by principal component analysis (PCA) and linear discriminant analysis (LDA): A) two-dimensional PCA plot; B) two-dimensional LDA score plot, showing mono- (light blue), di- (green), and tri-phosphates (yellow), $HP_2O_7^{3-}$ (turquoise), and the blank (empty). The 95 % confidence ellipsoids for clusters are indicated as colored ellipsoids (representing the blank, mono-, di-, triphosphates, and PPi, respectively). Reproduced with permission from ref.[127]. Copyright RSC 2022.

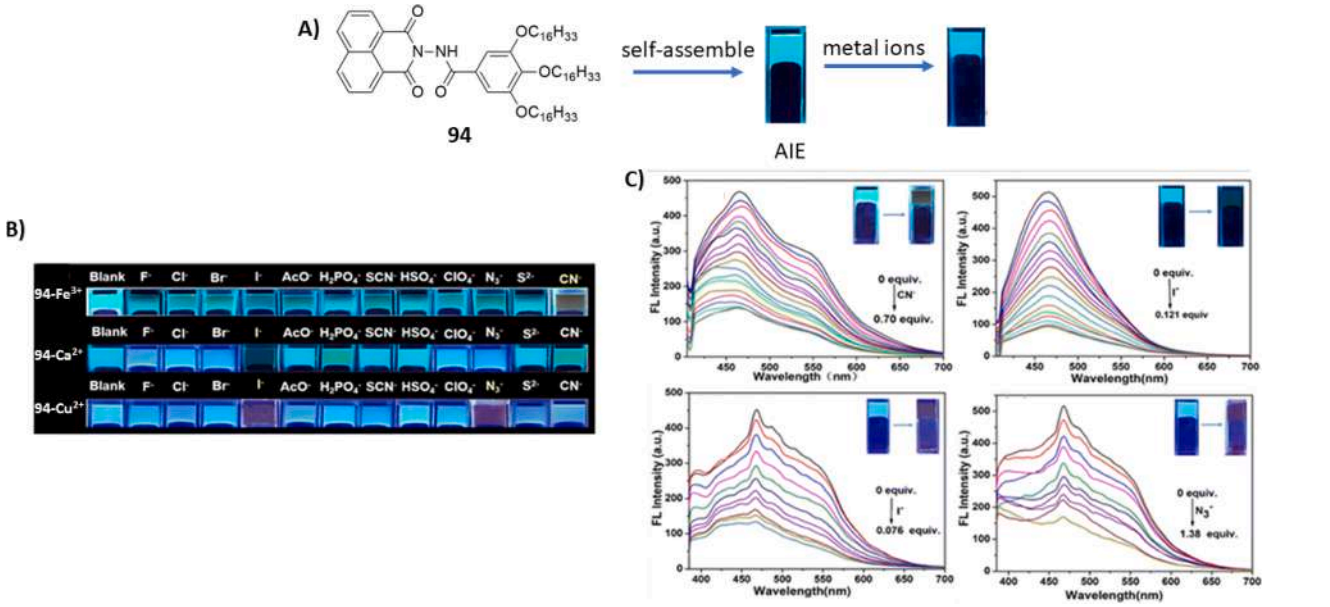

Fig. 38. A) Formation of the fluorescent supramolecular gel and metallogels based on gelator **94**; B) Photographs of the fluorescence response of **94**·Fe^{3+}, **94**·Ca^{2+}, and **94**·Cu^{2+} metallogels for anions; C) fluorescence titration of **94**·Fe^{3+} for CN^- (top left), **94**·Ca^{2+} for I^- (top right), **94**·Cu^{2+} for I^- (bottom left) and **94**·Cu^{2+} for N_3^- (bottom right). Adapted with permission from Ref. [128]. Copyright RSC 2022.

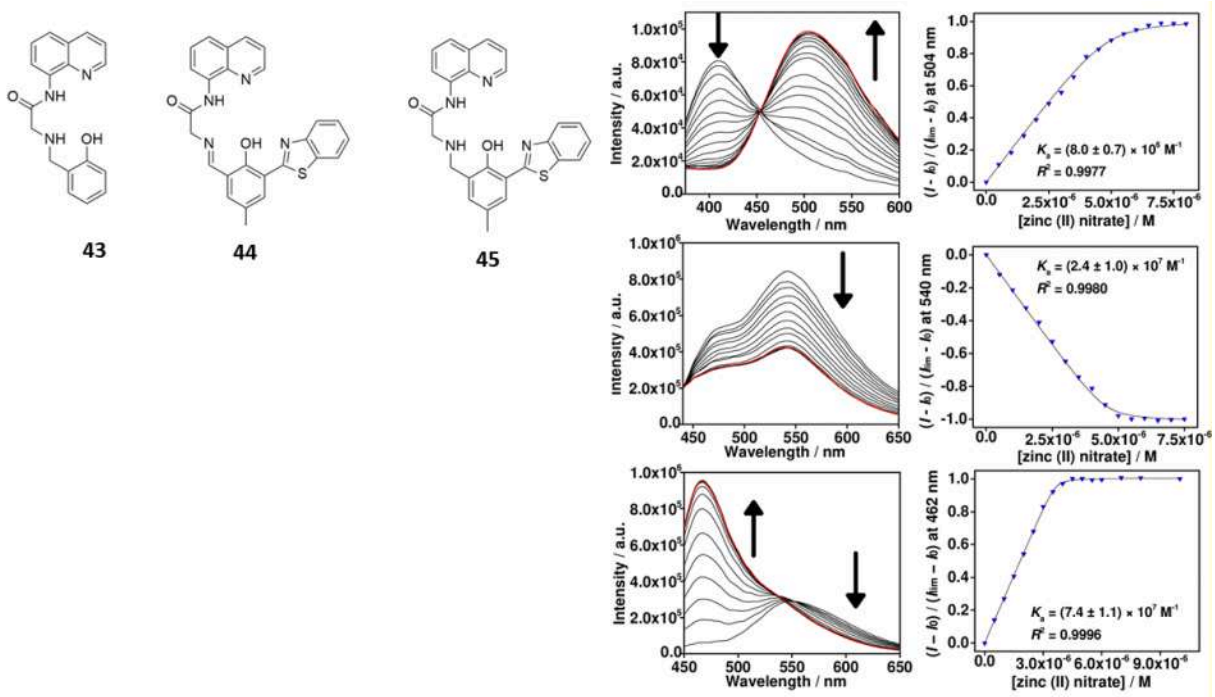

Fig. 39. Fluorescence spectra titrations of 5.0 μM solutions of **43** (top), **44** (middle) and **45** (bottom) upon addition of Zn(II) (λ_{exc} = 330, 345, and 345 nm, respectively). Medium: HEPS buffer solutions (10 mM, pH 7) and CH_3CN (50 %, *v/v*). Reproduced with permission from Ref. [129]. Copyright Wiley 2021.

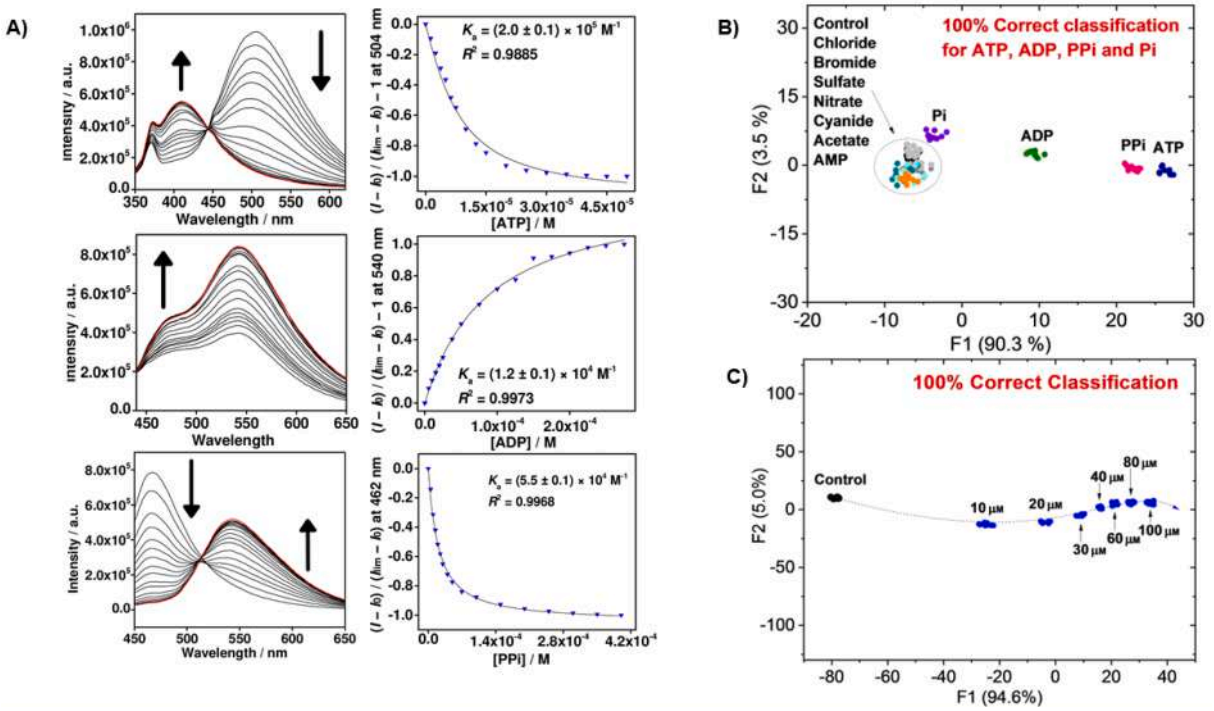

Fig. 40. A) Fluorescence spectra titrations of Zn(II)·**43** (top), Zn(II)·**44** (middle), and Zn(II)·**45** (bottom) upon addition of ATP (λ_{exc} = 330 nm, 345 nm and 435 nm respectively). For each solution, [43–45] and [Zn(II)] are 5.0 μM; B) LDA obtained from the response pattern of Zn(II)·**43**, Zn(II)·**44** and Zn(II)·**45** to the different anions (11 in total) in HEPES buffer solution (pH 7, 10 mM) containing CH_3CN (50 %, *v/v*); C) LDA obtained from the response pattern of the Zn(II)·**43**, Zn(II)·**44**, and Zn(II)·**45** at different concentration of ATP ([ATP] = 0, 10, 20, 30, 40, 60, 80, and 100 μM). Each clustering was identified with 100 % correct classification. Medium: HEPES buffer (pH 7, 10 mM) and acetonitrile (50 %, *v/v*). Reproduced with permission from Ref. [129]. Copyright Wiley 2021.

resulting molecular logic gates are reported in Fig. 51A. From the truth table, it is possible to notice that the presence of the F^- and the HSO_4^- was used as the two inputs. In contrast, the absorption band at 418 nm (spectrophotometric response) and the emission band at 564 nm (spectrofluorimetric response) were used as output points of the circuit. Moreover, it is worth noticing how both the detection capability of **101** towards F^- and its OFF-ON-OFF behaviour can be restored without losing performance over more than 12 cycles (Fig. 51B).

Srinivasan, Thomas, and co-workers explored the potential application of the tautomeric isomer of a diaryldipyrromethane derivative **102**

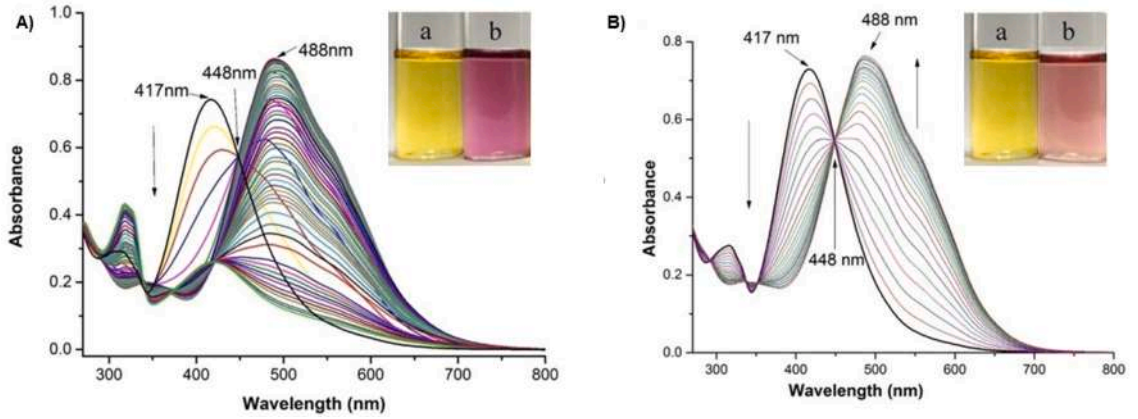

Fig. 41. The UV–Vis titration of **95** in DMSO in the presence of increasing amounts of A) F^- and B) AcO^-. Inset: colour change of the solution of **95** in DMSO in the presence of 2 equivs. of A) F^- and B) AcO^-. Reproduced with permission from Ref. [130]. Copyright Wiley 2020.

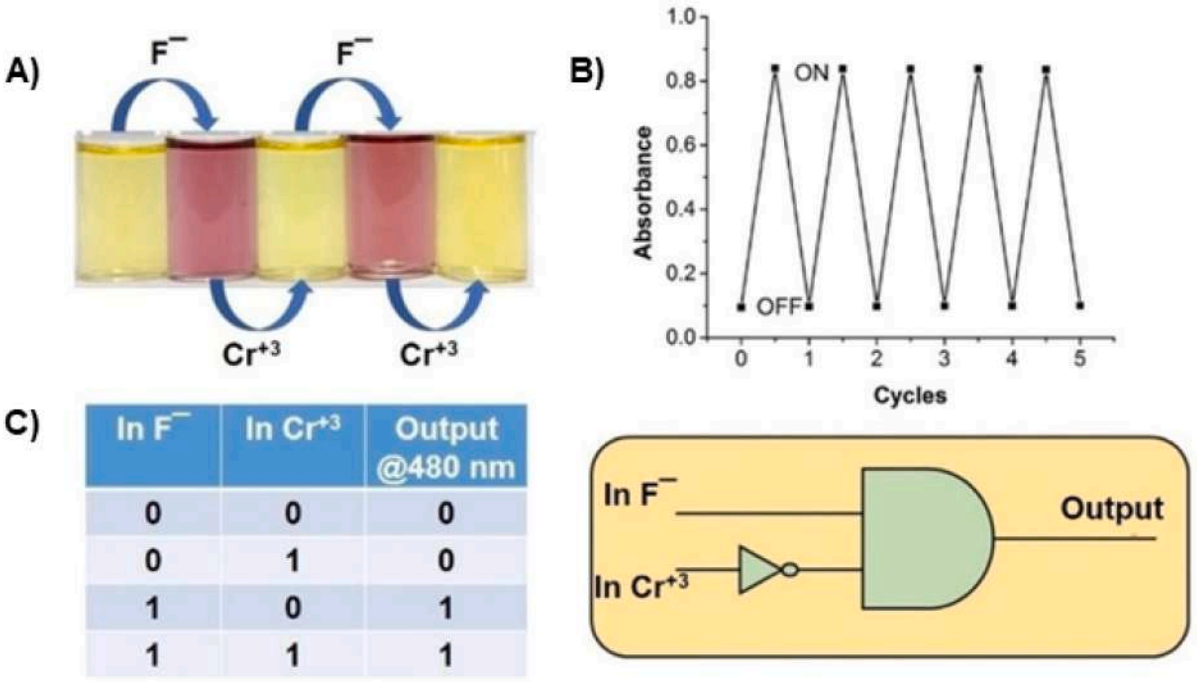

In F^-	In Cr^{+3}	Output @480 nm
0	0	0
0	1	0
1	0	1
1	1	1

Fig. 42. A) The colorimetric response of **95** in DMSO upon the alternating addition of F^- and Cr^{3+} with B) reversible OFF-ON-OFF behaviour; C) truth table of the OFF-ON-OFF molecular logic gate of **95**. Reproduced with permission from Ref. [130]. Copyright Wiley 2020.

[135]. By irradiating a solution of **102** in CH_3CN under the UV lamp, the formation of the excited state intramolecular proton transfer tautomeric product $\mathbf{102}_{EE}$ was observed in a 1:1 ratio with the non-excited form $\mathbf{102}_{KK}$ (see scheme reported in Fig. 52). The mixture of the two isomers was tested in the presence of a set of anions by spectrophotometric and spectrofluorimetric techniques. Interestingly, the addition of an increasing amount of F^- caused the reduction of the characteristic band centred at 390 nm with the concomitant formation of a new absorption band at 528 nm and a bathochromic shift of the band at 283 nm to 303. On the other hand, the fluorescent emission pattern underwent the decrease of the emission band at 560 (λ_{exc} = 356 nm) and concomitant formation of a new red-shifted band at 645 nm, accompanied by a colour change of the solution from bright green to red (Fig. 52B). Moreover, further addition of F^- to the solution caused the diminution of the absorption bands at 350 nm and 528 nm till the disappearance, with the formation of a new absorption band at 421 nm (Fig. 52A). Further, the hypsochromic shift from 624 nm to 574 nm (λ_{exc} = 356 nm) was observed, with a colour change of the solution turning from purple to yellow along with the emission colour turning from red to yellow.

This behaviour was assigned to the deprotonation of the NHs of the tautomeric isomer $\mathbf{102}_{KK}$, forming the $\mathbf{102}^{2}_{KK}{}^{-}$, as suggested by the ^1H NMR measurements conducted in CD_3CN in the presence of F^-, in which the upfield shift of the signals attributed to the aromatic CHs. The solution studies were further extended to various anions, such as CN^-, $H_2PO_4^-$, BzO^-, and AcO^-, but only in the case of CN^- was observed the same behavior to that observed in the presence of F^-. Nevertheless, the mixture of the two isomers were also tested in the presence of several cation species in their perchlorate salts. The presence of Zn^{2+} and Cd^{2+}

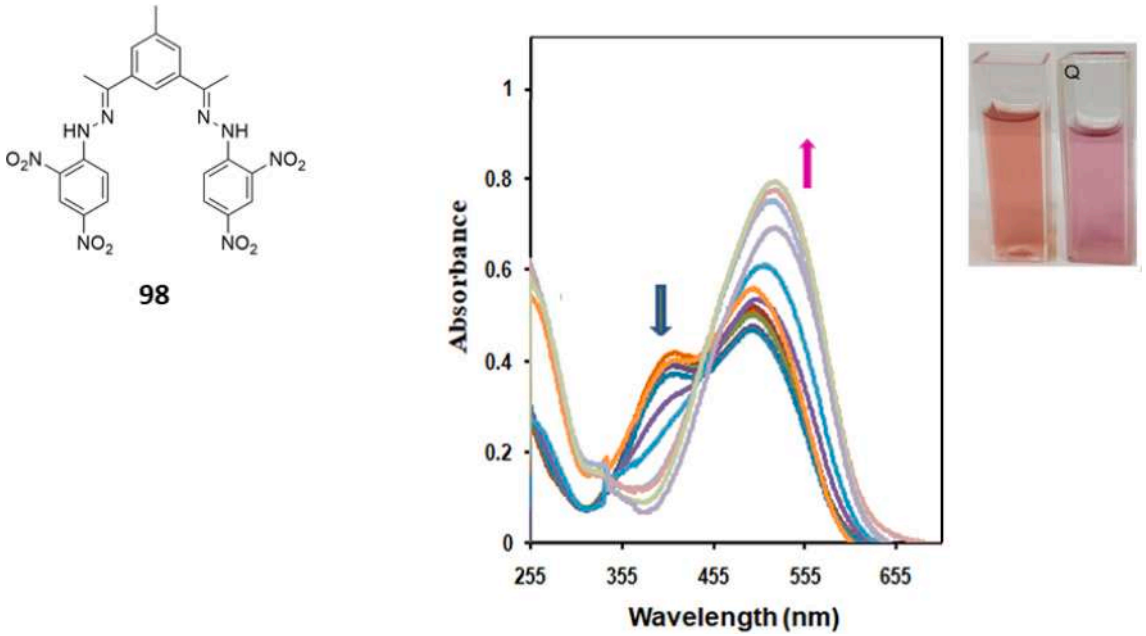

Fig. 43. Chemical structure of **98**; UV–Vis titration of **98** in DMSO in the presence of an increasing amount of F^- (Inset: colour change of the solution of **98** in the presence of 2 equivs. of F^-). Reproduced with permission from Ref. [131]. Coyright Elsevier 2022.

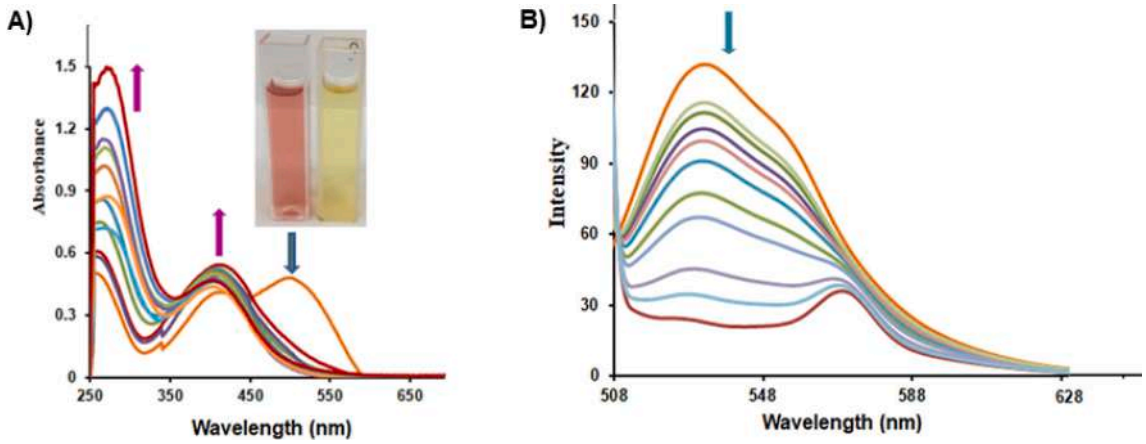

Fig. 44. A) The UV–Vis titration of **98** in DMSO in the presence of increasing amount of Cu(II) (Inset: colour change of the solution of **98** in the presence of 2 equivs. of Cu(II)); spectrofluorimetric titration of **98** in DMSO in the presence of increasing amount of Cu(II). Reproduced with permission from Ref. [131]. Coyright Elsevier 2022.

caused significant changes in the photophysical properties of the $\mathbf{102}^{2}_{\mathbf{KK}}{}^{-}$/$\mathbf{102}^{2}_{\mathbf{EE}}{}^{-}$, whereas the presence of the other cation species tested did not produce any significant change. Particularly, upon the addition of increasing amounts of Zn(II), the partial disappearance of the absorption band at 421 nm was observed, with the concomitant formation of a new absorption band at 417 nm, whereas the emission band at 534 nm underwent a dramatic ipsochromic shift to 444 nm (Fig. 53A-53B for the UV–Vis and fluorescence spectra, respectively).

This experimental evidence was further supported by a colour change of the solution turning to intense yellow to pale yellow. This dual response of the system the $\mathbf{102}^{2}_{\mathbf{KK}}{}^{-}$ and $\mathbf{102}^{2}_{\mathbf{EE}}{}^{-}$ was used to construct a molecular logic gate characterized by the exposure of the probe to the UV light, the presence of both F^- and CN^- as input points, and the presence of the Zn^{2+} as input 1, 2, and 3, respectively, and the emission at 444 nm as a single output. Moreover, the response was further used to build a molecular keypad in which the emission at 444 nm represented to lock off the system. Under these conditions, authors were able to find the password UFZ as the unique input combination to correctly unlock the molecular keypad.

Siva and co-workers described the sensing properties of a rhodamine 3-acetic acid-based **103** (Fig. 54) [136]. The rhodamine-based chemosensor was found to be able to detect CO_3^{2-} species in aqueous solution. The capability of **103** as colorimetric chemosensor towards anions was tested by the naked eye. The addition of the CO_3^{2-} species caused a dramatic colour change of the solution of **103** from yellow to brownish red (ascribable to the deprotonation of the –OH group), whereas no significant changes were observed upon the addition of the other anions tested. Solution studies by UV–Vis spectroscopy in aqueous media were conducted by the authors in order to support the sensitivity towards the CO_3^{2-} species. The addition of the CO_3^{2-} to a solution of **103** caused a dramatic bathochromic shift of the characteristic band centred at 406 nm to 492 nm, accompanied by a weaker shift of the band centred at

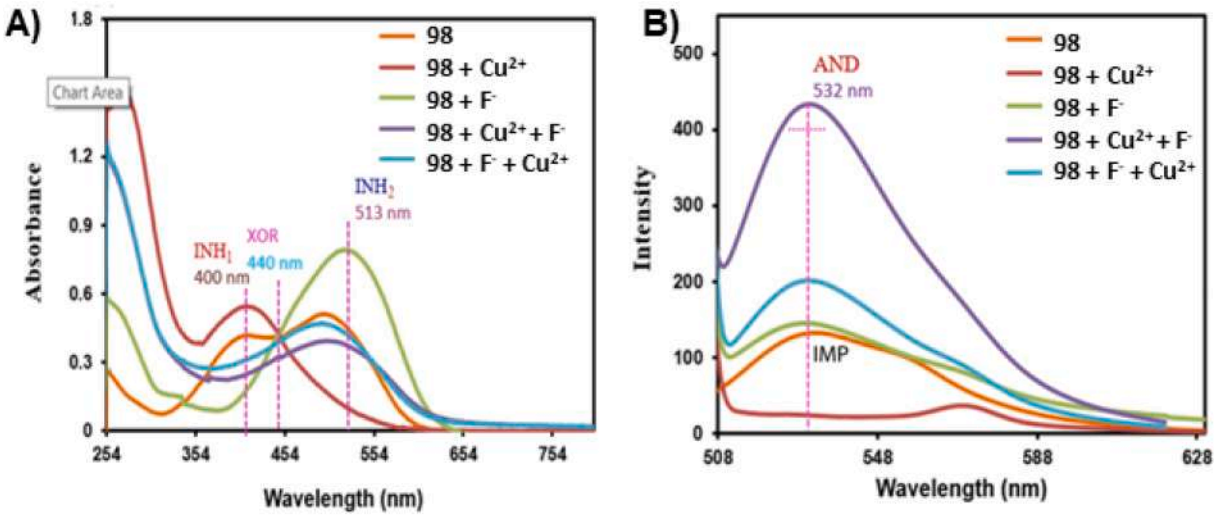

C)

Input		Output				
Input 1	Input 2	Output 1	Output 2	Output 3	Output 4	Output 5
Cu^{2+}	F^-	XOR gate (A 440nm)	INH_1 gate (A 400nm)	INH_2 gate (A 513 nm)	IMP gate (Em 532 nm)	AND gate (Em 532 nm)
0	0	0	0	0	1	0
1	0	1	1	0	0	0
0	1	1	0	1	1	0
1	1	0	0	0	1	1

Fig. 45. A) spectrophotometric and B) spectrofluorimetric response of **98** in the presence of Cu^{2+}, F^-, Cu^{2+} and F^-, and F^- and Cu(II), respectively; C) truth table of the molecular logic gate. Reproduced with permission from Ref. [131]. Copyright Elsevier 2022.

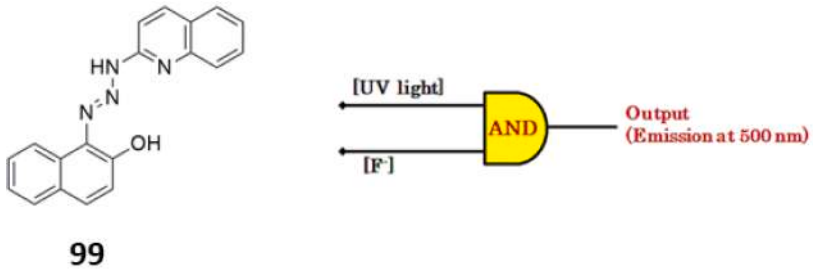

Truth Table

IN1 UV light	IN2 F^-	OUT Emission ON
0	0	0
1	0	0
0	1	0
1	1	1

Fig. 46. Molecular structure of **99**; truth table for the AND molecular logic circuit. Reproduced with permission from Ref. [132]. Copyright Elsevier 2022.

292 nm to 298 nm. Importantly, this experimental analysis showed evidence of the high sensitivity and the fast response of the probe towards the detection of the CO_3^{2-} in an aqueous solution, along with the determination of the LOD (8.1×10^{-5} M).

With these results in mind, the authors proposed a truth table for the construction of molecular logic gates based on an XNOR operation. The absorbance pattern of the rhodamine-based chemosensor in the absence and presence of the CO_3^{2-} species were used as inputs, whereas the response at 492 nm was set as the output. Accordingly, with the operation described above, when the inputs are both set to 0, the output will be 0, whereas it becomes 1 with both conditions of the inputs 0,1 and 1,1.

Marugesapian, Jothi, and co-workers described the reversible OFF-ON-OFF behaviour of the chemosensor **104** in the presence of the Al^{3+} and $HP_2O_7^{3-}$ (Fig. 55) [137]. Spectrofluorimetric studies conducted in DMF:Tris/HCl (6:4, *v/v*) at pH 7.2 highlighted how the addition of an increasing amount of Al^{3+} (as the nitrate salt) caused the enhancement of the emission band centred at 489 nm (λ_{exc} = 390 nm), up to the saturation condition reached in the presence of 1 equiv. of Al^{3+}.

The complex **104**·Al^{3+} was then studied as a sensor for the detection of $HP_2O_7^{3-}$ anions. In particular, the addition of increasing amounts of $HP_2O_7^{3-}$ to a solution of the complex **104**·Al^{3+} caused the partial quenching of the emission at 489 nm, probably due to the sequestration of the metal cation from the $HP_2O_7^{3--}$, followed by a releasing of the free-ligand in solution. The authors decided to transfer this behaviour into an INHIBIT logic operation based on a combination of AND and NOT operations. As shown in the truth table reported in Fig. 56A, the two table is represented by the presence of the Al^{3+} and the $HP_2O_7^{3-}$, whereas the output was set on the emission at 489 nm.

Hens reported the complex of compound **105** (Fig. 57) with Zn(II) with a 1:2 stoichiometry [138]. Particularly, the authors described the sensing properties of the binuclear complex of **105** in the presence of different anion species. Fluorescence screening in a mixture of CH_3OH/H_2O (3:2, *v/v*) in HEPES buffer at pH 7.2 was conducted in the presence

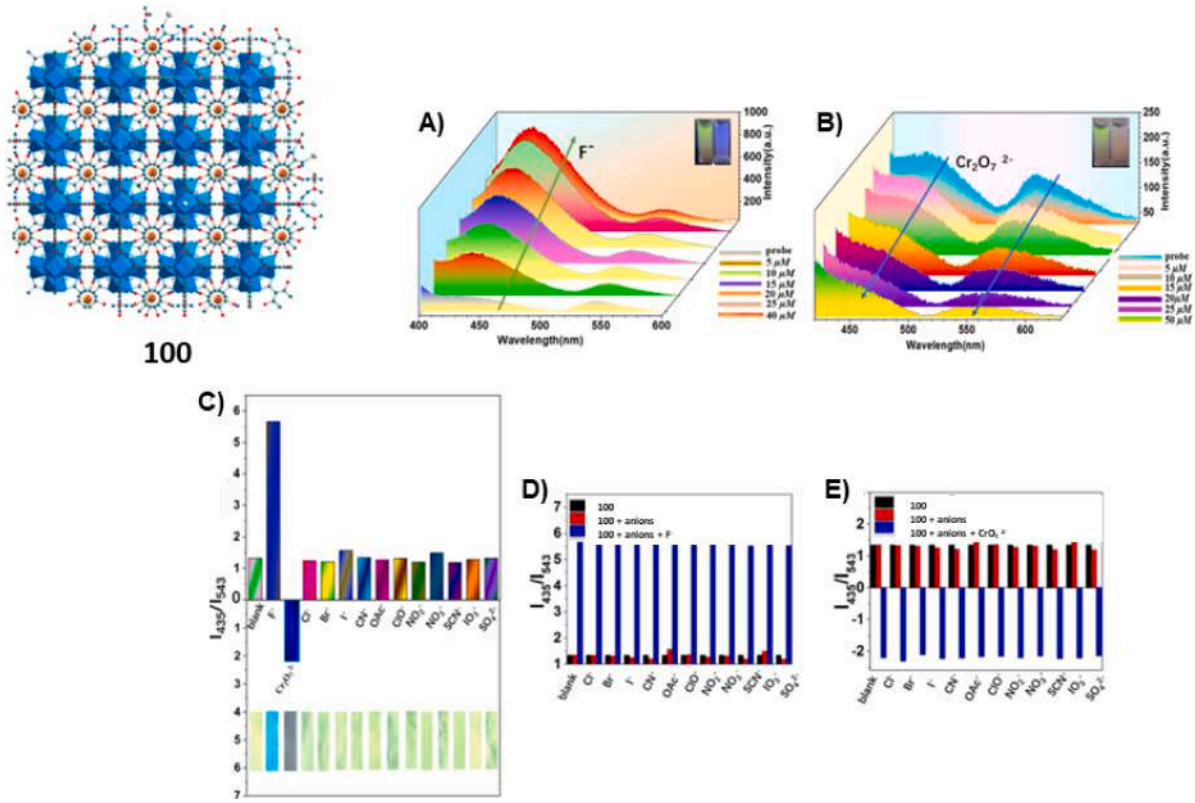

Fig. 47. The representation of the composite MOF chemosensor **100**; emission profile of **100** upon the addition of an increasing amount of A) F^- (inset: colour change of the solution in the presence of an excess of F^- under the UV lamp) and B) $Cr_2O_7^{2-}$ (inset: colour change of the solution in the presence of an excess of $Cr_2O_7^{2-}$ under the UV lamp); C) spectrofluorimetric response of **100** in the presence of the anions tested; competitive test of **100** in the presence of D) F^- and E) $Cr_2O_7^{2-}$. Reproduced with permission from Ref. [38]. Copyright Elsevier 2021.

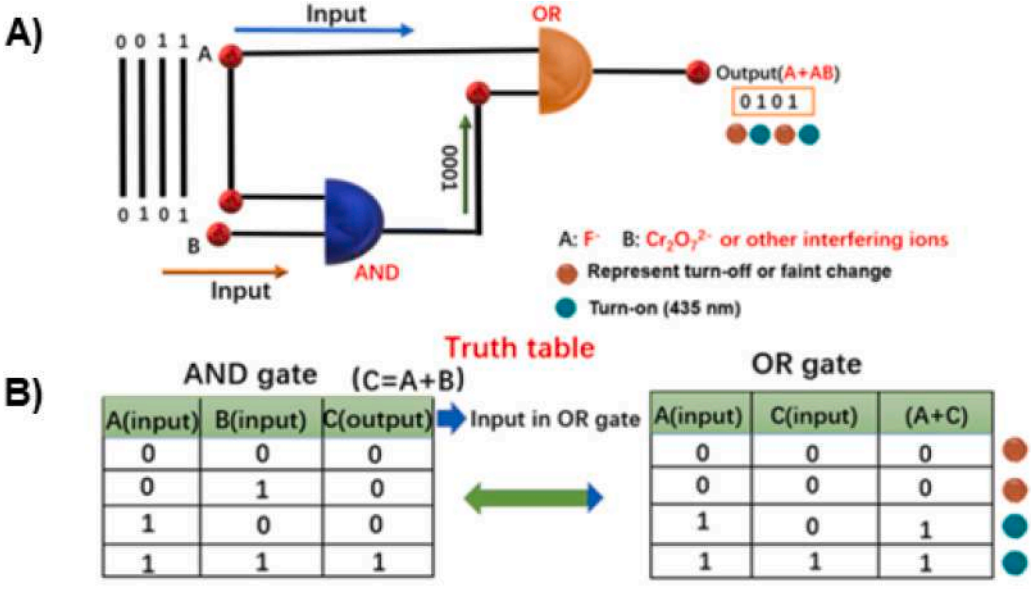

Fig. 48. A) The AND-OR coupled molecular logic circuit set for **100** and B) the corresponding truth table. Reproduced with permission from Ref. [38]. Copyright Elsevier 2021 (Fig. 9).

of a set of anion species (F^-, Cl^-, Br^-, I^-, ATP, AMP, SO_4^{2-}, PO_4^{3-}, HPO_4^{2-}, $H_2PO_4^-$, and $HP_2O_7^{3-}$), and only upon the addition of the SO_4^{2-} the strong emission of the complex was quenched. In order to deeply evaluate this behavior, a fluorescence titration to a solution of **105** in CH_3OH/H_2O (3:2, *v/v*) in HEPES buffer at pH 7.2 in the presence of an increasing concentration of SO_4^{2-} species. As reported in Fig. 57A, upon the addition of the SO_4^{2-}, the characteristic emission band at 330 nm was gradually quenched with the concomitant bathochromic shift to 345 nm, because of the formation of the **105**·Zn^{2+}·SO_4^{2-} complex until stabilization occurred when 1 equiv. of the anion had been added. Further

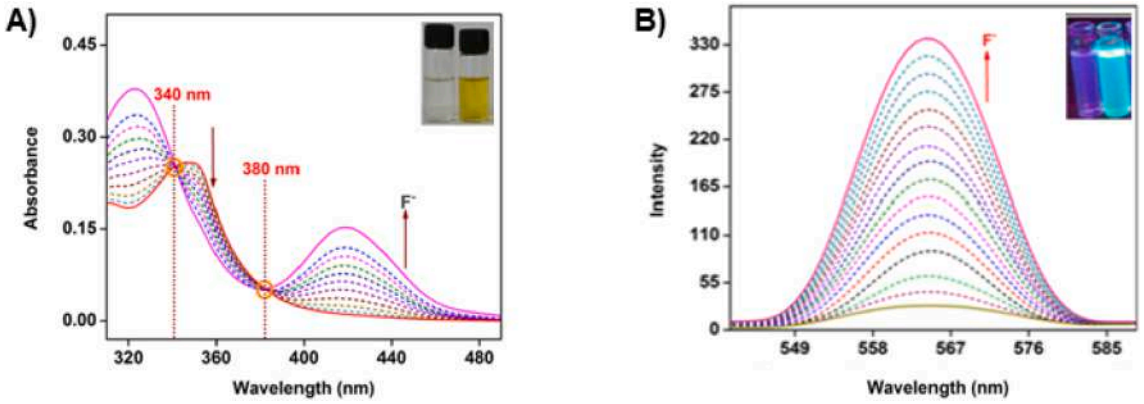

Fig. 49. A) The UV–Vis and B) fluorescence titration of **101** in DMSO/H_2O (7:3, *v/v*) in the presence of an increasing amount of F^-; inset: colour change of a solution of **101** upon the addition of an excess of F^-, A) under the ambient light and B) under the UV light. Reproduced with permission from Ref. [134]. Copyright Elsevier 2020.

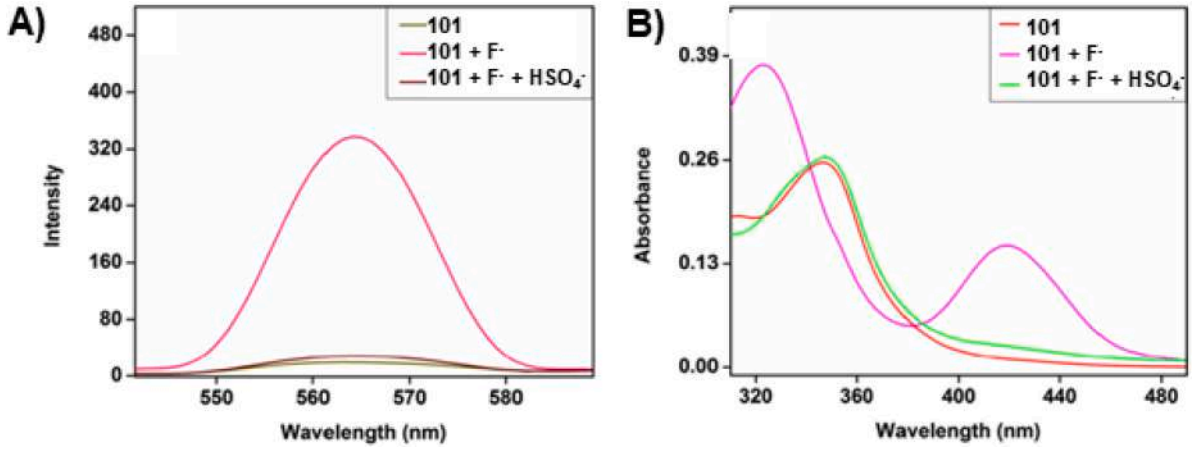

Fig. 50. A) Spectrofluorimetric and B) spectrophotometric response of **101** in the presence of F^- and the simultaneous presence of F^- and HSO_4^-. Reproduced with permission from Ref. [134]. Copyright Elsevier 2020.

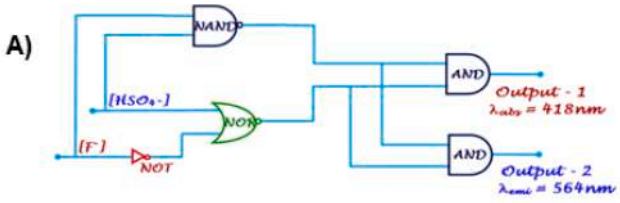

Truth Table

Input		Output	
IN1	IN2	OUT1	OUT2
F^-	HSO_4^-	λ_{abs} at 418 nm	λ_{emi} at 564 nm
0	0	0	0
1	0	1	1
0	1	0	0
1	1	0	0

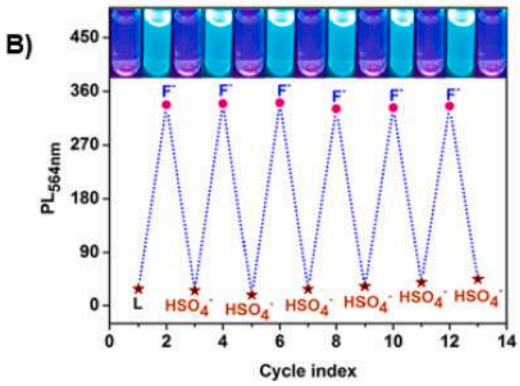

Fig. 51. A) Molecular logic circuit and corresponding truth table; B) fluorimetric response of **101** in DMSO upon the alternate addition of F^- and HSO_4^- with reversible OFF-ON-OFF behaviour. Reproduced with permission from Ref. [134]. Copyright Elsevier 2020.

excess addition of the anion did not cause further changes to the fluorescence properties of the system. This experimental evidence was then further supported by UV–Vis studies in which the formation of the 1:1 adduct was confirmed by the formation of a well-defined isosbestic point at 294 nm.

Following this work, the author decided to build a molecular logic

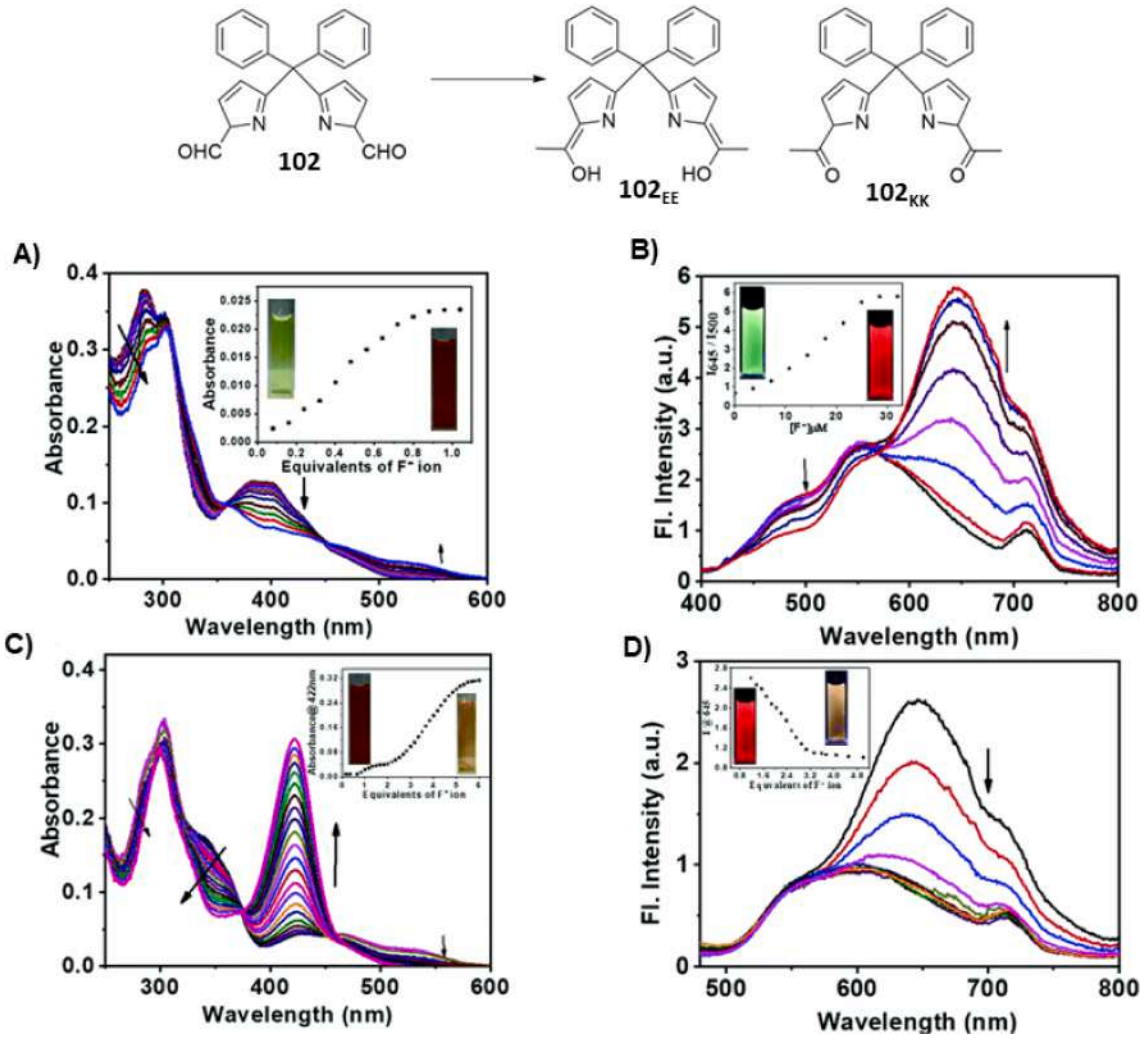

Fig. 52. Schematic representation of the tautomerization process of **102** under UV light; UV–Vis spectra of $\mathbf{102_{KK}}$ and $\mathbf{102_{EE}}$ in CH_3CN upon the addition of A) 1 equiv. and C) 5 equivs. of F^- (inset: corresponding colour changes); fluorescence spectra of $\mathbf{102_{KK}}$ and $\mathbf{102_{EE}}$ in CH_3CN upon the addition of B) 1 equiv. and D) 5 equivs. of F^- (inset: corresponding colour changes). Reproduced with permission from Ref. [135]. Copyright RSC 2020.

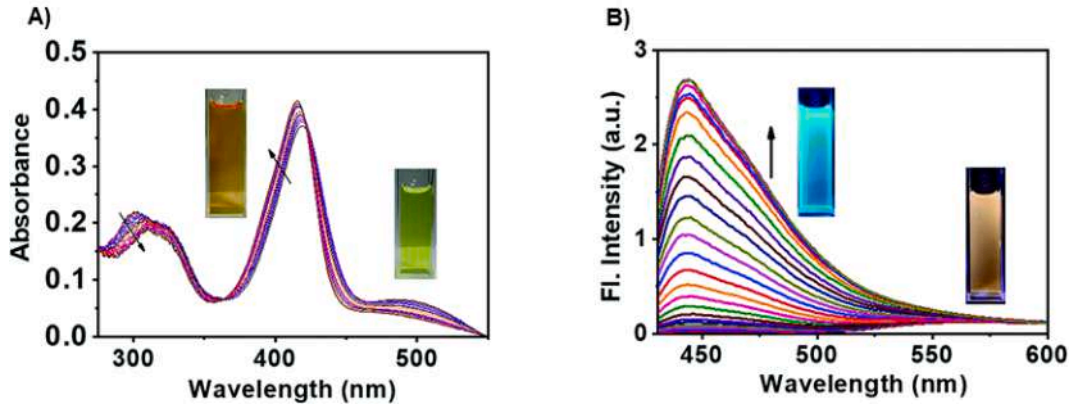

Fig. 53. A) Absorption and B) emission spectra and relative colour changes of $\mathbf{102^2_{KK}}^-$ and $\mathbf{102^2_{EE}}^-$ upon the addition of increasing amounts of Zn(II) in CH_3CN. Reproduced with permission from Ref. [135]. Copyright RSC 2020 (Fig. 8).

circuit based on the INHIBIT operation. The presence of the Zn^{2+} and SO_4^{2-} as was set as the input of the circuit, whereas the emission response at 330 nm was set as the output, while the presence of Zn^{2+} and the absence of SO_4^{2-} is defined as state 1. The circuit was defined to be in state 0 when both Zn^{2+} and SO_4^{2-} were present in the system, when only SO_4^{2-} was present, or in the absence of both the species (emission properties of the free chemosensor). A similar behaviour was described for a salen-type Schiff base in the presence of Al^{3+}, Zn^{2+}, and SO_4^{2-} [139].

Baitalik and co-workers reported the interesting behaviour of the Ru

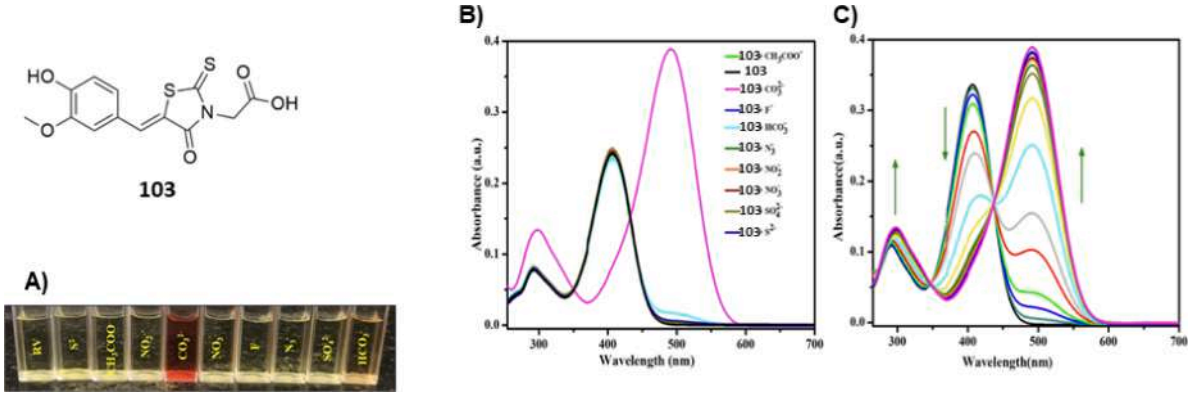

Fig. 54. The molecular structure of **103**. A) The colormetric response of **103** observable by the naked eye, the B) in the UV–Vis spectra of an aqueous solution of **103** when with various anions added; C) UV–vis titration of **103** in aqueous media in the presence of an increasing amount of CO_3^{2-}. Reproduced with permission from Ref. [136]. Copyright Elsevier 2022.

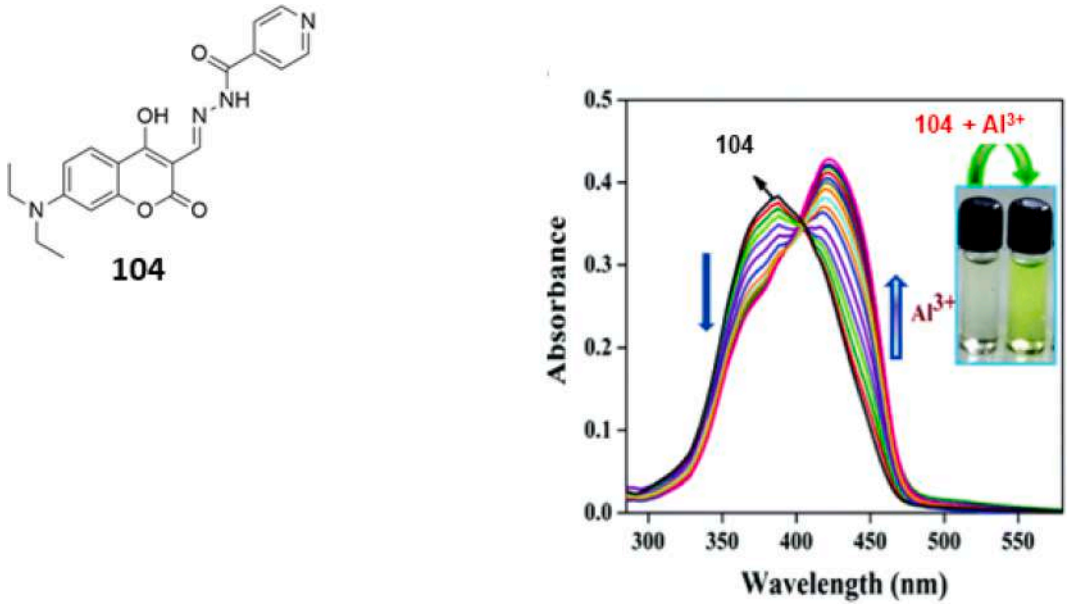

Fig. 55. The molecular structure of **104**; UV–Vis spectra of **104** in DMF:Tris/HCl (6:4, *v/v*) at pH 7.2 upon the addition of an increasing amount of Al^{3+}; inset: colour change of the solution of **104** in the presence of 10 equivs. of Al^{3+}. Reproduced with permission from Ref. [137] Copyright RSC 2021 (Fig. 3).

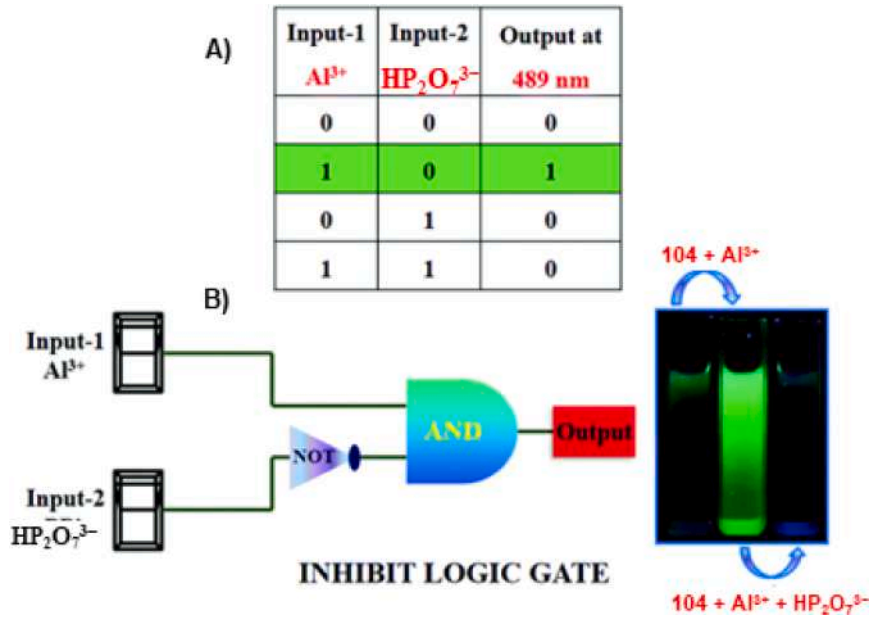

Fig. 56. A) The truth table and B) the molecular logic circuit of the INHIBIT logic gate of **104**. Reproduced with permission from Ref. [137]. Copyright RSC 2021 (Fig. 9).

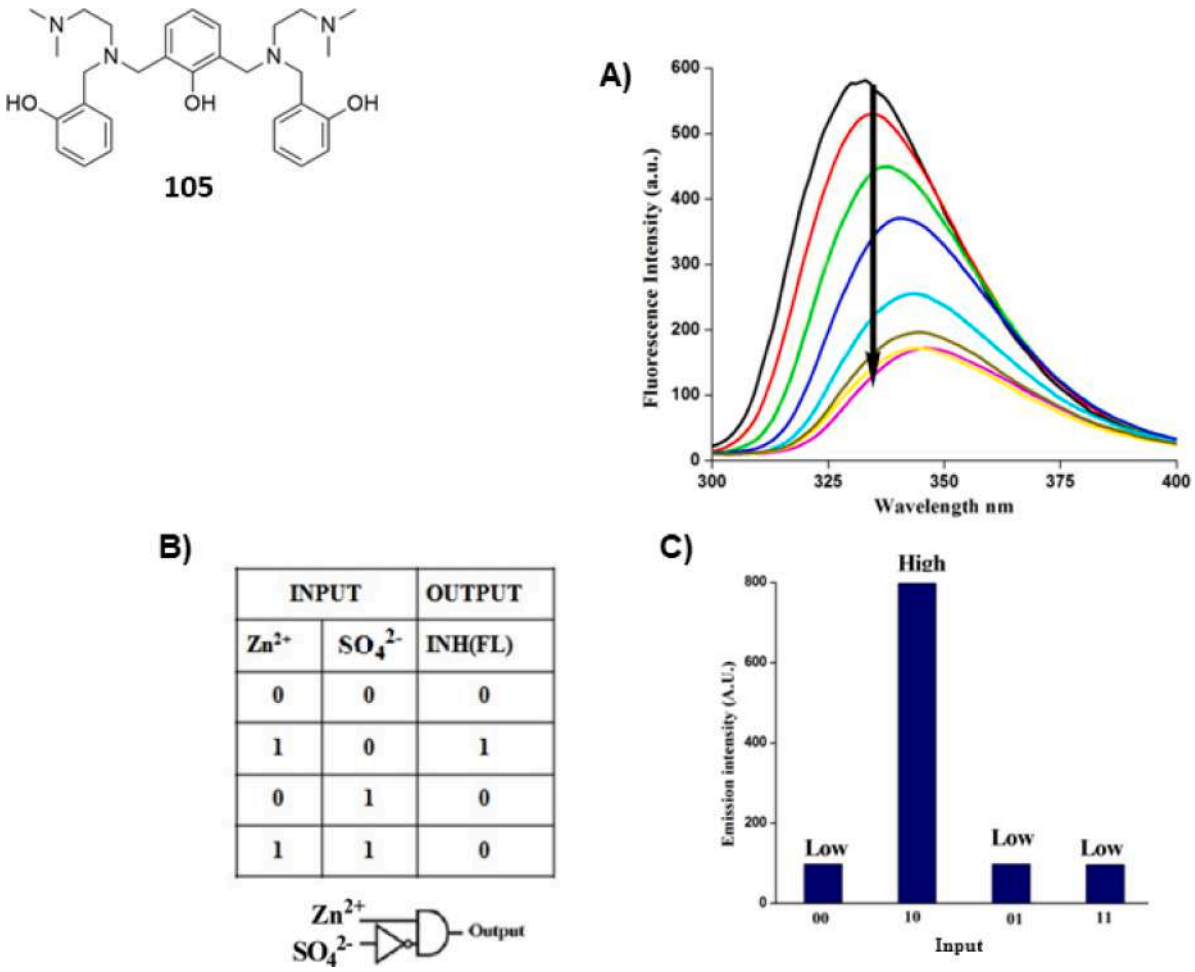

Fig. 57. The molecular structure of **105**; A) emission spectra of **105** in CH_3OH/H_2O (3:2, *v/v*) in HEPES buffer at pH 7.2 upon the addition of an increasing amount of SO_4^{2-}; B) truth table of the INHIBIT logic circuit. Reproduced with permission from Ref. [138]. Copyright Elsevier 2021.

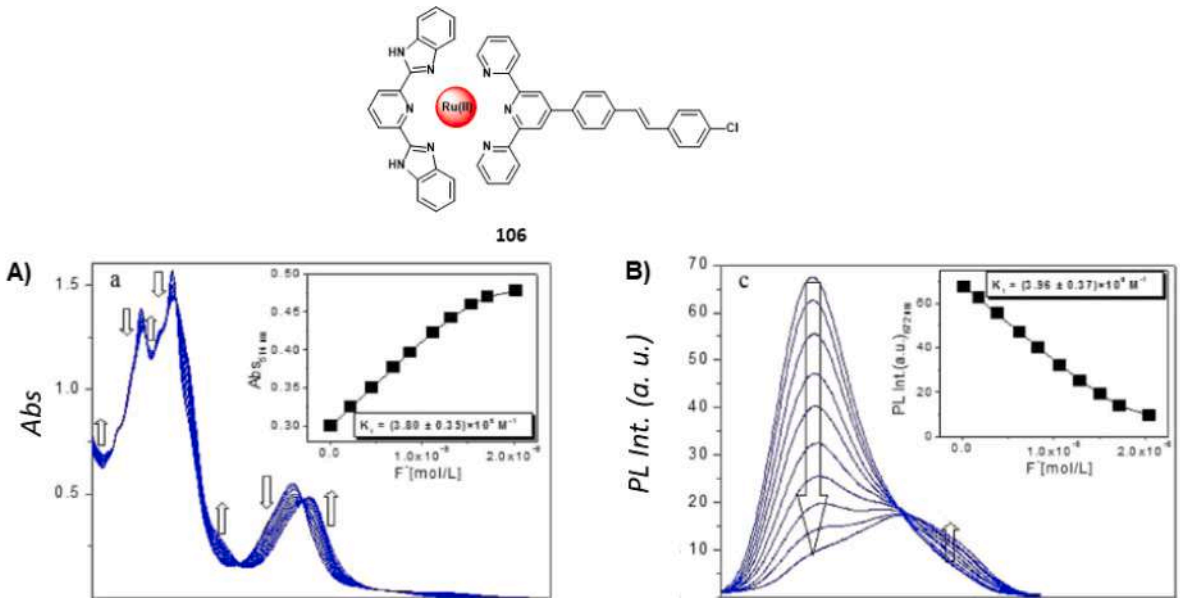

Fig. 58. The molecular structure of the Ru(II) complex **106**; A) absorption and B) emission spectra of **57** in CH_3CN in the presence of an increasing amount of F^-. Reproduced with permission from Ref. [140]. Copyright Wiley 2022 (Fig. 2).

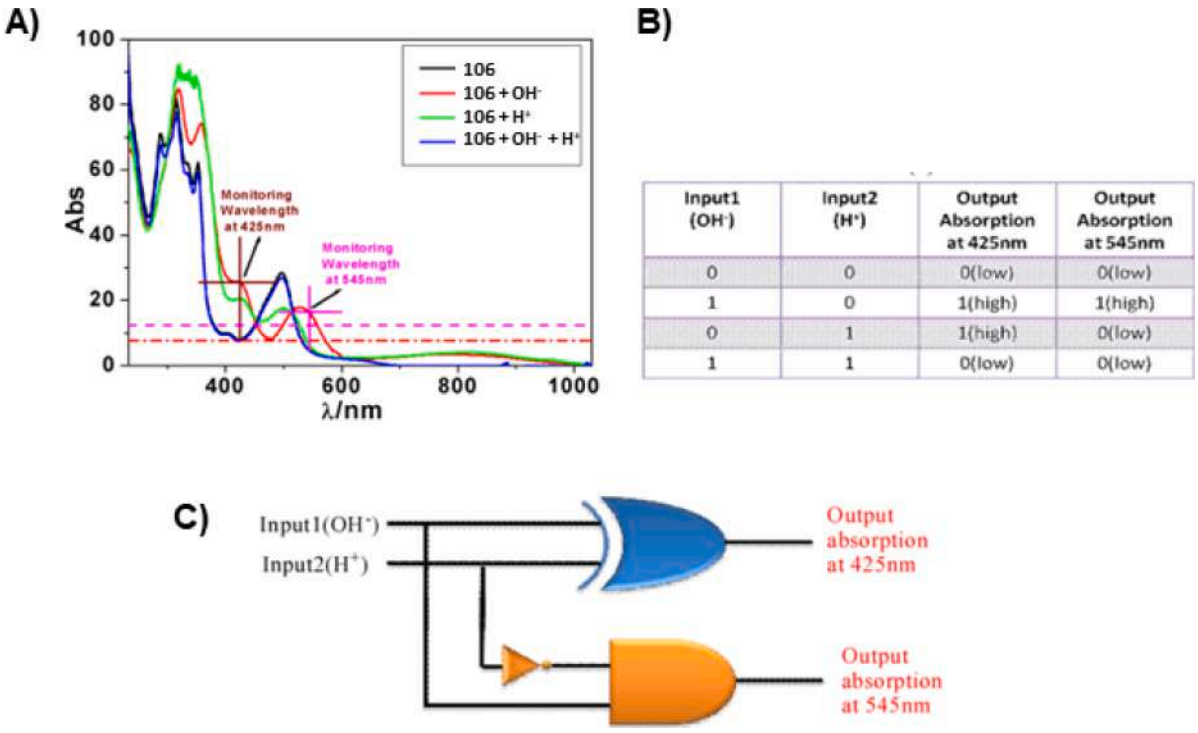

Fig. 59. A) Spectrophotometric response of **106** in the presence of OH^-, H^+, and the simultaneous addition of OH^- and H^+; B) truth table and C) representation of the molecular logic circuit. Reproduced with permission from Ref. [140]. Copyright Wiley 2022.

(II) coordination complex **106** obtained by exploiting the coordination properties of the pyridyl-bis-benzimidazole and both the coordination and switching properties of a stilbene terpyridine derivative (Fig. 58) [140]. Based on previous findings by the same group regarding the *trans/cis* isomerization of these complexes, authors decided to deeply evaluate the optical response, along with the possible implication of multiple advanced Boolean operations, in the presence of different chemical inputs, such as the presence of an anionic species, an acid, or the application of light. Solution studies by UV–Vis and fluorescence spectroscopies were conducted in CH_3CN in the presence of different anions. Particularly, the presence of the more basic anions, such as F^-, AcO^-, and SO_4^{2-}, caused the dramatic red shift of the absorption band centred at 490 nm (ascribed to an MLCT) to 530 nm, accompanied by a colour change of the solution from red to violet. No significant changes were observed upon the addition of the other anions tested, except for the addition of $H_2PO_4^-$, which caused a less remarkable red shift of the MLCT absorption band (from 490 to 500 nm) compared to that observed in the presence of the more basic anions. However, the presence of F^-,

AcO^-, and SO_4^{2-} in a solution of **57** caused the partial quenching of the characteristic emission band at 670 nm, which also red-shifted to 800 nm.

Based on the relative basicity of the anions tested, this behaviour was hypothesized to be due to the deprotonation of the imidazole NHs of the coordination complex by the more basic anions, such as F^-, whereas the $H_2PO_4^-$ was found to be not basic enough to produce the same response. To support the hypothesis of the imidazole deprotonation, the same measurements were conducted in the presence of OH^- showing the same results.

The authors decided to explore the possible implication of molecular logic operations on the system by coupling the reversible deprotonation-protonation phenomenon with reversible *trans–cis* photo-isomerization behaviours of the complexes. Furthermore, the addition of a required amount of acid was found to restore the spectrum of the free complex.

As a first instance, the authors used the XOR and INHIBIT logic operation to obtain two outputs, giving rise to a half-subtractor, which is a conjunctional loop that subtracts two bits and generates their difference. The presence of the OH^- and the H^+ in the system are set as input 1 and input 2. As shown by the truth table reported in Fig. 59, in the presence of one of two inputs, the signal of the output is defined by the ON-state, while in the simultaneous presence or absence of both inputs, the output 1 (absorbance at 425 nm) is defined by the OFF-state. On the other hand, for the INHIBIT operations, output 2 (absorbance at 545 nm) is defined by the ON state only in the presence of the OH^- into the system. Nevertheless, the authors used the same inputs to construct an IMPLICATION molecular logic gate based on AND, OR, and NOT gates. Herein, the authors decided to set the emission at 670 nm as the circuit's output point, which is in the ON state in the presence or the absence of the two inputs. In contrast, the OFF state is obtained when the OH^- only is present in the system.

13. Conclusions

This review highlights the continuing development of sensors for anionic species that have excellent selectivity. An important step forward in this area over this period has been the use of vesicles with transporters to act as a selectivity filter for a sensor encapsulated within a vesicle. The development of sensors that can function in biological systems has also continued. This area of supramolecular chemistry continues to attract much attention, and we can anticipate further developments in the coming years.

Declaration of Competing Interest

The authors declare that they have no known competing financial interests or personal relationships that could have appeared to influence the work reported in this paper.

Data availability

No data was used for the research described in the article.

Acknowledgements

P.A.G. and A.M.G. acknowledge and pay respect to the Gadigal people of the Eora Nation, the traditional owners of the land on which we research, teach, and collaborate at the University of Technology Sydney and The University of Sydney. P.A.G., would like to thank the Australian Research Council (DP200100453) and the University of Technology Sydney for funding. A.M.G. would like to thank The University of Sydney and the Australian Government for the Research Training Program (RTP) scholarship. C.C. would like to thank MIUR (PRIN 2017 project 2017EKCS35) Università degli Studi di Cagliari (FIR 2016-2019) and Fondazione di Sardegna (FdS Progetti Biennali di Ateneo, annualità 2020) for financial support. This study was carried out within the RETURN Extended Partnership and received funding from the European Union Next-GenerationEU (National Recovery and Resilience Plan – NRRP, Mission 4, Component 2, Investment 1.3 – D.D. 1243 2/8/2022, PE0000005).

References

[1] J. Gomez-Vega, J.M. Soto-Cruz, O. Juárez-Sánchez, H. Santacruz-Ortega, J. C. Gálvez-Ruiz, D.O. Corona-Martínez, R. Pérez-González, K. Ochoa Lara, ACS Omega 7 (2022) 22244–22255.
[2] J. Li, M. Saleem, Q. Duan, T. Kakuchi, Y. Chen, Sci. Technol. Adv. Mater. 22 (2021) 597–606.
[3] R. Kato, H. Kahara, Y. Ishii, T. Hattori, Spectrochim. Acta - Part A: Mol. Biomol. Spectroscopy 228 (2020), 117656.
[4] D. Quiñone, M. Belluzzi, J. Torres, M. Brovetto, N. Veiga, Polyhedron 225 (2022).
[5] B. Zavala-Contreras, H. Santacruz-Ortega, A.U. Orozco-Valencia, M. Inoue, K. Ochoa Lara, R.-E. Navarro, ACS Omega 6 (2021) 9381–9390.
[6] S.R. Marshall, A. Singh, J.N. Wagner, N. Busschaert, Chem. Commun. 56 (2020) 14455–14458.
[7] B.K. Billing, M. Verma, ChemistrySelect 6 (2021) 4273–4284.
[8] K. Salvadori, L. Šimková, I. Císařová, J. Sýkora, J. Ludvík, P. Cuřínová, ChemPlusChem 85 (2020) 1401–1411.
[9] P.R. Sharma, S. Pandey, A. Malik, G. Choudhary, V.K. Soni, R.K. Sharma, RSC Adv. 11 (2021) 26644–26654.
[10] I. Yahaya, E. Keleş, A.U. Putra, M. Yahya, N. Seferoğlu, Z. Seferoğlu, J. Mol. Struct. 1204 (2020), 127465.
[11] E.A. Younes, N. Hussein, M. Shtaiwi, F. Shahrokhi, K.A. Abu Safieh, Y. Zhao, New J. Chem. 44 (2020) 16546–16556.
[12] S. Panja, A. Kumar, N. Misra, S. Ghosh, R. Raza, K. Ghosh, ChemistrySelect 6 (2021) 6353–6359.
[13] H.-F. Xie, C. Wu, J. Zou, Y.-X. Yang, H. Xu, Q.-L. Zhang, C. Redshaw, T. Yamato, Dyes Pigm. 178 (2020), 108340.
[14] R. Nazarian, H.R. Darabi, K. Aghapoor, R. Firouzi, H. Sayahi, Chem. Commun. 56 (2020) 8992–8995.
[15] L.A. Marchetti, L.K. Kumawat, N. Mao, J.C. Stephens, R.B.P. Elmes, Chem 5 (2019) 1398–1485.
[16] G. Picci, C. Caltagirone, M.C. Aragoni, M. Arca, M. Formica, V. Fusi, L. Giorgi, F. Ingargiola, V. Lippolis, E. Macedi, L. Mancini, L. Mummolo, L. Prodi, Org. Biomol. Chem. 21 (2023) 2968–2975.
[17] G. Picci, I. Carreira-Barral, D. Alonso-Carrillo, C. Busonera, J. Milia, R. Quesada, C. Caltagirone, Org. Biomol. Chem. 20 (2022) 7981–7986.
[18] G. Picci, M. Kubicki, A. Garau, V. Lippolis, R. Mocci, A. Porcheddu, R. Quesada, P. C. Ricci, M.A. Scorciapino, C. Caltagirone, Chem. Commun. 56 (2020) 11066–11069.
[19] V. Saez Talens, J. Davis, C.-H. Wu, Z. Wen, F. Lauria, K.B.S.S. Gupta, R. Rudge, M. Boraghi, A. Hagemeijer, T.T. Trinh, P. Englebienne, I.K. Voets, J.I. Wu, R. E. Kieltyka, J. Am. Chem. Soc. 142 (2020) 19907–19916.
[20] R.I. Storer, C. Aciro, L.H. Jones, Chem. Soc. Rev. 40 (2011) 2330–2346.
[21] M. Zaleskaya-Hernik, Ł. Dobrzycki, M. Karbarz, J. Romański, Int. J. Mol. Sci. 22 (2021) 13396.
[22] A. Grundzi, S.A. Healy, O. Fenelon, R.B.P. Elmes, Results Chem. 4 (2022), 100652.
[23] A.A. Abogunrin, S.A. Healy, O. Fenelon, R.B.P. Elmes, Chemistry 4 (2022) 1288–1299.
[24] G. Picci, J. Milia, M.C. Aragoni, M. Arca, S.J. Coles, A. Garau, V. Lippolis, R. Montis, J.B. Orton, C. Caltagirone, Molecules 26 (5) (2021) 1301.
[25] R. Ahmed, A. Ali, M. Ahmad, A. Alsalme, R.A. Khan, F. Ali, New J. Chem. 44 (2020) 20092–20100.
[26] R.S. Fernandes, N. Dey, Talanta 250 (2022), 123703.
[27] R.K. Jakku, N. Mirzadeh, S.H. Privér, G. Reddy, A.K. Vardhaman, G. Lingamallu, R. Trivedi, S.K. Bhargava, Chemosensors 9 (2021) 285.
[28] S. Jindal, J.N. Moorthy, Inorg. Chem. 61 (2022) 3942–3950.
[29] V. Kavitha, K. Chitra, A. Gomathi, R. Dhivya, P. Viswanathamurthi, J. Anal. Chem. 77 (2022) 882–892.
[30] P. Rana, A. Jennifer, G.M. Siva, E. Varathan, P. Das, New J. Chem. 46 (2022) 23139–23154.
[31] G. Yuan, Z.Q. Chen, C. Zhang, Z.Y. Xie, S.Y. Liu, X.H. Meng, J.Y. Sun, X.M. Li, L. H. Dong, X.R. Hao, J. Solid State Chem. 315 (2022), 123442.
[32] R. Ali, S.K. Dwivedi, H. Mishra, A. Misra, Dyes Pigm. 175 (2020), 108163.
[33] G. Cavallo, P. Metrangolo, R. Milani, T. Pilati, A. Priimagi, G. Resnati, G. Terraneo, Chem. Rev. 116 (2016) 2478–2601.
[34] L.C. Gilday, S.W. Robinson, T.A. Barendt, M.J. Langton, B.R. Mullaney, P.D. Beer, Chem. Rev. 115 (2015) 7118–7195.
[35] G.R. Desiraju, P.S. Ho, L. Kloo, A.C. Legon, R. Marquardt, P. Metrangolo, P. Politzer, G. Resnati, K. Rissanen, Pure Appl. Chem. 85 (2013) 1711–1713.
[36] R. Hein, P.D. Beer, Chem. Sci. 13 (2022) 7098–7125.
[37] T. Bunchuay, K. Boonpalit, A. Docker, A. Ruengsuk, J. Tantirungrotechai, M. Sukwattanasinitt, P. Surawatanawong, P.D. Beer, Chem. Commun. 57 (2021) (1979) 11976–111971.
[38] A. Docker, X. Shang, D. Yuan, H. Kuhn, Z. Zhang, J.J. Davis, P.D. Beer, M. J. Langton, Angew. Chem. Int. Ed. 60 (2021) 19442–19450.
[39] E.J. Mitchell, A.J. Beecroft, J. Martin, S. Thompson, I. Marques, V. Félix, P. D. Beer, Angew. Chem. Int. Ed. 60 (2021) 24048–24053.
[40] S. Mondal, A. Rashid, P. Ghosh, J. Organomet. Chem. 952 (2021), 122027.

[41] N.d.J. Hiller, N.A. do Amaral e Silva, T.A. Tavares, R.X. Faria, M.N. Eberlin, D. de Luna Martins, Eur. J. Org. Chem., 2020 (2020) 4841–4877.
[42] Z. Cao, Y. Cao, R. Kubota, Y. Sasaki, K. Asano, X. Lyu, Z. Zhang, Q. Zhou, X. Zhao, X. Xu, S. Wu, T. Minami, Y. Liu, Front. Chem. 8 (2020), 414.
[43] Y. Liu, Y. Zhou, H. Li, J. Gao, M. Yang, Z. Yuan, X. Li, ACS Omega 7 (2022) 34317–34325.
[44] L.R. Ortega-Valdovinos, J. Valdes-García, I.J. Bazany-Rodríguez, J.C. Lugo-González, A. Dorazco-González, A.K. Yatsimirsky, New J. Chem. 45 (2021) 15618–15628.
[45] B.P. Jacobs, J. Townsend, K.D. Vogiatzis, J.N. Brantley, Polym. Chem. 11 (2020) 1919–1925.
[46] Y. Qi, X. Cao, Y. Zou, C. Yang, J. Mater. Chem. C 9 (2021) 1567–1571.
[47] O.S. Ipek, S. Topal, T. Ozturk, Dyes Pigm. 192 (2021), 109458.
[48] C.A.S. P, A.V. Raveendran, N. Sivakrishna, R.P. Nandi, Dalton Transactions, 51 (2022) 15339-15353.
[49] G. Turkoglu, T. Ozturk, Dalton Trans. 51 (2022) 2715–2725.
[50] J. Wang, Y. Zhang, Q. Lin, Q. Huang, Y. Liu, J. Mol. Struct. 1257 (2022), 132537.
[51] A.V. Raveendran, C.a.s. p,, New J. Chem. 46 (2022) 20299–20310.
[52] H. Lee, S. Jana, J. Kim, S.U. Lee, M.H. Lee, Inorg. Chem. 59 (2020) 1414–1423.
[53] S.R. Bayly, P.D. Beer, Metal-based anion receptor systems, in: R. Vilar (Ed.), Recognition of Anions, Springer, Berlin Heidelberg, Berlin, Heidelberg, 2008, pp. 45–94.
[54] L. Conti, N. Flore, M. Formica, L. Giorgi, M. Pagliai, L. Mancini, V. Fusi, B. Valtancoli, C. Giorgi, Inorg. Chim. Acta 519 (2021), 120261.
[55] E. Macedi, L. Giorgi, M. Formica, P. Rossi, D. Paderni, P. Paoli, V. Fusi, ChemPlusChem 88 (2023), e202200364.
[56] R. Das, M. Mondal, S. Paul, A. Pan, P. Banerjee, Inorg. Chim. Acta 548 (2023), 121364.
[57] M. Formica, V. Fusi, D. Paderni, G. Ambrosi, M. Inclán, M.P. Clares, B. Verdejo, E. García-España, Molecules 26 (2021) 2352.
[58] K. Satheeshkumar, P. Saravana Kumar, C. Nandhini, R. Shanmugapriya, K. N. Vennila, K.P. Elango, Inorg. Chem. Commun. 139 (2022), 109299.
[59] S.-Y. Huang, V.C. Pierre, JACS Au 2 (2022) 1604–1609.
[60] Y.-S. Wong, M. Ng, M.-C.-L. Yeung, V.-W.-W. Yam, J. Am. Chem. Soc. 143 (2021) 973–982.
[61] M. Rabha, B. Sen, S.K. Sheet, K. Aguan, S. Khatua, Dalton Trans. 51 (2022) 11372–11380.
[62] S. Deb, A. Sahoo, P. Pal, S. Baitalik, Inorg. Chem. 60 (2021) 6836–6851.
[63] Z.-L. Gong, Y.-W. Zhong, J. Organomet. Chem. 931 (2021), 121612.
[64] M. Kumari, K. Dey, S.K. Bera, G.K. Lahiri, Inorg. Chem. 61 (2022) 16122–16140.
[65] S. Mondal, K. Sarkar, P. Ghosh, Inorg. Chem. 60 (2021) 9084–9096.
[66] M. Toyama, T. Hasegawa, N. Nagao, RSC Adv. 12 (2022) 25227–25239.
[67] C. Sonkar, S. Sarkar, N. Malviya, M.L. Kuznetsov, S. Mukhopadhyay, Dalton Trans. 51 (2022) 13071–13084.
[68] S.E. Bodman, S.J. Butler, Chem. Sci. 12 (2021) 2716–2734.
[69] V.C. Pierre, R.K. Wilharm, Front. Chem. 10 (2022), 821020.
[70] N.Y. Edwards, D.M. Schnable, I.R. Gearba-Dolocan, J.L. Strubhar, Molecules 26 (2021) 87.
[71] C. Gong, Z. Li, G. Liu, S. Pu, Spectrochim. Acta A Mol. Biomol. Spectrosc. 252 (2021), 119493.
[72] W. Shi, S. Zhang, Y. Wang, Y.D. Xue, M. Chen, Sens. Actuators B 367 (2022), 132008.
[73] Y. Zhao, L. Feng, X. Meng, J. Guan, Dyes Pigm. 183 (2020), 108713.
[74] S. Farshbaf, K. Dey, W. Mochida, M. Kanakubo, R. Nishiyabu, Y. Kubo, P. Anzenbacher, New J. Chem. 46 (2022) 1839–1844.
[75] S.E. Bodman, C. Breen, S. Kirkland, S. Wheeler, E. Robertson, F. Plasser, S. J. Butler, Chem. Sci. 13 (2022) 3386–3394.
[76] S.E. Bodman, C. Breen, F. Plasser, S.J. Butler, Org. Chem. Front. 9 (2022) 5494–5504.
[77] W. Liu, F. Wang, X. Chen, W. Zhi, X. Wang, B. Xu, B. Yang, Dalton Trans. 51 (2022) 15741–15749.
[78] Y. Okayasu, K. Wakabayashi, J. Yuasa, Inorg. Chem. 61 (2022) 15108–15115.
[79] Z. Sun, J. Sun, L. Xi, J. Xie, X. Wang, Y. Ma, L. Li, Cryst. Growth Des. 20 (2020) 5225–5234.
[80] K. Yu, Q. Wang, W. Xiang, Z. Li, Y. He, D. Zhao, Inorg. Chem. 61 (2022) 13627–13636.
[81] C. Alexander, J.A. Thom, A.M. Kenwright, K.E. Christensen, T.J. Sørensen, S. Faulkner, Chem. Sci. 14 (2023) 1194–1204.
[82] M. Alhaddad, S.M. El-Sheikh, ACS Omega 6 (2021) 15182–15191.
[83] L. Esrafili, A. Morsali, M.-L. Hu, A. Azhdari Tehrani, L. Carlucci, P. Mercandelli, D.M. Proserpio, Inorg. Chem. 59 (2020) 16421–16429.
[84] L.D. Rosales-Vázquez, A. Dorazco-González, V. Sánchez-Mendieta, Dalton Trans. 50 (2021) 4470–4485.
[85] J. Xiong, Y. Xiao, J. Liang, J. Sun, L. Gao, Q. Zhou, D. Hong, K. Tan, Spectrochim. Acta A Mol. Biomol. Spectrosc. 285 (2023), 121863.
[86] J. Xiu, G. Wang, Sens. Actuators B 374 (2023), 132837.
[87] S. Hui, P. Daga, P. Mahata, Inorg. Chem. 62 (2023) 591–600.
[88] J.N. Tutol, J. Lee, H. Chi, F.N. Faizuddin, S.S. Abeyrathna, Q. Zhou, F. Morcos, G. Meloni, S.C. Dodani, Chem. Sci. 12 (2021) 5655–5663.
[89] X. Pan, S. Cheng, C. Zhang, X. Qi, Anal. Bioanal. Chem. 412 (2020) 6959–6968.
[90] S. Cheng, X. Pan, M. Shi, T. Su, C. Zhang, W. Zhao, W. Dong, Spectrochim. Acta A Mol. Biomol. Spectrosc. 228 (2020), 117710.
[91] A. Rashid, S. Mondal, S. Mondal, P. Ghosh, Chem. Asian J. 17 (2022).
[92] L. Yang, L. Han, H. Zhu, H. Ma, Polym. Chem. 13 (2022) 1274–1281.
[93] A.S. Miranda, P.M. Marcos, J.R. Ascenso, M.N. Berberan-Santos, F. Menezes, Molecules 27 (2022) 3247.
[94] F. Chen, H. Xu, Y. Cai, W. Zhang, P. Shen, W. Zhang, H. Xie, G. Bai, S. Xu, J. Gao, Molecules 27 (2022) 8750.
[95] O. Hayashida, S. Imamura, T. Miyazaki, Chem. Lett. 51 (2022) 859–861.
[96] S. Ghosh, N. Baildya, K. Goswami, K. Ghosh, ChemistrySelect 6 (2021) 8932–8937.
[97] S. Garain, S.M. Wagalgave, A.A. Kongasseri, B.C. Garain, S.N. Ansari, G. Sardar, D. Kabra, S.K. Pati, S.J. George, J. Am. Chem. Soc. 144 (2022) 10854–10861.
[98] S. Mommer, S.J. Wezenberg, ACS Appl. Mater. Interfaces 14 (2022) 43711–43718.
[99] D. Villarón, N. Duindam, S.J. Wezenberg, Chem. A Eur. J. 27 (2021) 17346–17350.
[100] D. Villarón, S.J. Wezenberg, Angew. Chem. Int. Ed. 59 (2020) 13192–13202.
[101] S.J. Wezenberg, L.J. Chen, J.E. Bos, B.L. Feringa, E.N.W. Howe, X. Wu, M. A. Siegler, P.A. Gale, J. Am. Chem. Soc. 144 (2022) 331–338.
[102] F. Xu, L. Pfeifer, S. Crespi, F.K.C. Leung, M.C.A. Stuart, S.J. Wezenberg, B. L. Feringa, J. Am. Chem. Soc. 143 (2021) 5990–5997.
[103] D. Villarón, M.A. Siegler, S.J. Wezenberg, Chem. Sci. 12 (2021) 3188–3193.
[104] T.S.C. MacDonald, B.L. Feringa, W.S. Price, S.J. Wezenberg, J.E. Beves, J. Am. Chem. Soc. 142 (2020) 20014–20020.
[105] J.D. Einkauf, V.S. Bryantsev, B.A. Moyer, R. Custelcean, Chem. A Eur. J. 28 (2022) e2022007.
[106] O. Dalkilic, E. Bozkurt, H. Kilic, New J. Chem. 46 (2022) 20473–20480.
[107] Y. Fang, M. Wang, Y. Shen, M. Zhang, Z. Cao, Y. Deng, Inorg. Chim. Acta 503 (2020), 119413.
[108] D. Sóvári, G.M. Keserű, P. Ábrányi-Balogh, Materials 13 (2020) 199.
[109] S.H. Lee, M.S. Mun, M. Kim, J.H. Lee, H. Hwang, W. Lee, K.M. Lee, RSC Adv. 11 (2021) 24057–24064.
[110] V.G. More, D.N. Nadimetla, D.B. Shaikh, A.L. Puyad, S.V. Bhosale, S.V. Bhosale, ChemistrySelect 7 (2022), e202201537.
[111] R. Shanmugapriya, P. Saravana Kumar, S. Ponkarpagam, C. Nandhini, K. N. Vennila, A.G. Al-Sehemi, M. Pannipara, K.P. Elango, J. Mol. Struct. 1251 (2022), 132081.
[112] S. Saha, P. Ghosh, P. Mondal, A. Chattopadhyay, P. Sahoo, Environ. Sci. Processes Impacts 23 (2021) 1308–1315.
[113] E. Keleş, B. Aydıner, Y. Nural, N. Seferoğlu, E. Şahin, Z. Seferoğlu, Eur. J. Org. Chem. 2020 (2020) 4681–4692.
[114] C. Shen, Q. Tang, C.-B. Gong, C.-F. Chow, J. Mater. Chem. C 8 (2020) 5029–5035.
[115] L.C. Murfin, C.M. López-Alled, A.C. Sedgwick, J. Wenk, T.D. James, S.E. Lewis, Front. Chem. Sci. Eng. 14 (2020) 90–96.
[116] K. Mariappan, P.K. Shrestha, A. Hussain, A.G. Sykes, J. Mol. Struct. 1267 (2022), 133585.
[117] Z. Li, S. Li, H. Lv, J. Shen, X. He, B. Peng, Spectrochim. Acta A Mol. Biomol. Spectrosc. 269 (2022), 120766.
[118] Y. Shiraishi, R. Nakatani, S. Takagi, C. Yamada, T. Hirai, Chemosensors 8 (2020) 123.
[119] N. Dey, S. Bhattacharya, Chem. Asian J. 15 (2020) 1759–1779.
[120] Y. Guan, Y. Lu, J. Sun, J. Zhao, W. Huang, X. Zhang, Y. Liu, ACS Sustain. Chem. Eng. 9 (2021) 9802–9812.
[121] W. Miao, L. Wang, Q. Liu, S. Guo, L. Zhao, J. Peng, Chem. Asian J. 16 (2021) 247–251.
[122] Y. Sasaki, R. Kubota, T. Minami, Coord. Chem. Rev. 429 (2021), 213607.
[123] G.E. Sergeant, V.E. Zwicker, K.A. Jolliffe, Anal. Sensing 3 (2023), e202200089.
[124] H. Sharifi, J. Tashkhourian, B. Hemmateenejad, Sens. Actuators B 339 (2021), 129911.
[125] M. Šídlo, P. Lubal, P. Anzenbacher, Chemosensors 9 (2021) 39.
[126] Z. Zhang, V. Hamedpour, X. Lyu, Y. Sasaki, T. Minami, ChemPlusChem 86 (2021) 798–802.
[127] V.E. Zwicker, G.E. Sergeant, E.J. New, K.A. Jolliffe, Org. Biomol. Chem. 19 (2021) 1017–1021.
[128] H. Yao, Y.-B. Niu, Y.-P. Hu, X.-W. Sun, Q.-P. Zhang, Y.-M. Zhang, T.-B. Wei, Q. Lin, New J. Chem. 46 (2022) 17251–17259.
[129] M. Pushina, S. Farshbaf, W. Mochida, M. Kanakubo, R. Nishiyabu, Y. Kubo, P. Anzenbacher Jr., Chem. Eur. J. 27 (2021) 11344–11351.
[130] M.P. Bhat, S. Vinayak, J. Yu, H.-Y. Jung, M. Kurkuri, ChemistrySelect 5 (2020) 13135–13143.
[131] R. Arabahmadi, J. Photochem. Photobiol. A Chem. 427 (2022), 113797.
[132] R. Bhaskar, N. Mageswari, D. Sankar, G.G. Vinoth Kumar, Mater. Lett. 327 (2022), 133040.
[133] Y. Zhang, L. Zhang, J. Hazard. Mater. 418 (2021), 126271.
[134] D. Mohanasundaram, G.G. Vinoth Kumar, S.K. Kumar, B. Maddiboyina, R.P. Raja, J. Rajesh, G. Sivaraman, J. Mol. Liq. 317 (2020), 113913.
[135] K.C. Gowri Sreedevi, A.P. Thomas, B. Adinarayana, A. Srinivasan, New J. Chem. 44 (2020) 11768–11776.
[136] N. Malini, A. Siva, Inorg. Chem. Commun. 143 (2022), 109754.
[137] M. Mathivanan, B. Tharmalingam, T. Devaraj, A. Murugan, C.-H. Lin, M. Jothi, B. Murugesapandian, New J. Chem. 45 (2021) 6067–6079.
[138] A. Hens, Inorg. Chim. Acta 511 (2020), 119794.
[139] S. Das, M. Das, S. Laha, K. Rajak, I. Choudhuri, N. Bhattacharyya, B.C. Samanta, T. Maity, J. Mol. Struct. 1263 (2022), 133214.
[140] P. Pal, A. Sahoo, A. Paul, S. Baitalik, Eur. J. Inorg. Chem. (2022), e202200219.